Probing electronic and structural properties of single molecules on the atomic scale

Dissertation
zur Erlangung des Doktorgrades
der Naturwissenschaften (Dr. rer. nat.)
der Fakultät für Physik
der Universität Regensburg

vorgelegt von
Fabian Mohn
aus Ludwigsburg

Mai 2012

Promotionsgesuch eingereicht am 17.04.2012.
Diese Arbeit wurde angeleitet von Dr. G. Meyer und Prof. Dr. J. Repp.

Prüfungsausschuss:

Vorsitzender:	Prof. Dr. I. Morgenstern
1. Gutachter:	Prof. Dr. J. Repp
2. Gutachter:	Prof. Dr. C. Back
Weiterer Prüfer:	Prof. Dr. F. Gießibl

Contents

CHAPTER 1

Introduction

The concept of using single molecules as functional components in electronic devices was established long ago [1], but progress in this field has often been hampered by a limited understanding of the microscopic details of the interaction of individual molecules with their environment and of how this interaction may modify their electronic and structural properties. In this context, scanning probe techniques offer the unique possibility of studying single molecules on surfaces with atomic precision. Scanning tunneling microscopy (STM), for example, has been used to study electron transport through single-molecule junctions [2–5] and to measure the vibrational spectra of individual molecules [6, 7]. Furthermore, the possibility of STM to manipulate single atomic and molecular adsorbates [8, 9] has been utilized to induce and study chemical reactions on surfaces at the single-molecule level [10–14] and to assemble molecular adsorbates to form artificial structures [15, 16]. Insulating films of a thickness of only a few atomic layers electronically decouple adsorbates from the underlying metal substrate, while presenting a small enough barrier for the tunneling electrons to still allow STM operation at small currents. In such double-barrier tunnel junction geometries, the reversible charging of single atoms [17], the coupling of light to single molecules [18–20], and the excitation of spins in single atoms [21, 22] and assembled nanostructures [23, 24] have been studied. Furthermore, it was shown that on thin insulating films, the essentially unperturbed frontier electron orbitals of a molecule can be imaged [25],

yielding insights into the formation of single chemical bonds [13, 26] and the tautomerization switching of single molecules [27].

Atomic force microscopy (AFM) is another variant of scanning probe microscopy that does not suffer from the STM's limitation to conductive samples. After the introduction of the frequency modulation technique in noncontact AFM [28] and the first demonstration of true atomic resolution [29], significant progress has been reported in recent years in atomic-resolution AFM: for example, atomic resolution on carbon nanotubes [30], chemical identification of surface atoms [31], and both lateral and vertical manipulation of single atoms [32, 33] have been achieved. Because in AFM forces are measured instead of tunneling currents, it can provide information that is not accessible with STM: for example, the energies/forces required to operate a molecular switch [34] or to move single atoms and molecules [35] have been determined, and the magnetic exchange force was measured with atomic resolution [36]. An important recent development is the introduction and increasing proliferation of self-sensing AFM sensors such as the qPlus tuning fork [37]. With their simple detection scheme and their immediate suitability for simultaneous STM and AFM investigations, they have made noncontact-AFM attractive for an even wider community of surface scientists.

In this thesis work, a combination of low-temperature STM and AFM was used to study different atomic and molecular adsorbates on thin insulating films with atomic resolution. We show that noncontact-AFM can yield important additional information for these systems, which had previously only been studied with STM. In particular, we demonstrate the detection of electrostatic forces with single-electron charge sensitivity and atomic-scale lateral resolution, and we show that noncontact-AFM with functionalized tips enables atomic-resolution imaging of single molecules. The thesis is structured as follows: In Chapter 2, we give an introduction to scanning probe microscopy, describing briefly the experimental and theoretical principles underlying the methods used in this work. Next, in Chapter 3, we provide some details of the experimental setup and describe the tip and sample preparation procedures used in our experiments. In the following chapters, several STM and AFM studies of individual atoms and molecules are presented:

In Chapter 4, we investigate the charge switching of single metal adatoms on ultrathin NaCl films on Cu(111) with AFM. Charging of an adatom

by one electron charge is found to increase the force on the AFM tip by a few pN, enabling the direct discrimination of neutral and charged adatoms in AFM images. Furthermore, we show that depending on the sign of the charge, the local contact potential difference between the tip and the sample is shifted, which can be detected with Kelvin probe force microscopy (KPFM), a special mode of AFM.

In Chapter 5, we demonstrate that AFM can be used to image the chemical structure of single organic molecules. The key step to achieving such high resolution was to functionalize the AFM tip with a suitable atomically well-defined termination, for example a single CO molecule. To elucidate the exact nature of the imaging mechanism and to extend the method towards the imaging of nonplanar molecules, we developed an imaging technique that enables atomic-resolution measurements of the complete three-dimensional force field above a molecule. By comparison with density functional theory calculations, we are able to identify Pauli repulsion as the source of the atomic contrast in our AFM images.

In Chapter 6, we investigate a molecular switch based on the reversible bond formation between a metal atom and an organic molecule on a thin insulating NaCl film. The operation and electronic characterization of the switch were performed with STM, whereas the exact structural details of the metal-molecule complex were deduced from atomically resolved AFM images. A comparison of the experimental results with DFT calculations suggests that a special mechanism of bond formation, which involves different charge states of the metal-molecule complex, is responsible for the favorable characteristics of this molecular switch.

In Chapter 7, we demonstrate the usefulness of atomic-resolution AFM imaging to aid in the determination of the structure of an unknown molecule. We investigated a molecule extracted from a sample collected in the deep sea, for which other methods had failed in an unambiguous structure determination. By directly imaging the chemical structure and adsorption position of the unknown compound with AFM and comparison of the experimental results to DFT calculations, we were eventually able to unambiguously identify the molecule as cephalandole A.

In Chapter 8, we combine the charge sensitivity demonstrated in Chapter 4 with the submolecular resolution demonstrated in Chapter 5 to image the charge distribution within a single molecule. We show that a pronounced asymmetry exists between the different lobes of the investigated

naphthalocyanine molecule, which clearly manifests itself in submolecularly resolved KPFM images. By comparison with DFT calculations, we identify the electric field generated by the intramolecular charge distribution as the source of contrast in the KPFM images.

These investigations show that by combining STM and AFM, the electronic and structural properties of single molecules can be revealed in unprecedented detail. We anticipate that the possibility of imaging the chemical structure with AFM and the intramolecular charge distribution with KPFM, in combination with the established spectroscopic techniques of STM, will lead to new fundamental insights into single-molecule switching and bond formation, processes that are often accompanied by a structural rearrangement or an intra- or intermolecular redistribution of charge.

CHAPTER 2

Basic principles of scanning probe microscopy

Since the invention of the scanning tunneling microscope (STM) in 1981 and the atomic force microscope (AFM) in 1985, a number of probe-based microscopy techniques – subsumed under the term scanning probe microscopy – have been developed. These techniques have turned out to be invaluable tools for surface analysis on the micro- and nanoscale and even on the atomic level. The various scanning probe techniques are today widely being used both for scientific research and for industrial applications. Their fields of application range from the characterization of inorganic surfaces to investigations of biological systems.

In this chapter, we briefly summarize the historical development of scanning probe microscopy, before describing the functional principle of STM and AFM. We focus mainly on certain aspects that are relevant to this thesis and refer the reader for further details to the various books and review articles about scanning probe microscopy [38–45].

2.1 Historical introduction

The STM was invented by Binnig and Rohrer in 1981 at the IBM Zurich Research Laboratory [46]. It was the first instrument to enable imaging of the topography of a flat sample surface with atomic resolution. Within only one year of its invention, the STM contributed to solving one of the most

intriguing problems in surface science at that time: The adatom layer of the Si(111)-7×7 surface was imaged with STM [47], which helped to develop the dimer-adatom-stacking fault model for the 7×7 surface reconstruction [48]. This success led to a wide acceptance of the STM as a powerful new tool for surface investigations and consequently, in 1986, Binnig and Rohrer were awarded the Nobel prize for their invention (together with Ernst Ruska, constructor of the first electron microscope).

Despite the huge success of the STM, it suffers from a serious limitation: Because the STM uses the tunneling current flowing between the tip and the sample as the imaging signal, STM studies are limited to conductive surfaces. Due to their high chemical reactivity and the permanent adsorption and desorption of molecules, most conductive surfaces are not suited for investigations under ambient conditions. Ultrahigh vacuum (UHV) is required to maintain them in a clean and well-defined state, which makes such experiments more challenging. It was noticed in the early STM experiments that significant forces acted between the tip and the sample at the close distances required for electron tunneling. This motivated Binnig to invent in 1985 a probe-based microscope that uses these forces as the imaging signal – the AFM. A first functional prototype was developed shortly afterwards, while Binnig and Gerber spent a sabbatical at Stanford University and the IBM San Jose Research Laboratory in California [49]. A new tool for surface investigation was therewith introduced, which enabled imaging of virtually any flat solid surface without the need for extensive surface preparation in UHV. Today, thousands of AFMs are in use in academic and industrial research laboratories and most of them are operated under ambient conditions.

The AFM is based on a tip mounted to a flexible beam called cantilever, which bends under the influence of a force acting on the tip. The first AFM used an additional STM tip mounted directly above the metalized back side of the cantilever to measure this bending. Today's AFM designs use other methods for sensing the tip displacement, among which optical methods (beam deflection, fiber interferometer) are still the most common. In recent years, however, self-sensing AFM sensors such as the qPlus quartz tuning fork sensor used in this thesis have also become more and more popular. After Binnig et al. had succeeded in recording with AFM the lattice image of a graphite surface under ambient conditions [50], Meyer and Amer presented atomically resolved AFM images of the NaCl(001) surface

recorded in UHV [51]. In these measurements, performed in the so-called contact mode, it was not possible to observe atomic defects like vacancies, and it was found that the typical tip load in contact AFM measurements exceeded the load limit of a single-atom junction [52]. Therefore, it was inferred that the contact area should be larger than the size of a single atom, implying that true atomic resolution could hardly be achieved with contact mode AFM. In 1995, one decade after the invention of the AFM, Giessibl [29] and Kitamura and Iwatsuki [53] finally achieved true atomic resolution on the reactive Si(111)-7 $\times$ 7 surface using noncontact AFM with a frequency modulation detection scheme [28].

Since the invention of scanning probe microscopy, a large family of instruments based on STMs and AFMs has been developed. While the pure imaging capabilities were initially the dominant application of scanning probe microscopes, new scanning probe techniques have enabled quantitative investigations of various physical properties with nanometer or even subnanometer resolution. Electrostatic force microscopy [54] measures the electrostatic interaction, Kelvin probe force microscopy [55] the local work function difference and scanning capacitance microscopy [56] the local capacitance between the tip and the sample. Furthermore, magnetic force microscopy [57] and spin-polarized STM [58] are used to probe magnetic properties on the atomic scale.

2.2 Scanning tunneling microscopy

The STM is based on the principle of electrons tunneling between two conductive electrodes, which are spaced apart by a few nanometers or less. This quantum mechanical phenomenon was first observed by Giaever [59]. He showed that if a voltage was applied to two metals separated by a thin insulating oxide film, a tunneling current could be measured between the electrodes, yielding insight into the electron density of states of superconducting solids. Instead of the oxide film, the electrons can also tunnel through a vacuum barrier. Binnig and Rohrer combined this phenomenon with the possibility of lateral scanning of a local probe to create the STM.

A schematic showing the basic setup of an STM is shown in Fig. 2.1a: A sharp metal tip is positioned at a distance of typically less than 1 nm

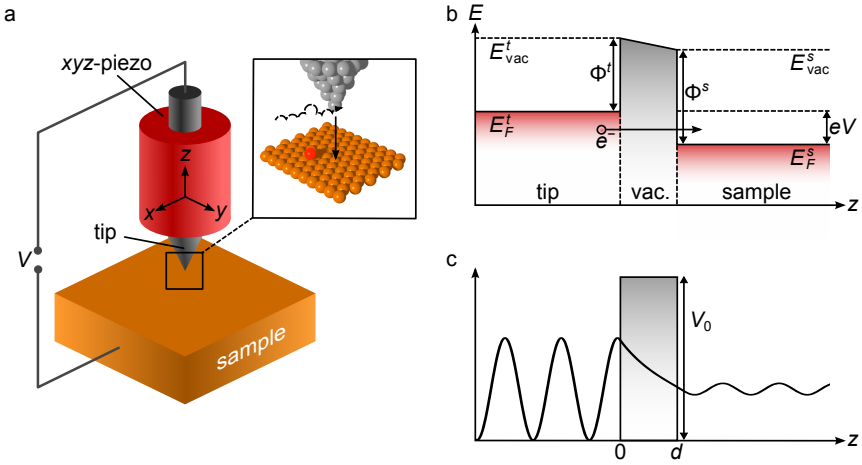

Fig. 2.1 Functional principle of STM. **a**, A sharp tip is scanned over the sample surface at a distance of typically less than 1 nm. The inset shows a microscopic representation of the atomic structure of the tip and the substrate. **b**, Schematic energy diagram of the tip/vacuum/sample system. E_F^t and E_F^s are the Fermi energies, $E_{\rm vac}^t$ and $E_{\rm vac}^s$ the vacuum levels, and Φ^t and Φ^s the work functions of the tip and the sample, respectively. The voltage V applied to the sample lowers the energy of the electron states in the substrate, enabling the tunneling of electrons across the vacuum barrier. **c**, Real part of the particle wave function in one dimension, for the case of a rectangular tunneling barrier of width d and height V_0. The particle is traveling from left to right.

above the conductive sample surface and a voltage in the range of a few V is applied. Because the potential barrier of the vacuum gap is greater than the energy of the electrons, in the classical picture no current could flow between the tip and the sample. It is known since the 1920s, however, that quantum mechanical particles have a certain probability of crossing a classically forbidden potential barrier, an effect known as quantum tunneling [60]. A particle's wave function decays exponentially across a potential barrier. Therefore, there is a small but nonvanishing probability of finding the particle on the other side of the barrier. The tunneling currents measured in STM are typically in the pA to nA range and depend exponentially on the tip–sample distance. A rule of thumb says that the tunneling

current is reduced by one order of magnitude when the vacuum gap between the tip and the sample is increased by one Å. An energy diagram of the tip/vacuum/sample system is shown in Fig. 2.1b, and the one-dimensional wave function for a rectangular potential barrier is shown in Fig. 2.1c.

For STM imaging, the tip is scanned line-by-line over the sample surface. A precisely controlled motion of the tip is achieved using piezoelectric translators (alternatively, the tip can be held fixed and the sample is scanned; the principle remains the same). A voltage applied across a piezoelectric material causes a change in the crystal structure that leads to a contraction of the piezo element in some directions and an expansion in the others. This piezoelectric effect can be used to build very precise scanning devices. Piezo tube scanners [61], which are today most widely used in scanning probe instruments, can easily achieve subnanometer positioning accuracy, provided that sufficient damping of external vibrations is ensured.

In the most commonly used STM imaging mode, the constant-current mode, the tunneling current is kept at a constant preset value during the scanning of the tip. This is achieved by adjusting the z distance with a feedback control loop that can contain integral, proportional, and derivative terms (PID controller). The z displacement of the tip, given by the voltage applied to the piezoelectric drive, then represents the imaging signal. A topographic map $z(x, y)$ of the sample is thereby recorded and can be displayed using a dedicated STM imaging software. A second imaging mode is the constant-height mode, where the tip is scanned in a plane parallel to the sample surface – irrespective of the local corrugation of the sample – while the tunneling current is being recorded. This mode does not need a z feedback controller and the imaging speed is therefore only limited by the bandwidth of the current detector. However, imaging in constant-height mode is only possible when investigating atomically flat sample surfaces, and a low drift rate and good vibration damping is needed to prevent the tip from crashing into the sample.

2.2.1 Theory of scanning tunneling microscopy

The contrast in constant-current STM images depends not only on the topography but also on the detailed electronic structure of the sample. This is the reason why the interpretation of STM images is often not straightforward. For a better understanding of the tunneling process in STM,

we give a brief introduction to its theoretical description. A first schematic approach to electron tunneling treats the problem as one-dimensional and assumes a rectangular potential barrier of height V_0 and width d (Fig. 2.1c). The solution of the corresponding time-independent Schrödinger equation is of the form

$$\psi(z) = \begin{cases} A_1 \mathrm{e}^{\mathrm{i}kz} + A_2 \mathrm{e}^{-\mathrm{i}kz} & \text{for } z < 0 \\ B_1 \mathrm{e}^{Kz} + B_2 \mathrm{e}^{-Kz} & \text{for } 0 \leq z \leq d \\ C \mathrm{e}^{\mathrm{i}kz} & \text{for } z > d \ , \end{cases} \tag{2.1}$$

for a particle traveling from left to right with energy $E < V_0$. The wavenumbers k and K are given by $k = \sqrt{2mE/\hbar^2}$ and $K = \sqrt{2m(V_0 - E)/\hbar^2}$, where m is the mass of the particle. The coefficients A_1, A_2, B_1, B_2, C are determined by requiring that the wave function be continuous and continuously differentiable. The transmission coefficient $T = |C|^2 / |A_1|^2$, which describes the probability of the incoming particle to be transmitted across the barrier, is calculated as [62]:

$$T = \frac{1}{1 + \frac{V_0^2 \sinh^2(Kd)}{4E(V_0 - E)}} \ . \tag{2.2}$$

The transmission through a rectangular barrier is thus found to be nonvanishing even for $E < V_0$. Equation 2.2 can be further simplified for the case of a very high tunneling barrier, $Kd \ll 1$:

$$T \approx \frac{16E(V_0 - E)}{V_0^2} \mathrm{e}^{-2Kd} \ . \tag{2.3}$$

The transmission probability decreases exponentially with increasing barrier width. This exponential distance dependence also applies to the tunneling current and is fundamental for the high resolution obtained with STM.

While the above considerations are sufficient to explain the exponential distance dependence of the tunneling current, for a quantitative description of the phenomenon of electron tunneling, a three-dimensional description is required as shown by Bardeen [63]. In Bardeen's approach, the tip and the sample are treated as separate entities. The transition probability between the unperturbed tip states and the unperturbed sample states is calculated

by considering the proximity of the tip to the sample as a perturbation potential and applying time-dependent perturbation theory. The tunneling current is then given to first order by:

$$I = \frac{2\pi e}{\hbar} \sum_{\mu,\nu} \{f(E_\mu)[1 - f(E_\nu + eV)] - f(E_\nu + eV)[1 - f(E_\mu)]\} \times \\ \times |M_{\mu\nu}|^2 \, \delta(E_\mu - E_\nu) \; . \tag{2.4}$$

The summation runs over the electron states in the tip (index μ) and the sample (index ν), with energies E_μ, E_ν. The Fermi function f describes the occupation of the states, V denotes the bias voltage applied to the sample and $M_{\mu\nu}$ is the transition matrix element between the electron state χ_μ in the tip and the electron state ψ_ν in the sample. The factor containing the Fermi functions represents the fact that tunneling can only occur from occupied to unoccupied states, and the delta function ensures that the principle of energy conservation is satisfied. It should be noted that χ_μ and ψ_ν in Eq. 2.4 are eigenstates of different Hamiltonians, in contrast to ordinary first-order perturbation theory. In the case of low temperatures (room temperature or below) and small voltages ($\sim 10\,\mathrm{mV}$), the last equation can be approximated by:

$$I \approx \frac{2\pi e^2 V}{\hbar} \sum_{\mu,\nu} |M_{\mu\nu}|^2 \, \delta(E_\mu - E_F)\delta(E_\nu - E_F) \; . \tag{2.5}$$

In this case, only electrons at the Fermi level E_F contribute to the tunneling current. When using Eq. 2.5 to calculate the tunneling current between the tip and the sample, the essential difficulty is the calculation of the matrix element $M_{\mu\nu}$. It can be expressed as [63]:

$$M_{\mu\nu} = \frac{\hbar^2}{2m} \int \mathrm{d}\boldsymbol{S} \cdot (\chi_\mu^* \boldsymbol{\nabla} \psi_\nu - \psi_\nu \boldsymbol{\nabla} \chi_\mu^*) \; , \tag{2.6}$$

where the integral is over an infinite surface within the tunneling region between the tip and the sample.

Starting from Bardeen's formalism of electron tunneling, Tersoff and Hamann developed a theory that enabled the interpretation of STM images [64]. They assumed the tip to be locally spherical and used s-like wave

functions for the tip states. By inserting this assumption into Eq. 2.6, the following result for the tunneling current between the tip and the sample is obtained:

$$I = \frac{32\pi^3 e^2 V(\Phi^s)^2 D_{\mathrm{tip}}(E_F) R^2}{\hbar\kappa^4} \mathrm{e}^{2\kappa R} \sum_{\nu} |\psi_\nu(\boldsymbol{r}_0)|^2 \, \delta(E_\nu - E_F) \ , \qquad (2.7)$$

where $\kappa = \sqrt{2m\Phi^s/\hbar^2}$ with the work function Φ^s of the sample surface. $D_{\mathrm{tip}}(E_F)$ denotes the tip density of states at the Fermi level, and $\boldsymbol{r}_0$ and R are the center and the radius of the tip curvature, respectively. The important conclusion from the last equation is that the tunneling current is proportional to the sample local density of states (LDOS) $\rho(\boldsymbol{r}_0, E_F)$ at the Fermi level at the position of the tip. The LDOS at position $\boldsymbol{r}$ is in general defined as:

$$\rho(\boldsymbol{r}, E) = \sum_{\nu} |\psi_\nu(\boldsymbol{r})|^2 \delta(E_\nu - E) \ . \qquad (2.8)$$

Therefore, if the assumption of s-wave tip states is justified, constant-current STM images show topographic maps of constant sample density of states.

2.3 Atomic force microscopy

In AFM, the imaging signal is given by the force between the scanning probe tip and the sample, rather than the tunneling current. Therefore, AFM is not restricted to conductive tip and sample materials. The central element of an AFM and its main difference compared to an STM is the flexible beam that senses the force acting between the tip and the sample (Fig. 2.2a). The first cantilevers were made from gold foil with a small diamond tip attached to it [49]. The probes used in AFM today are mainly built by microfabricating cantilevers with integrated tips from silicon [65]. A cantilever is characterized by its spring constant k, its eigenfrequency f_0 and its quality factor Q. The latter describes the width of the resonance peak of the cantilever and is defined as $Q = f_0/\delta f$, where δf is the bandwidth of the resonance.

The most common detection scheme used for sensing the deflection of the cantilever is measuring the displacement of a laser beam reflected off the back side of the cantilever [66]. This is achieved with a photosensitive

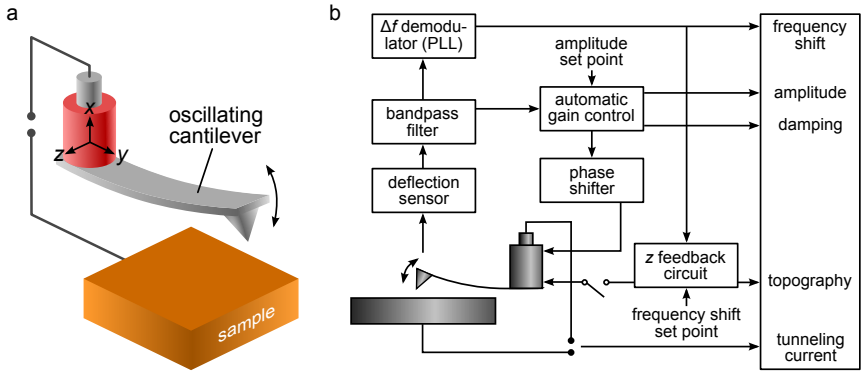

Fig. 2.2 Functional principle of frequency modulation AFM. **a**, A sharp tip mounted to a flexible cantilever is scanned over the sample surface at a distance of typically less than 1 nm. The cantilever is mechanically excited to oscillate at its resonance frequency and the shift of this resonance induced by tip–sample forces is the imaging signal. **b**, Schematic diagram of the frequency modulation AFM feedback loop. The physical observables are listed in the box to the right. The z feedback loop can be open (constant-height mode) or closed (constant-frequency mode).

diode that is divided in four sectors. When the cantilever is deflected, the laser spot on the photodiode is shifted and this generates different values of the photocurrent in the four segments. The AFM used in this thesis employs a different deflection detection scheme based on the piezoelectric properties of the quartz tuning fork used as the force sensor instead of a silicon cantilever [67].

There are basically two different modes of operation in AFM: the contact (static) and the noncontact (dynamic) mode. In contact mode, the force F acting on the probe simply translates into a static deflection $q = F/k$ of the cantilever. The range of useful values of k is limited by the requirement that the deformation of the cantilever should be significantly larger than the deformations of the tip and the sample. Depending on the system to be investigated, typical values for k in the static mode range from 0.01 N/m to 5 N/m. As mentioned above, atomic resolution imaging was achieved with contact AFM. It turned out, however, that the contrast mechanism was not the imaging of single atoms, but rather scanning with a tip that had a

large contact area with the sample and a periodicity commensurate to that of the sample. Therefore, no atomic defects could be observed. While it is difficult to achieve high resolution in contact mode, the interpretation of the measured data is straightforward: When a feedback control loop is used to keep the cantilever deflection constant during the scan, a topography $z(x, y, F = \text{const.})$ of constant force is recorded.

In noncontact AFM, the cantilever is excited by a mechanical actuator to oscillate at its resonance frequency f_0. This enables stable operation at close tip–sample distances, without the tip making contact to the sample. It also has the advantage that low-frequency noise ($1/f$ noise) can be filtered out using a bandpass filter centered around f_0. There are two basic methods of dynamic operation: amplitude modulation (AM) [68] and frequency modulation (FM) [28]. In AM-AFM, the actuator is driven at fixed frequency with fixed amplitude. When the tip is approached to the sample, the amplitude of the cantilever oscillation changes due to the interaction with the sample. Therefore, the amplitude can be used as the feedback signal for imaging the sample surface. The amplitude change in AM mode occurs on a timescale of $\tau \approx 2Q/f_0$. With Q values reaching 10^5 or more in UHV, the AM mode is very slow. This problem is circumvented by the FM mode, where a feedback loop ensures that the cantilever is oscillating with constant amplitude. In FM-AFM, the deflection signal is routed through a bandpass filter, phase shifted and fed back to the actuator, as shown in Fig. 2.2b. A phase-locked loop (PLL) determines the oscillation frequency $f = f_0 + \Delta f$, and the frequency shift Δf is used as the imaging signal.

Whereas atomic resolution was achieved with STM soon after its invention, it took a whole decade before true atomic resolution was demonstrated with AFM. There are various reasons that make atomic resolution more difficult to achieve with AFM: (i) In AFM, there is the problem of the so-called jump to contact or snap-in of the cantilever. When the tip is approached to the sample, for distances larger than the equilibrium distance of the chemical interaction the tip will be subject to an attractive force. Because the tip of an AFM is mounted to a flexible cantilever, this attraction can lead to a sudden jump of the tip into contact with the sample. The dynamic mode helps eliminating this problem: jump to contact is avoided, if $kA > \max(-F)$, that is by using a stiff enough cantilever or a large enough oscillation amplitude. (ii) Whereas the tunneling current is always increasing

with decreasing tip–sample distance, the force has a nonmonotonic distance dependence: it is attractive for larger distances and becomes repulsive for small distances. The consequence is that stable z feedback is only possible on one branch of the curve, usually the part with positive slope. This problem can be circumvented by operating in constant-height mode. However, this is only feasible if working at low temperatures, where thermal drift is minimal. (iii) The force between the tip and the sample is composed of different contributions, some of which are long-ranging and do not vary on the atomic scale. To achieve atomic resolution, it is desirable to filter out these long-ranging contributions. In STM, this problem does not occur, because the rapid exponential decay of the tunneling current eliminates all contributions to the current but the one from the tip atom closest to the sample. In the static mode, long- and short-ranging forces cannot be distinguished. In the dynamic mode, the long-ranging contributions can be attenuated by using a small oscillation amplitude [45].

2.3.1 Theory of atomic force microscopy

We now derive the relation between the force acting on the AFM tip and the oscillation frequency of the cantilever, which is recorded as the imaging signal in FM-AFM. Afterwards, we briefly discuss the different force contributions that are relevant in AFM.

The oscillating cantilever can be considered as a harmonic oscillator with a single degree of freedom. Its unperturbed motion is given by $q(t) = A\cos(2\pi f_0 t)$ with the resonance frequency $f_0 = (2\pi)^{-1}\sqrt{k/m'}$, where k is the spring constant and m' the effective mass of the cantilever. A force F between the tip and the sample causes a change in the effective spring constant. For amplitudes significantly smaller than the tip–sample distance z, this change is given by $k' = k - (\partial F/\partial z)$ [69]. By assuming the force gradient to be small compared to k, the following approximation for the frequency shift is obtained:

$$\frac{\Delta f}{f_0} = \frac{f - f_0}{f_0} = \frac{1}{2\pi f_0}\left(\sqrt{\frac{k'}{m'}} - \sqrt{\frac{k}{m'}}\right) \approx -\frac{1}{2k}\frac{\partial F}{\partial z} \ . \tag{2.9}$$

For small amplitudes, the frequency shift is approximately proportional to the force gradient. However, in many AFM studies larger amplitudes are

used. A more general expression for Δf for arbitrary amplitudes was derived using first-order perturbation theory in the Hamilton-Jacobi approach [69]:

$$\Delta f = -\frac{f_0^2}{kA} \int_0^{1/f_0} \{F(z + A[1 + \cos(2\pi f_0 t)]) \cos(2\pi f_0 t)\} \, \mathrm{d}t \tag{2.10a}$$

$$= -\frac{f_0}{\pi k A} \int_{-1}^{1} \left\{ F(z + A[1 + u]) \frac{u}{\sqrt{1 - u^2}} \right\} \mathrm{d}u \ . \tag{2.10b}$$

This relation can be used to calculate the frequency shift if the $F(z)$ dependence is known. More often, however, the force needs to be determined from a $\Delta f(z)$ curve obtained from an AFM measurement. An exact analytic inversion of Eq. 2.10 is not known, but there exist different approximative inversion procedures [70–73]. The most commonly used method is an analytical approximative approach developed by Sader and Jarvis [74, 75], which is easy to apply and yields excellent results over the whole range of amplitudes. They showed that the force can be expressed in terms of the frequency shift using the Laplace transform $\mathcal{L}$ and its inverse $\mathcal{L}^{-1}$:

$$F(z) = \mathcal{L}\left\{ \frac{kA}{T(\lambda A)} \mathcal{L}^{-1}\left[\frac{\Delta f(z)}{f_0} \right] \right\} \ , \tag{2.11}$$

with $T(x) = I_1(x)\exp(-x)$, where I_1 is a modified Bessel function. Using an approximative representation of $T(x)$,

$$T(x) \approx \frac{x}{2} \left(1 + \frac{1}{8}\sqrt{x} + \sqrt{\frac{\pi}{2}} x^{3/2} \right)^{-1} \ , \tag{2.12}$$

one arrives at the following expression for the force:

$$F(z) = \frac{2k}{f_0} \int_z^{\infty} \left\{ \left[1 + \frac{\sqrt{A}}{8\sqrt{\pi(t - z)}} \right] \Delta f(t) - \frac{A^{3/2}}{\sqrt{2(t - z)}} \frac{\partial[\Delta f(t)]}{\partial t} \right\} \mathrm{d}t \ . \tag{2.13}$$

In the case of the force spectroscopy measurements presented in Chapter 4 and 5, where we have a discrete set of experimental data points $\Delta f_i = \Delta f(z_i)$

for certain equidistant tip heights $z_i = z_1 + (i-1)\Delta z,\ i = 1 \ldots N$, we use the following discretized version of Eq. 2.13 to extract the corresponding force data $F_i = F(z_i)$:

$$F_i = \frac{2k}{f_0} \sum_{j=i+1}^{N} \left\{ \left[(1 + \frac{\sqrt{A}}{8\sqrt{\pi(z_j - z_i)}} \right] \Delta f_j - \frac{A^{3/2}(\Delta f_{j+1} - \Delta f_j)}{\sqrt{2(z_j - z_i)}\,\Delta z} \right\} \Delta z \ . \tag{2.14}$$

The method of Sader and Jarvis was shown to be very accurate: the maximum deviations from the actual force law were calculated for midrange oscillation amplitudes and were less than 5 % [74]. For the small amplitudes used in this work, the accuracy can be expected to be even better.

Next, we discuss the different contributions to the total force acting on the AFM tip in the proximity of the sample. In our UHV experiments, the van der Waals force and the electrostatic force with a range of several tens of nm and the chemical force with a range of several Å are relevant:

Van der Waals force The van der Waals (vdW) force is caused by fluctuations of the local dipole moment of atoms and the interaction of these dipoles with dipoles induced in nearby atoms. The vdW interaction is always attractive. For two atoms separated by a distance r, the vdW force goes as r^{-6}. The vdW force between two macroscopic bodies (like the tip and the sample in AFM) can be calculated with the Hamaker approach by integrating over the respective volumes with the assumption that the forces are additive and nonretarded [76]. For a spherical tip of radius R at a distance z from a flat surface, the Hamaker approach yields the following relation for the vdW force:

$$F_{\mathrm{vdW}} = -\frac{HR}{6z^2} \ , \tag{2.15}$$

where H denotes the material-dependent Hamaker constant. For a tip of radius $R = 50\,\mathrm{nm}$ at a distance of $z = 5\,\text{Å}$, the force according to Eq. 2.15 is typically on the order of 10 nN.

Electrostatic force Long-ranging electrostatic forces occur when there is a potential difference between a conductive tip and a conductive sample. The tip and the sample can be regarded as a capacitor with distance-dependent capacitance $C(z)$. The electrostatic force is then

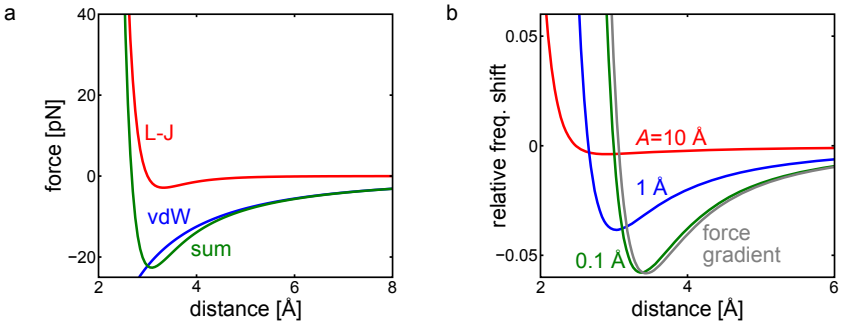

Fig. 2.3 Forces and frequency shifts in FM-AFM. **a**, Distance dependence of the Lennard-Jones force (red), the van der Waals force (blue), and their sum (green), calculated using the following parameters: $H = 2.5\,\text{eV}$, $R = 30\,\text{nm}$, $E_{\text{bond}} = 2\,\text{eV}$ and $z_{\text{min}} = 3\,\text{Å}$. **b**, Relative frequency shift $\Delta f/f_0$ calculated from the green force curve in **a** for different values of the oscillation amplitude: 10 Å (red), 1 Å (blue), and 0.1 Å (green). The relative frequency shift calculated from the force gradient according to Eq. 2.9 is shown in gray. A cantilever spring constant of $k = 1000\,\text{N/m}$ was assumed.

given by:

$$F_{\text{el.st.}} = \frac{1}{2}\frac{\partial C}{\partial z}(V - V^*)^2 \,, \tag{2.16}$$

where V is the voltage applied to the sample and V^* describes the contact potential difference between the tip and the sample ($V^* > 0$ means that the work function of the sample is greater than that of the tip). The term $\partial C/\partial z$ depends on the tip geometry, but is always negative. Like the vdW force, the electrostatic interaction is therefore always attractive. The tip can be modeled by a sphere of radius R on a truncated cone, which leads to the following expression for the electrostatic force valid for small distances ($z \ll R$) [77]:

$$F_{\text{el.st.}} = -\pi\epsilon_0\frac{R}{z}(V - V^*)^2 \,. \tag{2.17}$$

For typical experimental bias voltages, the electrostatic force is on the order of 1 nN, but it can be minimized by compensating the contact potential difference by choosing $V = V^*$. It should be noted that

there can also be short-ranging electrostatic contributions to the force, namely in the case of ionic crystal surfaces, where neighboring atoms carry charges of alternating sign. In this case, the electrostatic force decays exponentially with distance [78].

Chemical force The short-ranging chemical force starts to play a role at distances, where the overlap of the electron wavefunctions in the tip and the sample becomes significant. Chemical forces can be both attractive and repulsive, depending on the distance. A model potential commonly used to empirically describe the chemical force is the Lennard-Jones potential [79]:

$$V_{\mathrm{LJ}} = E_{\mathrm{bond}} \left[\left(\frac{z_{\mathrm{min}}}{z} \right)^{12} - 2 \left(\frac{z_{\mathrm{min}}}{z} \right)^{6} \right] , \tag{2.18}$$

where E_{bond} is the binding energy or potential minimum and z_{min} the equilibrium distance. The force corresponding to the Lennard-Jones potential is given by:

$$F_{\mathrm{LJ}} = -\frac{\partial V_{\mathrm{LJ}}}{\partial z} = 12 \frac{E_{\mathrm{bond}}}{z_{\mathrm{min}}} \left[\left(\frac{z_{\mathrm{min}}}{z} \right)^{13} - \left(\frac{z_{\mathrm{min}}}{z} \right)^{7} \right] . \tag{2.19}$$

The Lennard-Jones force is plotted in Fig. 2.3a for typical parameters, together with the vdW force. Fig. 2.3b shows the corresponding frequency shift, calculated from the sum of Lennard-Jones and vdW forces using Eq. 2.10 for different oscillation amplitudes. For decreasing amplitudes, the frequency shift approaches the force gradient curve (Eq. 2.9).

2.3.2 Kelvin probe force microscopy

Kelvin probe force microscopy (KPFM) is an AFM-derived technique that can measure the local work function of a sample surface. It is based on a method proposed by Lord Kelvin in 1898, in which the work function of a material is determined relative to the work function of a known reference material [80]. The basic principle of the Kelvin method is illustrated in Fig. 2.4: When two metals of different work functions Φ_1, Φ_2 are connected, their Fermi levels align, leading to a voltage drop $V^* = (\Phi_1 - \Phi_2)/e$ (the

contact potential) across the vacuum barrier between them. By applying a compensating voltage, the contact potential can be determined. In the original Kelvin method, the two metals are arranged as a parallel plate capacitor. The distance between the two plates is oscillated periodically and the work function difference leads to an ac current. To determine V^*, an additional dc voltage is applied, until the space between the plates becomes field-free and the current vanishes. While the Kelvin method can measure the contact potential with high sensitivity, it provides no lateral resolution of the local variation of the work function difference.

KPFM combines the high lateral resolution of AFM with the sensitivity to contact potential differences of the Kelvin method [55]. In KPFM, the electrostatic force between the two electrodes (given by the tip and the sample) is detected instead of the displacement current. In order to distinguish the electrostatic force from other contributions like the vdW force, a small ac voltage $V_{\mathrm{ac}} \sin(\omega_{\mathrm{ac}} t)$ is applied to the sample, in addition to the dc bias voltage V_{dc}. Inserting $V = V_{\mathrm{dc}} + V_{\mathrm{ac}} \sin(\omega_{\mathrm{ac}} t)$ into Eq. 2.16 yields:

$$\begin{aligned} F_{\mathrm{el.st.}} = & \frac{1}{2}\frac{\partial C}{\partial z}\left[(V_{\mathrm{dc}} - V^*)^2 + \frac{1}{2}V_{\mathrm{ac}}^2\right] \\ & + \frac{\partial C}{\partial z}(V_{\mathrm{dc}} - V^*)V_{\mathrm{ac}} \sin(\omega_{\mathrm{ac}} t) \\ & - \frac{1}{4}\frac{\partial C}{\partial z}V_{\mathrm{ac}}^2 \cos(2\omega_{\mathrm{ac}} t) \ . \end{aligned} \tag{2.20}$$

The force and the resulting frequency shift contain constant terms and terms oscillating with ω_{ac} and $2\omega_{\mathrm{ac}}$. The local contact potential difference (LCPD) is determined in KPFM by adjusting the dc voltage such that the first harmonic term vanishes. This is usually done during scanning with constant-Δf feedback, and there are two different experimental techniques to simultaneously measure the LCPD and the topography: amplitude modulation KPFM and frequency modulation KPFM [43].

As an alternative to the feedback scheme of KPFM, it is also possible to determine V^* directly from $\Delta f(V)$ spectra, without the additional ac voltage modulation. According to Eq. 2.16, such spectra should exhibit a parabolic behavior. The local contact potential difference is then determined by the position of the maximum of the $\Delta f(V)$ parabola. This method does

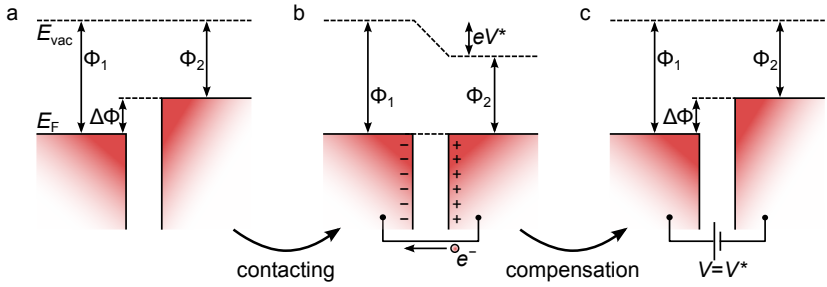

Fig. 2.4 Schematic illustration of the Kelvin principle. **a**, Two different metals which are not connected to each other share the same vacuum level E_{vac}. Their Fermi energies differ in general, corresponding to a difference $\Delta\Phi$ between the work functions of the two materials. **b**, When the two materials are connected, their Fermi levels align, accompanied by an electron flow to the material with the greater work function. This leads to a voltage drop $V^* = \Delta\Phi/e$ across the vacuum barrier. **c**, The contact potential difference can be compensated by applying a dc voltage $V = V^*$.

not offer the speed of KPFM as far as 2D imaging of the work function is concerned, because a complete spectrum has to be recorded for each point of interest. The simplicity of the method, however, makes the interpretation of the data more straightforward, and it offers a high sensitivity to small shifts of the contact potential difference. We use this method in Chapter 4 to determine local shifts of the LCPD above differently charged adatoms and in Chapter 8 to demonstrate 2D imaging of the charge distribution within a single molecule.

CHAPTER 3

Experimental details

All the measurements presented in this thesis were carried out using a low-temperature combined STM/AFM system that is a modified version of a commercially available instrument from Createc Fischer & Co. GmbH, which is based on a design by Gerhard Meyer [81]. The system was originally built as a pure STM system, and the AFM capabilities were later added following the qPlus tuning fork design [37, 82]. In this chapter, we briefly describe the detailed features of the STM/AFM system, and the tip and sample preparation methods used in our experiments.

3.1 UHV chamber and low-temperature STM/AFM

Our STM/AFM system is shown in Fig. 3.1a. The whole system is located in the basement of the building and is supported by four pneumatic vibration isolators, to reduce low-frequency mechanical vibrations. The stainless-steel ultrahigh vacuum (UHV) chamber consists of two parts separated by a gate valve. The left part is used for sample preparation, and the right part hosts the low-temperature scanning probe stage, which is attached to the helium bath cryostat. The preparation chamber is connected to a small loadlock chamber equipped with a turbomolecular pump, which is used for pumping during the bake-out of the system. After the bake-out, the system is pumped with a titanium sublimation pump and an ion getter

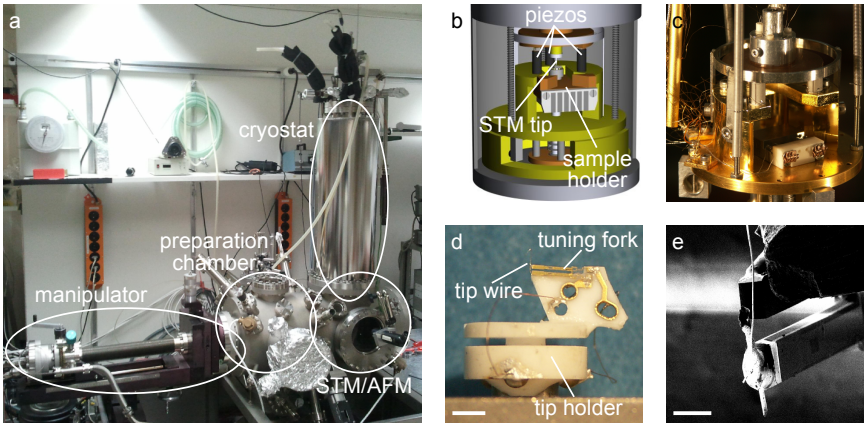

Fig. 3.1 The STM/AFM system used in this thesis. **a**, Photograph showing the UHV chamber. The preparation part of the chamber, the part containing the STM/AFM, the liquid nitrogen/liquid helium bath cryostat, and the coolable manipulator used for transferring samples are indicated. The loadlock is located behind and the titanium sublimation and ion getter pumps are located underneath the preparation chamber. **b**, Schematic drawing of the scanner stage. Image taken from ref. [83]. **c**, Photograph of the scanner stage. In contrast to **b**, no sample holder is inside the STM/AFM. **d**, Photograph of the tuning fork sensor, before cutting the PtIr tip wire with a focused ion beam. The tuning fork is glued with one prong to a rhomboid-shaped substrate, which is glued onto the transferable tip holder. A 10 μm Au wire (barely visible in the photograph) connects the tip wire to the lower left hole in the substrate. **e**, Focused ion beam microscope image of the tuning fork, after cutting the tip wire. Scale bars: 2 mm in **d** and 200 μm in **e**.

pump connected to the preparation chamber, and a base pressure in the UHV chamber below 10^{-10} mbar is routinely achieved. The preparation chamber is equipped with a mass spectrometer for residual gas analysis and a low-energy electron diffractometer (LEED) for surface characterization. For the sample preparation, there is an ion gun for sputter cleaning, and several crucibles from which different materials can be evaporated. Our single-crystal metal samples are mounted onto small resistive button heaters on the sample holders, with a NiCr/Ni thermocouple attached for controlling the temperature. The manipulator for transferring the samples inside the

preparation chamber and into the STM/AFM can be moved with high precision in all three directions and also rotated around its longitudinal axis (by means of a differentially pumped rotary feedthrough). Furthermore, it can be cooled with liquid nitrogen or helium, which enables a wide range of sample temperatures during the growth of materials. A sample storage inside the preparation chamber can store up to six samples, evaporators, or other tools mounted onto sample holders (for example a tool for transferring microscope tips).

The STM/AFM stage itself is based on the Besocke beetle design [84, 85]. It is shown schematically in Fig. 3.1b, and a photograph is shown in Fig. 3.1c. The STM tip (or in our case the tuning fork sensor) is attached to a copper disk which rests on three sapphire balls glued to PZT (lead zirconate titanate) piezo tubes. Using the principle of stick-slip motion, the disk can be moved by applying sawtooth-shaped voltage pulses to the quadrature electrodes of the piezos. Because the copper disk is not completely flat but has three slightly inclined planes on its bottom side, the sliding of the disk can also be used for a controlled vertical coarse motion of the tip. In our system, both the coarse positioning of the tip and the scanning are done with the three outer tube piezos. The whole STM/AFM is suspended by three springs and equipped with an eddy current damping system. For the cooling of the STM/AFM, the scanner stage is thermally (weakly) coupled to the liquid helium tank of the bath cryostat and enclosed by two radiation shields. The inner radiation shield is thermally connected to the helium tank and the outer one is connected to the surrounding liquid nitrogen tank. This system enables a continuous operation of the STM/AFM at a temperature of about 5 K (measured with a Si diode on the base plate of the scanner stage). The liquid nitrogen tank (15 l) and the liquid helium tank (4 l) have to be refilled every 48 hours and 72 hours, respectively.

As the AFM sensor, we use quartz tuning forks like the one shown in Fig. 3.1d,e. The tuning fork (type E158, as found in the DS26 crystals from Micro Crystal AG which are used for example in Swatch wristwatches) with oscillation frequency 32 768 Hz and theoretical spring constant 1 800 Nm^{-1} is firmly glued with one prong to an insulating ceramic substrate, following the qPlus design [82]. A piece of 25 μm PtIr wire is attached to the apex of the free prong to serve as the STM/AFM tip. To avoid crosstalk between the STM and AFM signals, a separate 10 μm Au tip wire is connected to the PtIr tip wire to measure the tunneling current independently of the

tuning fork electrodes used for deflection sensing [86, 87]. The whole sensor is mounted onto a MACOR tip holder, which can be transferred using the manipulator (that is without breaking the vacuum) when no sample is inside the microscope. The tuning fork is excited purely mechanically, by a small central piezo tube carrying the tip holder receptacle.

The STM/AFM is controlled using homebuilt electronics and a customized software. A high-voltage amplifier is used for driving the piezos and two operational amplifiers are used to amplify the tunneling current (gain 10^{10}) and the deflection signal of the tuning fork (gain 10^8). To ensure low noise operation, the op-amps are installed close to the microscope stage in UHV, on the outer radiation shield at liquid nitrogen temperature. For the tunneling current signal, there is also an alternative variable-gain external amplifier, which can be used when high currents are to be measured or a higher bandwidth is required. A relay on the outer radiation shield is used to switch between the internal and external tunneling current amplifiers. The deflection signal of the tuning fork is further enhanced by an additional external amplifier (Stanford Research Systems SR560, gain 20). The bias voltage V is always applied to the sample, and the tip is held at virtual ground. The analog components of the electronics are all connected to a digital signal processor (DSP) board (Innovative Integration SBC6711), via two 18-bit analog-to-digital/20-bit digital-to-analog converter boards (one is used for the AFM operation exclusively). The phase-locked loop (PLL) needed for the AFM frequency feedback (see Chapter 2) is purely software-based and runs on the DSP board. To ensure a very low noise in the frequency shift signal even at sub-Å amplitudes, it is set to very small bandwidths ($\lesssim 10\,\mathrm{Hz}$) and accordingly, the tip has to be scanned very slowly during AFM operation (the high-resolution AFM images of molecules presented in Chapter 5 to 8 were typically recorded at scanning speeds of about $5\,\mathrm{Å s}^{-1}$). It should be noted that all the initial sample characterization and tip preparation were done in the STM mode, and only after obtaining a good tip and setting the right imaging area, etc., did we switch to the AFM mode. Our qPlus tuning fork system enables stable STM feedback at small currents ($I \lesssim 1\,\mathrm{pA}$) and AFM operation with oscillation amplitudes as small as 0.1 Å.

The scan piezos were initially calibrated by comparing the known interatomic distances in the copper fcc crystal structure to STM topographic

images of the Cu(111) surface, which showed either single atomic steps (z) or the atomically resolved positions of the topmost Cu atoms (x,y). The tip oscillation amplitude was calibrated using the instrument's capability of simultaneous STM and AFM operation: With closed STM feedback loop, we measured how the tip height changed when turning on the oscillation for different amplitude set points. Because of the exponential distance dependence of the tunneling current, for increasing amplitudes, the measured change of the tip height approaches a linear behavior as a function of the amplitude set point, which directly reflects the change of the real oscillation amplitude. The slope of the line fitted to the measured values therefore yields the desired conversion factor between the amplitude set point (in some arbitrary units) and the real oscillation amplitude.

3.2 Sample and tip preparation

The substrate used for all measurements presented in this thesis was a Cu(111) single crystal, which was cleaned in the UHV preparation chamber by repeated sputtering (15 to 20 minutes with 1 keV Ne ions) and annealing (to about 840 K) cycles. Next, the sample temperature was held at about 270 K (using the cooled manipulator), and submonolayer coverages of NaCl were evaporated from a resistively heated Ta crucible in the preparation chamber. This leads to the formation of (100)-terminated NaCl islands with a thickness of predominantly two atomic layers [88, 89]. The sample was then transferred into the microscope and the adsorbates to be investigated were deposited in situ. Metal atoms and different molecules were evaporated through small holes in the shutters of the radiation shields, at a sample temperature of about 10 K, where thermal diffusion on the surface is suppressed and the atoms and molecules mostly remain at their initial adsorption sites. For the evaporation of the organic molecules, we usually used a two-step process. First, the molecules were evaporated inside the loadlock onto a small piece of a Si wafer. Then, this wafer was positioned in front of the openings in the shutters and flash-heated to ~ 900 K by resistive heating. This procedure enables very clean sample preparations and several different kinds of molecules can be deposited on the same sample without getting too much contamination. To deposit single CO molecules on the surface, small pressures ($\sim 10^{-8}$ mbar) of CO were admitted into the UHV chamber

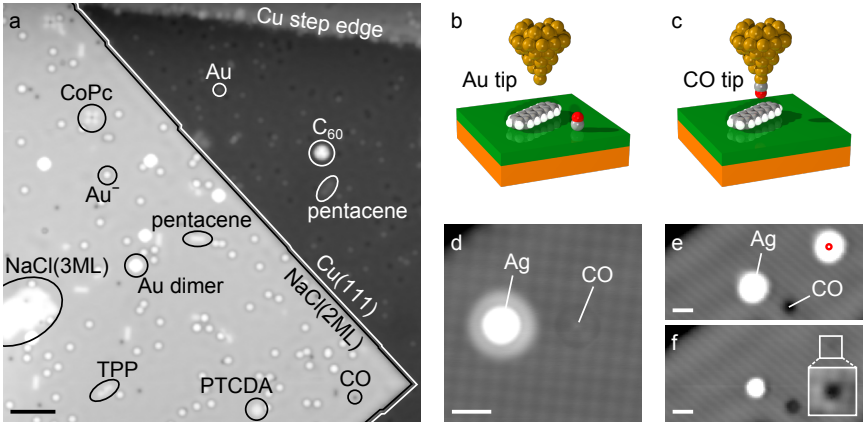

Fig. 3.2 Sample and tip preparation. **a**, STM constant-current overview image ($I = 2.5\,\text{pA}$, $V = 0.2\,\text{V}$) of a typical sample preparation. The Cu(111) substrate and a two-monolayer NaCl island (with a small patch of the third layer on top) can be identified. Different adsorbates have been deposited on the surface and can be distinguished from their appearance in the STM topography: Au monomers and dimers, CO, C_{60} fullerenes, terphenyl-pyridine (TPP), perylene (PTCDA), cobalt phthalocyanine (CoPc), and pentacene. **b**,**c**, Schematic representation of the creation of a CO tip. Upon approaching the sharp metal tip to a CO molecule on the NaCl(2ML)/Cu(111) surface, the molecule is transferred to the tip apex. During the transfer of the molecule, a rotation by 180° occurs. **d**, Typical STM image ($I = 4\,\text{pA}$, $V = 0.2\,\text{V}$) recorded with a CO tip. Enhanced resolution of the NaCl surface is observed, as well as a characteristic appearance of the adsorbates. **e**,**f**, STM images ($I = 2.3\,\text{pA}$, $V = 0.2\,\text{V}$) before (**e**) and after (**f**) creation of a Cl tip by picking up a AgCl complex from the NaCl surface. The inset ($I = 4\,\text{pA}$, $V = 0.2\,\text{V}$) shows that a single Cl vacancy was created. Scale bars: 50 Å in **a** and 10 Å elsewhere.

and the shutters in the radiation shields were opened for a few seconds. An STM overview image of a typical sample preparation is shown in Fig. 3.2a, showing a two-monolayer NaCl island on Cu(111) [NaCl(2ML)/Cu(111)] with different atomic and molecular adsorbates.

The tips for high-resolution STM and AFM measurements were prepared in several steps: Before installing the tuning fork sensor in the STM/AFM, a focused ion beam (FIB) was used to shorten and sharpen the PtIr tip wire

(see FIB image in Fig. 3.1e). After transferring the tip into the microscope, the tip was repeatedly indented into the Cu substrate, until a stable tip favorable for both STM and AFM measurements resulted. After each tip crash, we checked the quality of STM images (for example, adatoms should appear as sharp circular protrusions) and $I(V)$ spectra (no strange unidentifiable features should be present). A good indicator for a tip suitable for high-resolution AFM imaging was found to be a small negative frequency shift at a certain STM set point height (on the order of $-1\,\mathrm{Hz}$ at a set point of $I = 2\,\mathrm{pA}$, $V = 0.2\,\mathrm{V}$ over the bare substrate). The small frequency shift corresponds to a weak long-ranging attractive interaction, and the tip is presumably very sharp. Starting from such a sharp metal tip (that is most likely covered with Cu), we would then pick up different molecules and atoms from the surface. These controlled tip modifications on the single-atom/single-molecule level were found to strongly modify (and often enhance) the contrast in STM and AFM imaging, which is a central result of this thesis. In particular, we created the following tips:

Au/Ag tip To pick up single Au or Ag atoms from the surface, the tip was first positioned above the center of an Au or Ag adatom on NaCl(2ML)/Cu(111). After switching the feedback off, the tip was approached by about 4 Å from the typical STM set point of $I = 2\,\mathrm{pA}$, $V = 0.2\,\mathrm{V}$, and the successful pickup of the atom was observed as a sudden jump in the tunneling current. The Au or Ag tip terminations yielded qualitatively the same contrast as the Cu tip, but picking up several single adatoms was found to be a good way to fine-tune the tip until the highest possible STM resolution could be achieved.

CO tip The creation of a CO tip is shown schematically in Fig. 3.2b,c. After preparing a sharp Cu, Ag, or Au tip, the tip was positioned above a single CO molecule on NaCl(2ML)/Cu(111) and the feedback loop was opened. By approaching the tip by about 3 Å from the STM set point, the CO molecule was often picked up, which we observed as a sudden decrease in the tunneling current. After switching the STM feedback back on, the tip height corresponding to the STM set point above the bare NaCl would be about 0.5 Å to 1.7 Å closer to the substrate. Subsequent STM imaging showed a very characteristic contrast, with enhanced atomic resolution of the NaCl substrate and diffuse bright halos around admolecules and adatoms (symmetric

halos as in Fig. 3.2d are an indication for a good CO tip). It is known that CO forms a bond with metal predominantly through the carbon, and a 180° rotation of the CO occurs in the transfer [10, 90, 91]. An alternative method for preparing a CO tip without the need for the insulating NaCl layer is to pick up the CO directly from the Cu(111) substrate by applying a voltage pulse of about $V = 2.5\,\mathrm{V}$ [91].

Cl tip When picking up a single Ag adatom from NaCl(2ML)/Cu(111), in the subsequent STM image sometimes a Cl vacancy [92] appeared at the former adsorption site of the adatom (Fig. 3.2e,f). Together with the fact that the subsequent STM images showed strongly modified contrast (enhanced atomic resolution of the NaCl, metal adatoms appear with reduced diameter), this led us to the conclusion that an AgCl complex was picked up, with the Cl atom at the very apex of the tip. An alternative method for preparing a Cl tip is to approach the tip towards the bare NaCl surface until a jump in the tunneling current indicates a modification of the tip. Subsequent STM imaging of the area then often confirms the creation of a Cl vacancy and shows the characteristic Cl-tip contrast.

Pentacene tip A tip terminated with a single pentacene molecule can be created by approaching the tip towards a single pentacene molecule on NaCl(2ML)/Cu(111), until a sudden discontinuity in the tunneling current indicates the transfer of the molecule. The pentacene tip has been shown in previous studies to give enhanced resolution in STM imaging of molecular orbitals [25, 93] and to facilitate the lateral manipulation of molecules on thin insulating films [27].

CHAPTER 4

Measuring the charge state of single atoms with AFM

It was shown that Au atoms adsorbed on a bilayer NaCl film on Cu(111) occur in two different charge states [17]. These charge states, which could be identified as the neutral adatom (Au^0) and the singly negatively charged adatom (Au^-), showed a distinctively different contrast when imaged with STM (Fig. 4.1c). Moreover, it was demonstrated that the adatoms can be switched between the two charge states in a controlled and reversible manner. This charge switching was achieved by applying voltage pulses of appropriate polarity, with the STM tip positioned directly above the adatom (Fig. 4.1a-d). First-principle DFT calculations traced back the origin of the observed charge bistability to ionic relaxations in the underlying NaCl film (Fig. 4.1e,f). The calculations showed that the neutral Au^0 adsorbs directly on top of a Cl^- ion and leaves the NaCl lattice almost unperturbed. The negatively charged Au^-, on the other hand, is 0.4 Å closer to the surface and the underlying Cl^- and Na^+ ions are relaxed towards and away from the substrate, respectively. Further studies have revealed that different charge states also occur for other metal adatoms (Ag, Cu, Pd) and on other thin insulating films (MgO), which emphasizes the universality of the phenomenon [94–96]. Particularly interesting is the fact that Ag adatoms on a thin NaCl film occur in three different stable charge states (Ag^0, Ag^- and Ag^+) that can be switched from one to another [94].

In view of future investigations of the charge distribution or charge transport in molecular complexes on thicker insulating films, it would be

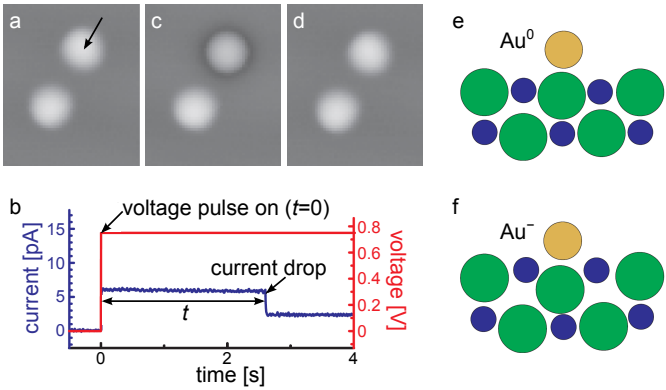

Fig. 4.1 Charge state switching with an STM tip, as reported in ref. [17]. **a**, Constant-current STM image showing two neutral gold adatoms adsorbed on NaCl(2ML)/Cu(111). **b**, The STM tip was positioned above one of the adatoms (arrow) and a positive voltage pulse was applied to the sample. After a certain time, a sudden drop of the tunneling current indicated the switching of the atom. **c**, The switching event was confirmed by the subsequent STM image. **d**, By applying a negative voltage pulse, the adatom was switched back to its original neutral state. **e**,**f**, Side view of the DFT-calculated atomic positions for the neutral (**e**) and negatively charged (**f**) adatom. Gold, sodium, and chlorine atoms are colored in yellow, blue, and green, respectively. All images reproduced from ref. [17].

desirable to have a method for detecting single electron charges that does not require a conducting tunneling junction. Previous electrostatic force measurements have shown that single-electron charge sensitivity can be achieved with noncontact AFM [97–102]. However, because of the large cantilever oscillation amplitudes (typically several nm) used in these studies, the sensitivity to short-range forces and the spatial resolution was limited. Here we demonstrate that the sub-Å amplitudes achievable with our qPlus tuning fork setup enable the combination of single-electron charge sensitivity with atomic-scale lateral resolution.

In addition to exerting an electrostatic force on the AFM tip, localized charges on surfaces lead to variations in the work function, which are reflected in local changes of the contact potential difference between the tip and the substrate [103, 104]. As described in Chapter 2.3.2, the method of

choice for mapping the local contact potential difference (LCPD) is Kelvin probe force microscopy (KPFM). In recent years, KPFM has been pushed to the atomic scale, making it a promising approach for the mapping of charge distributions with ultimate lateral resolution [105–109].

In this chapter, we first show that Au^0 and Au^- can be distinguished in constant-height AFM images [110]. A difference in the attractive tip–sample force is responsible for the contrast between the differently charged adatoms. This force difference is derived quantitatively from frequency shift versus distance measurements. Next, we investigate the influence of charge switching on the LCPD by analyzing $\Delta f(V)$ spectra recorded above the different adatoms (corresponding to a KPFM measurement). These measurements, which were also performed for Ag adatoms, show that the positively charged Ag^+ can be distinguished from its neutral counterpart Ag^0, too. We end this chapter by a discussion of our results in terms of a simple model, which assumes that the double-barrier tunnel junction can be modeled by a series of capacitances.

4.1 Charge state detection by AFM imaging

In Fig. 4.2, the possibility of distinguishing single adatoms in the neutral and negative state by AFM imaging is demonstrated. After preparing a sharp metal tip with the procedures described in the previous chapter (a schematic representation of the tip and sample geometry is shown in Fig. 4.2a), we imaged two nearby Au adatoms on NaCl(2ML)/Cu(111) in constant-current STM mode (Fig. 4.2b). One of them was identified as Au^- by its characteristic surrounding depression and its smaller apparent height ($h_{Au^-} \approx 1.5$ Å versus $h_{Au^0} \approx 2.2$ Å, in good agreement with ref. [17]), whereas the other was in the neutral state (compare Fig. 4.1c). Then, the feedback loop was opened and the same atoms were imaged again in constant-height mode, with the current (Fig. 4.2c) and frequency shift (Fig. 4.2d) signals being recorded simultaneously. After switching the current feedback back on, another constant-current image was taken to confirm that no unintended switching of the adatoms and no tip change had occurred during the measurement. In constant-height mode, a larger tunneling current was measured above Au^0 than above Au^-, in accordance with the larger apparent height of Au^0 in the constant-current image. In the Δf

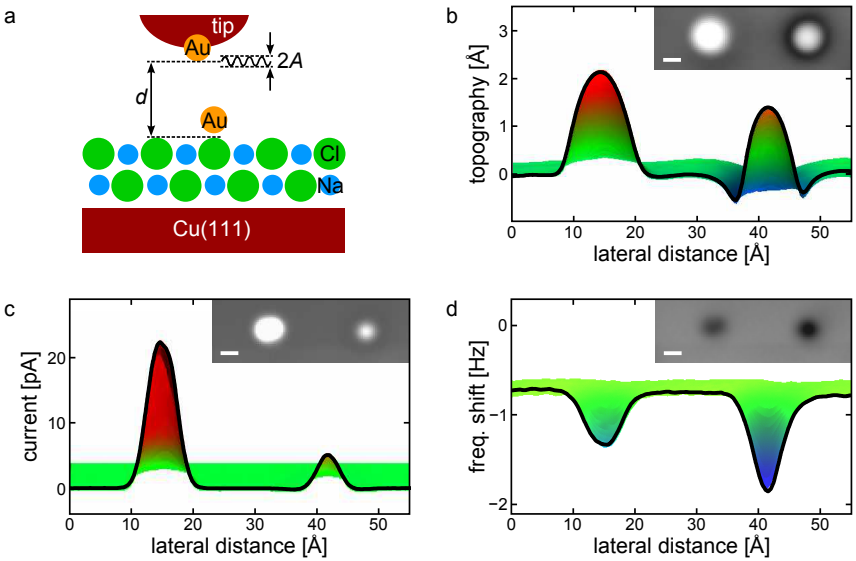

Fig. 4.2 Charge state determination with AFM. **a**, Schematic illustration of the tip and sample system: single Au adatoms on NaCl(2ML)/Cu(111) are imaged with a Au-terminated tip. The tip oscillates with constant amplitude A. **b-d**, Constant-current topography (**b**) and constant-height scans (**c**,**d**) above Au^0 (left) and Au^- (right). In the constant-height mode, the current (**c**) and frequency shift (**d**) signals were recorded. The line scans in **b-d** were taken through the centers of the two adatoms visible in the 2D maps shown as insets. Imaging parameters: $I = 2\,\text{pA}$, $V = -50\,\text{mV}$ in **b**, and $d = 5.0\,\text{Å}$, $A = 0.3\,\text{Å}$, $V = -5\,\text{mV}$ in **c**,**d**. Low-pass filtering was applied to the images, and the color scale in **b-d** corresponds to a three-dimensional representation of the insets, cut along the line profile. Scale bars in the insets: 5 Å.

image (inset of Fig. 4.2d), both atoms appear as circular depressions with a diameter (full width at half maximum) of approximately 6 Å. A significantly greater absolute value of the frequency shift was measured above Au^- than above Au^0 ($\Delta f_{Au^-} = -1.86\,\text{Hz}$ as compared to $\Delta f_{Au^0} = -1.39\,\text{Hz}$). In these measurements, the constant-height mode was important to exclude the different height in the constant-current topography as the source of the Δf contrast. Furthermore, the tip had to be scanned at a distance,

where the interaction with the adatoms was sufficiently small to prevent unintended manipulations such as charge switching or lateral manipulation. We conclude that the distinction of neutral and negatively charged atoms is possible with AFM and should therefore also be feasible on thicker insulating layers, where STM can not be used.

However, this result still has to be considered in the context of the above-mentioned relaxation of the Au adatom towards the substrate upon switching to the negative state. The difference in the tip–adatom distance will also affect the measured frequency shift. To exclude that the different appearance of Au^0 and Au^- in the constant-height Δf images is just caused by a topographic effect, in the next paragraph we present further investigations of the distance dependence of the frequency shift. With the knowledge of this distance dependence we can also quantify the difference in the forces exerted on the AFM tip above Au^0 and Au^-, respectively.

4.2 Forces above differently charged adatoms

The measurements presented in this paragraph were performed on the same two Au adatoms as the ones shown in Fig. 4.2. No tip change or change of the adsorption sites of the adatoms was observed during the complete set of measurements. Using constant-height AFM mode, we recorded the frequency shift along a line through the centers of the two adatoms for decreasing values of the tip–sample distance ($4.8\,\text{Å} < d < 11.0\,\text{Å}$, for the definition of the absolute distance d, see Appendix A[1]). We extracted the vertical force from these line scans using the following procedure: (i) The raw data (circles in Fig. 4.3a) were smoothed by adjacent averaging. We averaged over 3.0 Å in x for the four largest distances and over 1.4 Å for the other distances (averaged data are shown as solid lines in Fig. 4.3a). (ii) At each lateral position x, the distance dependence of Δf was fitted with a piecewise cubic Hermite polynomial, which yielded a continuous and continuously differentiable fit (Fig. 4.3b). (iii) We applied the method

1 Here and in the following chapters, z denotes the vertical coordinate in general, which for the experimental data is usually measured from a certain STM set point. On the other hand, d always refers to an absolute tip–sample distance, either defined in calculations or by some experimental calibration measurement as in Appendix A.

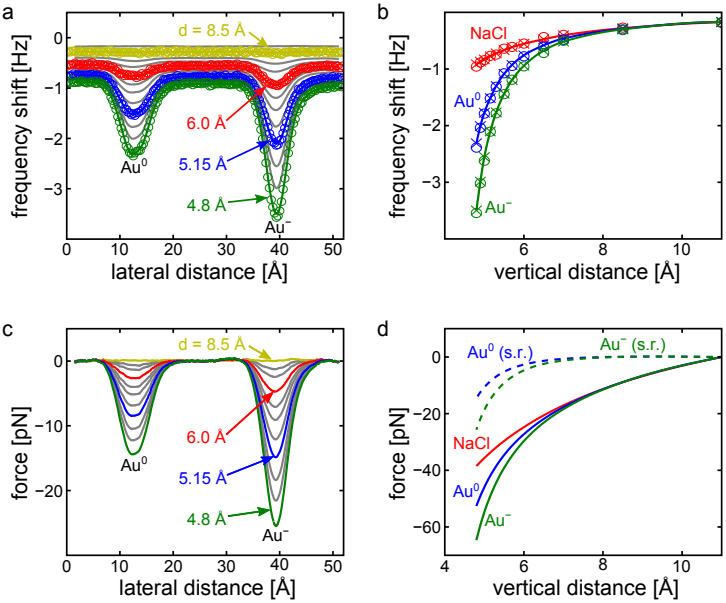

Fig. 4.3 Forces above Au^0 and Au^-. **a**, Constant-height line scans of the frequency shift at different tip–sample distances ($A = 0.22$ Å, $V = -2$ mV). For some lines, every eighth point of the raw data is shown as a circle. Solid lines correspond to smoothed data. **b**, Corresponding $\Delta f(d)$ curves above Au^0 ($x = 12.4$ Å), above Au^- ($x = 39.4$ Å), and above the NaCl substrate ($x = 26.8$ Å). The raw data (circles), the smoothed data (crosses) and the polynomial interpolation (solid lines) are shown. **c**, Line scans of the vertical force extracted from the averaged data in **a**. The background force above the substrate has been subtracted. **d**, Force versus distance curves above the different sites. For the dashed lines, the background force above the substrate has been subtracted.

of Sader and Jarvis [74] (Eq. 2.14) to the resulting curves to obtain the vertical force F_z. (iv) To finally obtain the short-range contribution to the force caused by the adatoms only, we subtracted from each constant-height line profile of F_z the background force (the force measured over the NaCl at a lateral distance of more than 10 Å from the adatoms). The resulting line profiles of the vertical force exerted on the AFM tip by the Au^0 and Au^- adatoms are shown in Fig. 4.3c. In Fig. 4.3d, F_z is plotted as a function of

the distance above the different sites (Au^0, Au^- and the NaCl substrate). Both the total force and the background-subtracted short-range part are shown.

At the closest investigated distance ($d = 4.8$ Å), we measured an attractive force that was 11 pN greater above Au^- than above Au^0. The high sensitivity of our tuning fork sensor enabled the measurement of forces with a resolution of about 1 pN. Attempting to increase the force difference between the differently charged adatoms by approaching the tip further to the sample would result in unintended charge switching and/or lateral manipulation of the adatoms. As mentioned above, DFT calculations have revealed that the Au adatoms are relaxed by about 0.4 Å towards the substrate when switched to the negative state [17]. Because the $\Delta f(d)$ curves shown in Fig. 4.3b are monotonically increasing in the investigated distance range, this topographic effect alone would lead to a decrease of $|\Delta f|$ above Au^-. However, we observed the opposite effect. We can therefore attribute the stronger attractive force measured above Au^- to electrostatic interactions between the tip and the charged adatom that overcompensate the topographic effect. The physical origin of this electrostatic interaction will be elucidated further at the end of this chapter, when we discuss our observations in terms of a simple electrostatic model.

4.3 Influence of the charge state on the LCPD

In this paragraph, we investigate the effect of the charge state of adatoms on the local contact potential difference (LCPD) between the AFM tip and the sample. In addition to Au^0 and Au^-, Ag adatoms were investigated, for which also the positive charge state Ag^+ is stable on NaCl(2ML)/Cu(111), as known from previous a STM investigation [94]. We determined the LCPD from measurements of the frequency shift as a function of the voltage applied to the sample. The maximum of the parabola fitted to the $\Delta f(V)$ curve yielded the LCPD value V^* as well as the frequency shift at compensated LCPD Δf^*.

In Fig. 4.4a, $\Delta f(V)$ curves measured above Au^0 and above Au^- are shown. Without moving the tip, $\Delta f(V)$ was first measured above Au^-, a voltage pulse of $V = -1$ V was applied to switch the adatom and $\Delta f(V)$ was measured again above Au^0. To confirm the switching of the adatom

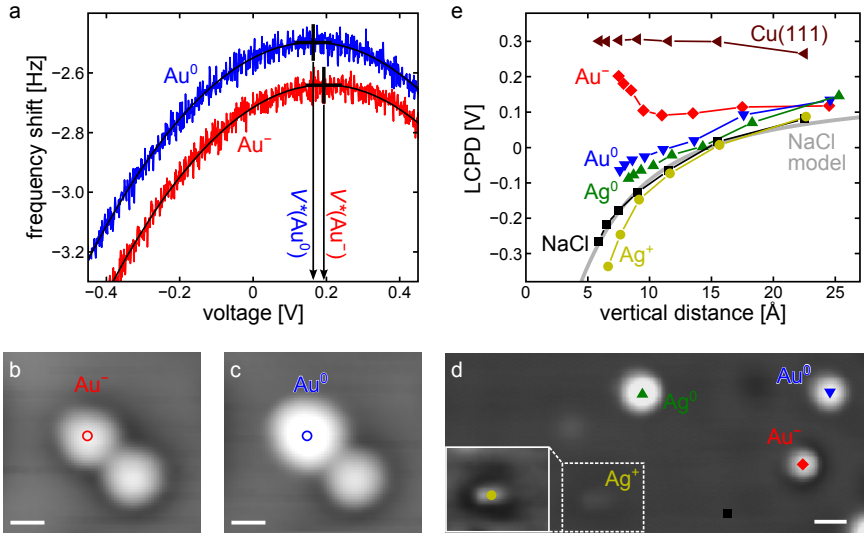

Fig. 4.4 Influence of the charge state on the LCPD. **a**, $\Delta f(V)$ spectra measured above a Au atom before and after charge switching ($d = 5.8\,\text{Å}$, $A = 0.6\,\text{Å}$). Solid black lines show parabolic fits to the measured data and the resulting LCPD values V^* are indicated by arrows. **b**,**c**, Constant-current STM images ($I = 7.4\,\text{pA}$, $V = -50\,\text{mV}$) before (**b**) and after (**c**) the LCPD measurement. **d**, Constant-current STM image of different adatoms on NaCl(2ML)/Cu(111) ($I = 3\,\text{pA}$, $V = 0.2\,\text{V}$). The inset shows the Ag^+ adatom with fivefold increased contrast. **e**, LCPD as a function of tip–sample distance above differently charged adatoms, above NaCl(2ML)/Cu(111) (positions indicated in **d**), and above the bare Cu(111) substrate. The LCPD values were extracted from Δf parabolas recorded at different heights ($A = 0.3\,\text{Å}$). The gray curve shows the LCPD above NaCl calculated with the simple plate-capacitor model described in the text. Scale bars: 5 Å in **b**,**c** and 10 Å in **d**.

and to verify that the switched adatom has maintained its lateral position, STM images were taken before and after the measurement (Fig. 4.4b,c). We observe that the switching of the charge state leads to a shifting of the frequency shift parabola both horizontally and vertically. For Au^-, V^* is shifted by $+27\,\text{mV}$ and Δf^* is shifted by $-0.11\,\text{Hz}$ with respect to Au^0. It should be noted that the absolute values of these shifts depended on the

exact tip condition and therefore varied in different measurements. The directions of the observed shifts, however, were found to be independent of the tip; we always observed a greater LCPD and a more negative Δf^* above the negatively charged adatom. Therefore, the differentiation of the different charge states was always possible by comparison. We will look into the origin of the shifting of the frequency shift parabola in further detail in the next paragraph. It is immediately clear, however, that the shift of the parabola to a higher voltage for the negatively charged adatom is reasonable from a physical point of view: the electric field generated by the Au^- and the induced positive image charge in the tip is compensated by applying a more positive voltage to the sample.

Next, we investigated the distance dependence of the LCPD shift over the different adatoms. Measurements on Ag adatoms were included to show that the neutral, positive, and negative charge state can all be distinguished from one another. An STM overview image of several adatoms on NaCl(2ML)/Cu(111) in different charge states is shown in Fig. 4.4d. We measured $\Delta f(V)$ for different tip–sample distances above the positions indicated in the image, and above the bare Cu(111) substrate (no tip change or manipulation of the adatoms was observed during the whole measurement). For all the $\Delta f(V)$ spectra, we determined the peak positions V^* from parabolic fits to the curves[2]. The resulting LCPD versus distance curves are shown in Fig. 4.4e. We first compare the LCPD measured above the NaCl bilayer and above the bare Cu(111) substrate. It is known that the NaCl film lowers the work function of the surface [88], and therefore, we expected a smaller LCPD above NaCl(2ML)/Cu(111) than above Cu(111). This is observed in Fig. 4.4e, but the effect also increases with decreasing distance d. Whereas the LCPD above Cu(111) is almost independent of d, it decreases above the NaCl film as the tip is approached towards the sample. We attribute this observation to an averaging effect that results from the finite size of the NaCl islands: for increasing tip–sample distance, the area of the sample that contributes to the measured value of the LCPD

2 In ref. [111], a nonparabolic Δf curve is predicted from theoretical simulations for a KPFM measurement above NaCl with a NaCl-terminated AFM tip. The authors attribute this deviation from the parabolic capacitive behavior to displacements of the ions at the tip-surface interface. However, no such deviations were observed in our experiments.

becomes larger and can exceed the size of the investigated NaCl island. When the tip is approached more closely, the relative influence of the surrounding Cu(111) surface on the measured LCPD is reduced, and the latter shifts to smaller values. This can be understood from the following very simple model: We assume that the tip can be modeled as two parallel plate capacitors describing the electrostatic tip–sample interaction with the NaCl area and the surrounding Cu surface, respectively. We further assume that the Cu capacitor is larger by a factor N, but also spaced further apart by a distance c (because the corresponding part of the tip is further away from the surface). Using Eq. 2.9 and Eq. 2.16, the following proportionality is then obtained for the frequency shift:

$$\Delta f \propto \frac{-N}{(d+c)^3}\left(V - V^*_{\mathrm{Cu}}\right)^2 - \frac{1}{d^3}\left(V - V^*_{\mathrm{NaCl}}\right)^2 . \tag{4.1}$$

The resulting LCPD curve for $V^*_{\mathrm{Cu}} = 0.3\,\mathrm{V}$ and $V^*_{\mathrm{NaCl}} = V^*_{\mathrm{Cu}} - 1\,\mathrm{V} = -0.7\,\mathrm{V}$ [95, 112], and $N = 7$ and $c = 6.5\,\text{Å}$ (shown in gray in Fig. 4.4e) reproduces well the measured distance dependence of the LCPD above NaCl. This shows that the simplistic plate-capacitor model can qualitatively explain the observed behavior of the LCPD above the NaCl islands.

Above the different adatoms, the observed values of the LCPD were very similar (within 0.1 V) for distances $d > 18\,\text{Å}$. When the tip was approached towards the sample, the LCPD measured above the different adatoms started to differ significantly, and for $d < 10\,\text{Å}$, the different charge states could be clearly distinguished. We observe a greater LCPD above Au^- than above Au^0 and a smaller LCPD above Ag^+ than above Ag^0. The absolute value of the LCPD difference obtained in different measurements again depended on the exact tip shape, but the direction of the LCPD shift was always directly related to the sign of the charge on the adatom (with respect to the neutral state, V^* would always shift to greater values above negative adatoms and to smaller values above positive adatoms). This shows that the distinction of neutral, positively, and negatively charged adatoms is possible by measuring the LCPD at close enough tip–sample distance. In particular, we were able to distinguish the charge states of Ag^+ and Ag^0, which would have been difficult to achieve by constant-height AFM imaging (as in Fig. 4.2), because of the large topographic difference between Ag^+ and Ag^0 [94].

4.4 A simple electrostatic model

We now discuss the results presented in the previous paragraphs in terms of the simple model illustrated in Fig. 4.5a: The investigated system constitutes a double-barrier tunnel junction, with one tunneling barrier given by the insulating film between the metal substrate and the adatom, and the other one given by the vacuum gap between the adatom and the AFM tip. Both tunneling junctions can be regarded as capacitances. In addition, the stray capacitance between the tip and the conducting substrate has to be considered. We denote by C_0, C_1 and C_2 the tip–substrate capacitance, the tip–adatom capacitance and the adatom–substrate capacitance, respectively. The free energy U of the system, which consists of the electrostatic energy minus the work done by the voltage source, is then given by [100, 102, 113]:

$$U = \frac{q^2}{2C_\Sigma} - \frac{C_1}{C_\Sigma} qV - \frac{C_1 C_2}{2C_\Sigma} V^2 - \frac{C_0}{2} V^2 \ , \tag{4.2}$$

where q is the charge on the adatom and $C_\Sigma = C_1 + C_2$. For the sake of simplicity, we refer to $V = 0$, when the contact potential difference between the tip and the substrate is compensated above the neutral adatom. The electrostatic force on the tip is found by differentiating U with respect to the vertical distance z (C_0 and C_1 are z-dependent, whereas C_2 is independent of z):

$$F_z = -\frac{\partial U}{\partial z} = \frac{\partial C_1}{\partial z} \left(\frac{q^2}{2C_\Sigma^2} + \frac{C_2}{C_\Sigma^2} qV + \frac{C_2^2}{2C_\Sigma^2} V^2 \right) + \frac{1}{2} \frac{\partial C_0}{\partial z} V^2 \tag{4.3a}$$

$$= \frac{1}{2C_\Sigma^2} \frac{\partial C_1}{\partial z} \left(q + C_2 V \right)^2 + \frac{1}{2} \frac{\partial C_0}{\partial z} V^2 \ . \tag{4.3b}$$

Differentiating once more with respect to z (compare Eq. 2.9), we find that the voltage-dependent electrostatic contribution to the frequency shift is given by a parabola of the form $\Delta f(V) = a(b + V)^2 + cV^2$, with certain parameters a, b, c.

To show that this simple model can indeed explain the shifting of the frequency shift parabola observed in Fig. 4.4a, the function $\Delta f(V)$ is plotted in Fig. 4.5b for the values $a = 1$, $c = -5$, and $b = -1, 0, +1$ (corresponding to negative, zero, and positive charge). In agreement with our measurements,

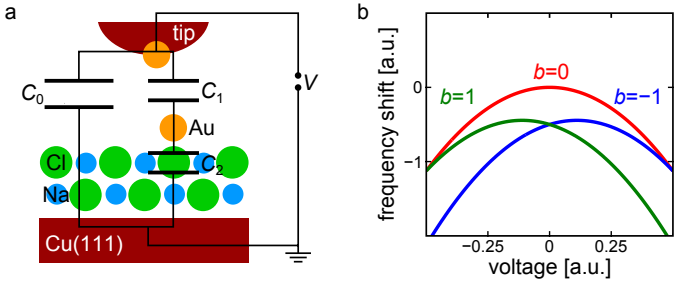

Fig. 4.5 Simple electrostatic model for the double-barrier tunnel junction. **a**, Schematic illustration of the tip and sample system and equivalent circuit of the electrostatic model. C_0, C_1, and C_2 denote the tip–substrate capacitance, the tip–adatom capacitance and the adatom–substrate capacitance, respectively. **b**, The function $\Delta f(V) = a(b+V)^2 + cV^2$ plotted for different values of b, corresponding to negative charge (blue), no charge (red), and positive charge (green) in the double-barrier tunnel junction. Nonvanishing values of b cause both a vertical and a lateral shift of the parabola, the directions of which are in agreement with our measurements.

we find that a negative (positive) charge in the double-barrier tunnel junction leads to a shift of the Δf parabola to lower frequencies and higher (lower) voltages. The considered model is strongly simplified, and we have completely neglected the (V-independent) contributions from other forces (like the van der Waals force) to the frequency shift. Therefore, we abstain from attempting a quantitative determination of the actual values of the parameters a, b, c from the measurement. Considering the simplicity of the model, however, it is pleasing to see that it can at least qualitatively explain the shift of the LCPD observed above the charged adatoms.

One last point should be mentioned concerning the origin of the difference between the forces above neutral and charged adatoms: The first term of the sum in Eq. 4.3a can be attributed to the electrostatic interaction between the charge on the adatom and the image charge induced in the AFM tip. In previous studies, it was argued that this term is negligible [100, 102], due to the experimental conditions used in these studies (large oscillation amplitudes, large tip–sample distances). In our case, however, this assumption is not justified and only this term can explain the different forces measured

above Au^0 and Au^- at zero voltage[3]. Therefore, we come to the conclusion that the shifting of the force and frequency shift parabolas observed for the different charge states of metal adatoms is mainly due to the electrostatic interaction between the charged atoms and the corresponding image charges induced in the tip.

3 One could argue that other voltage-independent force contributions like the van der Waals force could be responsible for the change in Δf at $V = 0$. However, as mentioned above, the change in Δf expected from the topographic difference of the differently charged gold adatoms is in the opposite direction (a stronger attractive force above Au^0 would be expected).

CHAPTER 5

Atomic-resolution AFM imaging of single molecules

Resolving single atoms has always been the ultimate goal of surface microscopy. With STM, atomic-scale features on surfaces can be imaged, but resolving the individual atoms within an adsorbed molecule remains a great challenge. This is because the tunneling current is primarily sensitive to the electron density of states at the Fermi level, which usually extends over the entire molecule. Consequently, STM images of single molecules reflect only roughly the contour of the molecule or – if the right bias voltage is applied in the case of molecules on thin insulating films – the structure of the frontier orbitals of the molecule [25, 114]. If the chemical structure of a molecule is to be imaged, one needs to be sensitive to energetically lower-lying electron states, which are more localized at the positions of the atoms and bonds within the molecule. Here we show that imaging the chemical structure of individual organic molecules is possible with noncontact AFM if the microscope tip is functionalized with suitable atomically well-defined terminations, such as a single CO molecule.

In the first part of this chapter, we present AFM imaging of single pentacene molecules with different functionalized tips, demonstrating the strong influence of the tip termination on the image contrast. Next, we present imaging of other molecules with the CO tip functionalization, which we found to be most stable and give the highest resolution in AFM imaging. To further elucidate the exact imaging mechanism and study the influence of the imaged molecule's topography and chemical composition on the image

contrast, apart from mere AFM imaging we also carried out complete 3D force map measurements, which are described in the next part of this chapter. Finally, by comparison with density functional theory (DFT) calculations, we identify Pauli repulsion as the source of the atomic resolution in our AFM images, whereas the attractive van der Waals (vdW) and electrostatic forces contribute only a diffuse background.

5.1 AFM imaging of pentacene

Noncontact-AFM in UHV has seen tremendous progress in recent years. Just to name a few prominent examples: chemical identification of single surface atoms [31], measurements of the exchange force with atomic resolution [36, 115, 116], and both lateral and vertical manipulation of single atoms [32, 33] have been achieved, and the force needed to move a single atom on a surface was measured [35]. As far as AFM studies of single molecules are concerned, atomic resolution was achieved on single-walled carbon nanotubes [30, 117], and the switching energy of a single-molecule conformational switch was determined [34]. Despite these impressive results, the complete chemical structure of an individual molecule has not been imaged with atomic resolution until now. There are two reasons that make AFM investigations of adsorbed molecules especially challenging: the strong influence of the exact atomic composition and geometry of the tip and the relatively low stability of the system, which can result in unwanted lateral or vertical manipulation of the imaged molecule. We have found that both problems can be overcome by preparing a well-defined, chemically inert tip by picking up single atoms or molecules from the sample surface using the tip preparation techniques described in Chapter 3. Such well-defined tip modifications are known to yield enhanced resolution in STM imaging [10, 25, 91, 93, 118], but have rarely been used in AFM investigations, where the exact tip structure is usually unknown and can only be guessed from comparison with calculations [31, 33, 119, 120]. Here we show that the combination of established STM tip preparation techniques with AFM enables imaging of single molecules with unprecedented resolution [121].

To benchmark the AFM resolution on single molecules, we imaged pentacene, a polycylic hydrocarbon consisting of five fused benzene rings (Fig. 5.1a), on Cu(111) and on NaCl(2ML)/Cu(111). This molecule has

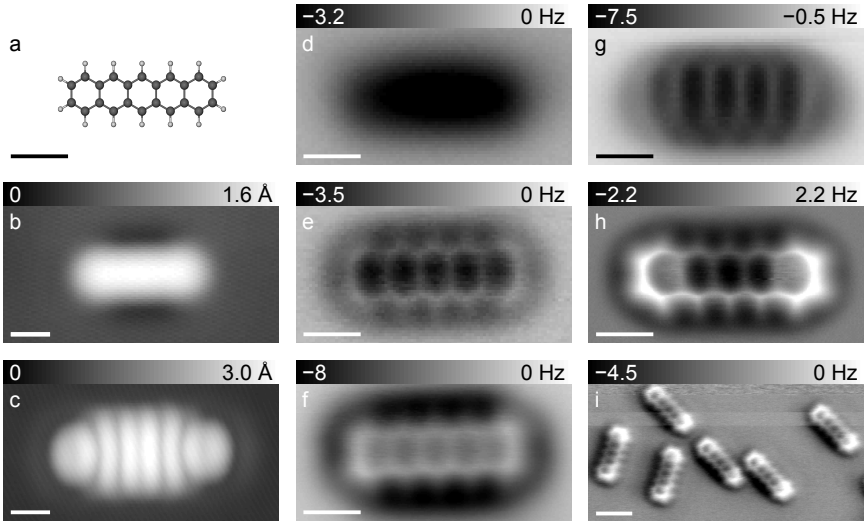

Fig. 5.1 STM and AFM imaging of pentacene with different functionalized tips. **a**, Ball-and-stick model of pentacene. **b**,**c**, In-gap STM topography (**b**, $I = 1.1\,\text{pA}$, $V = -0.8\,\text{V}$) and STM topography of the LUMO resonance (**c**, $I = 1.3\,\text{pA}$, $V = 1.3\,\text{V}$) of pentacene on NaCl(2ML)/Cu(111), measured with a CO tip. **d-g**, Constant-height AFM images of pentacene on NaCl(2ML)/Cu(111), measured with a metal tip (**d**, oscillation amplitude $A = 0.6\,\text{Å}$, vertical tip distance $z = -0.8\,\text{Å}$), with a CO tip (**e**, $A = 0.7\,\text{Å}$, $z = 1.3\,\text{Å}$), with a Cl tip (**f**, $A = 0.5\,\text{Å}$, $z = 1.0\,\text{Å}$), and with a pentacene tip (**g**, $A = 0.9\,\text{Å}$, $z = 0.5\,\text{Å}$). **h**, Constant-height AFM image of pentacene on Cu(111), measured with a CO tip ($A = 0.2\,\text{Å}$, $z = -2.1\,\text{Å}$). **i** Constant-height AFM image of several pentacene molecules on Cu(111), measured with a CO tip ($A = 0.8\,\text{Å}$, $z = -2.5\,\text{Å}$). All z values are given with respect to an STM set point of $I = 2\,\text{pA}$, $V = 0.2\,\text{V}$ over the substrate. Scale bars: 5 Å in **a**-**h** and 10 Å in **i**.

been studied before with high-resolution STM [13, 25, 93, 122], and an in-gap STM topographic image and an STM image of the LUMO resonance are shown in Fig. 5.1b,c. Both images were recorded with a CO-terminated tip, which is known to enhance the contrast in STM imaging [10, 91, 114], but the chemical structure of the molecule is not reflected in these STM images. As discussed above, this is due to the fact that the molecular frontier orbitals extend over the entire molecule, rather than being localized

at the atomic positions.

To achieve atomic resolution with AFM, it is necessary to operate in a distance region, where short-range chemical forces give significant contributions to the image contrast. The sensitivity to these short-range forces is enhanced by using small (< 1 Å) oscillation amplitudes [45]. Furthermore, imaging in constant-height mode allows stable operation even if the frequency shift $\Delta f(z)$ is a nonmonotonic function of distance. In Fig. 5.1d-g, constant-height AFM images of a pentacene molecule on NaCl(2ML)/Cu(111) are shown, recorded with a metal tip, a CO tip, a Cl tip, and a pentacene tip, respectively. For each tip, the distance z was minimized such that decreasing z further by a few 0.1 Å would result in unstable imaging conditions, with the molecule being laterally displaced or picked up by the tip. Comparing the different tips, we see that their atomic termination is crucial for the contrast in AFM molecular imaging. With metal-terminated tips, it was not possible to image at distances close enough to observe short-range repulsive contributions to the frequency shift, and no submolecular resolution could be observed (Fig. 5.1d). This changed dramatically, when we used a tip terminated with a single CO molecule. In this case, below a certain tip–sample distance bright features started to appear in the constant-height Δf image, and the structure of the five hexagonal carbon rings of the pentacene molecule could be observed (Fig 5.1e). The Cl tip termination yielded a similar contrast as the CO tip, with a slightly lower resolution but also less distortion in the direction perpendicular to the long axis of the molecule (Fig. 5.1f). The pentacene tip termination, which has previously been used to enhance the resolution in STM orbital imaging [25], gave a completely different image, which could not be directly related to the molecular structure (Fig. 5.1g). This emphasizes the strong influence of the exact tip termination on the contrast in AFM imaging. In general, the CO tip termination was found to have the most favorable properties for molecular structure imaging with AFM: highest resolution, easy tip preparation, and high stability of the tip (it was often possible to measure for several days with no observable change in the tip configuration). All high-resolution AFM molecule images presented in the following were recorded with CO tips.

To show that the insulating film is not necessary for molecular structure imaging with AFM (unlike for orbital imaging with STM), in Fig. 5.1h, a high-resolution constant-height AFM image of pentacene on Cu(111) is

shown. It is interesting to note that not only the positions of the C atoms in the molecule and the bonds between them are resolved, but also the C–H bonds, which indicate the positions of the H atoms at the periphery of the molecule. We attribute the enhanced brightness at the left and right ends of the molecule to a nonplanar adsorption geometry on Cu(111), with the ends of the molecule being slightly elevated [123, 124]. In Fig. 5.1i, a CO-tip AFM image of several pentacene molecules with two different adsorption orientations on Cu(111) is shown. For all molecules, we again observe the characteristic bright ends and an asymmetric appearance (dark silhouette only on the left side of the molecules), which indicates that in this case the CO molecule was adsorbed slightly asymmetrically at the tip apex.

5.2 AFM imaging of other molecules

To demonstrate the general applicability of our method and to elucidate the influence of the adsorption geometry and chemical composition on the AFM contrast, we imaged several different molecules both on bilayer NaCl and on the bare Cu(111) substrate. All Δf images shown in Fig. 5.2 were measured in constant-height mode with CO-functionalized tips, using oscillation amplitudes $\lesssim 0.5\,\text{Å}$. The molecule hexabenzo-coronene (HBC) is a planar polycyclic aromatic hydrocarbon consisting of 13 fused C_6 rings (Fig. 5.2b). It is particularly interesting because it can be considered as a subsection of graphene, which makes it suitable as graphene precursor and as a model system for graphene hydrogenation [125]. HBC was found to be only weakly bound on NaCl(2ML)/Cu(111), making high-resolution imaging very challenging. On Cu(111), on the other hand, the molecular structure could be clearly resolved (Fig. 5.2a), with a contrast similar to that demonstrated for pentacene. The enhanced brightness observed at the periphery of the molecule could be due to a nonplanar adsorption geometry or to an electronic effect where the delocalized electrons in the π-conjugated system have a higher density at the boundary of the molecule[1]. As shown in Fig. 5.2c,d,

1 This would be reminiscent for example of the solutions of the quantum mechanical harmonic oscillator: the wave functions for higher values of the energy quantum number mimic the classical situation, where there is an enhanced probability of finding the particle close to the turning points of the oscillatory motion [126].

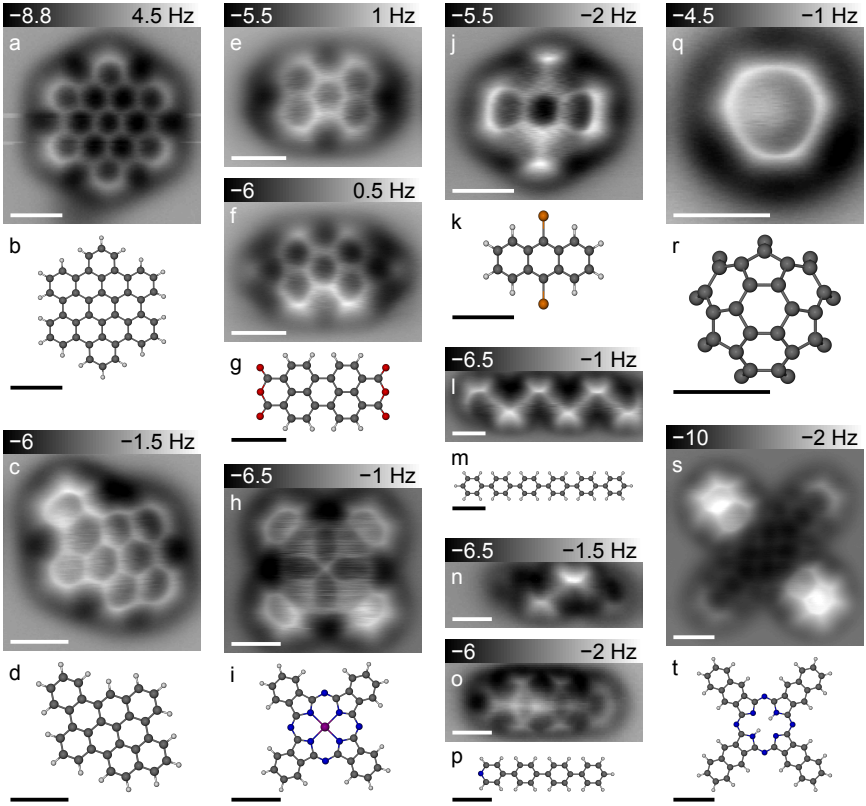

Fig. 5.2 Constant-height AFM images of different molecules measured with CO-functionalized tips, and corresponding ball-and-stick models. **a**,**b**, Hexabenzocoronene on Cu(111). **c**,**d**, Dibenzo-naphtho-perylene on NaCl(2ML)/Cu(111). **e-g**, Perylene-tetracarboxylic-dianhydride on NaCl(2ML)/Cu(111) (**e**) and on Cu(111) (**f**). **h**,**i**, Co-phthalocyanine on NaCl(2ML)/Cu(111). **j**,**k**, Dibromo-anthracene on NaCl(2ML)/Cu(111). **l**,**m**, Sexiphenyl on NaCl(2ML)/Cu(111). **n-p**, Terphenyl-pyridine on NaCl(2ML)/Cu(111) (**n**) and on Cu(111) (**o**). **q**,**r**, Buckminsterfullerene on Cu(111). **s**,**t**, Naphthalocyanine on Cu(111). All scale bars: 5 Å. Carbon, hydrogen, oxygen, nitrogen, cobalt, and bromine atoms are colored in gray, white, red, blue, purple, and orange, respectively.

similar results were obtained for the less symmetric polycylic aromatic hydrocarbon dibenzo-naphtho-perylene on NaCl(2ML)/Cu(111). We also studied molecules containing heteroatoms (atoms other than hydrogen and carbon), such as perylene-tetracarboxylic-dianhydride (PTCDA), which has two end-groups that contain three oxygen atoms each (Fig. 5.2g). This molecule has been studied extensively in surface science due to its applications as an organic semiconductor. We were able to image it both on the NaCl islands (Fig. 5.2e) and on the bare Cu(111) surface (Fig. 5.2f). Depending on the substrate, the oxygen-containing end-groups are not resolved at all [on NaCl(2ML)/Cu(111)], or only one of the oxygen atoms is visible [on Cu(111)]. This peculiar behavior could be due to a topographic or a chemical effect, or a combination of both. We will study PTCDA in further detail in the context of the Au-PTCDA switch investigated in the next chapter.

The next molecule we studied was Co-phthalocyanine, a coordination complex with an alternating C-N ring structure around the central Co atom (Fig. 5.2i). On NaCl(2ML)/Cu(111), the C_6 rings at the periphery of the molecule and the C_4N rings are resolved (albeit with strongly distorted appearance), as well as the Co atom in the center (Fig. 5.2h). The molecule dibromo-anthracene (DBA, Fig. 5.2j,k) has two Br atoms, which appear very bright in the AFM images and with a shape elongated in the direction perpendicular to the C-Br bonds, a peculiar feature which we also observed for other molecules containing Br atoms. Next, we studied two chains of phenyl rings, sexiphenyl (Fig. 5.2l,m) and terphenyl-pyridine (TPP, Fig. 5.2n-p), the latter with a pyridine ring at one end. On NaCl(2ML)/Cu(111), we observe a characteristic zigzag structure in the AFM images (Fig. 5.2l,n), which we attribute to an adsorption geometry where adjacent phenyl rings are twisted against each other and have their hydrogen atoms tilted upwards at opposite sides of the molecule. This leads to the alternating bright features in the AFM images. For TPP on Cu(111), on the other hand, we observe a distinctly different structure in the AFM image (Fig. 5.2o), with the individual phenyl rings appearing more symmetric, indicating a flat adsorption geometry. In addition, one end of the TPP molecule appears darker than the other, which could be due to the pyridine end interacting stronger with the substrate and bending downwards. A molecule with an intrinsic nonplanar structure is the Buckminsterfullerene C_{60} (Fig. 5.2r, only the upper dome of the molecule is shown), which could only be stably

imaged on Cu(111). From the constant-height AFM image (Fig. 5.2q), we are able to identify the adsorption orientation of the C_{60} as facing upwards with a C_6 ring, in agreement with a previous STM and DFT study [127], but the other carbon rings of the molecule are not resolved. Finally, we also investigated naphthalocyanine (Fig. 5.2t), which can be operated as a single-molecule hydrogen-tautomerization switch when it is adsorbed on thin insulating films [27]. Naphthalocyanine on NaCl(2ML)/Cu(111) will be studied in detail in Chapter 8, in the context of KPFM imaging with submolecular resolution. Here we show an atomically resolved AFM image of naphthalocyanine on Cu(111), in which a pronounced asymmetry between the two molecular lobes along one direction and the two lobes along the perpendicular direction is observed (Fig. 5.2s). This asymmetry can be attributed to a saddle-like adsorption geometry, which has been frequently observed for phthalocyanines on flat metal surfaces [128–130].

In summary, we have found our approach of molecular structure imaging with AFM using CO-functionalized tips to be applicable to a wide range of organic molecules. In general, aromatic carbon rings lying flat on the surface were easy to image, whereas nonplanar adsorption geometries and heteroatoms led to a wide variety of structures in the AFM images, which can be difficult to interpret without additional information or assumptions. To gain a better understanding of the detailed contrast mechanism and to further elucidate the influence of molecular geometry and chemical composition on the image contrast, in the next paragraph, we move from the simple constant-height AFM imaging to a more sophisticated approach that gives access to the complete short-range force field above a molecule.

5.3 Measuring the 3D force field above a molecule

Apart from its mere imaging capabilities, noncontact AFM offers the possibility of $\Delta f(z)$ spectroscopy to quantify the short-range forces at specific atomic sites [31, 34, 131, 132]. This can be extended to systematic recording of dense 2D $[\Delta f(x, z)]$ or 3D $[\Delta f(x, y, z)]$ data sets of the frequency shift, which can subsequently be converted into 2D or 3D fields of the vertical and lateral forces [30, 35, 133–138]. There are in principle two different methods to measure such force maps: In the first method, which we used in the preceding chapter to quantify the forces above the differently

charged adatoms, the tip is scanned horizontally at constant height or on a topography $z(x, y)$ of constant frequency shift, and a line $\Delta f(x)$ or an image $\Delta f(x, y)$ is recorded. The data recorded for different heights are then merged into a complete $\Delta f(x, z)$ or $\Delta f(x, y, z)$ data set [35, 134, 135, 137]. In the second method, individual $\Delta f(z)$ spectra are consecutively recorded along a line or on a lateral grid and then merged to obtain the complete data set [30, 133, 136, 138].

To understand the distance dependence of the contrast in our atomically resolved molecular images and to be able to extract the forces acting on the tip, we captured complete $\Delta f(x, y, z)$ data sets above pentacene on NaCl(2ML)/Cu(111), using the second method of consecutive recording of $\Delta f(z)$ spectra. The following routine was developed for these measurements: First, a constant-current STM image of the molecule was recorded. This served as reference image for lateral drift compensation during the measurement. Then, the current feedback was switched off, and the tip was moved to sequentially record the $\Delta f(z)$ spectra for the force maps. About every 20 minutes (corresponding to ~ 100 spectra recorded), the tip was moved back to the starting point of the reference image, the current feedback was switched on, and another STM image was recorded. By cross-correlating this image with the reference image, the lateral drift could be determined and compensated before switching the feedback off again and continuing $\Delta f(z)$ data acquisition. The vertical drift was compensated after each spectrum, by moving the tip to the starting point (over the substrate) and switching on and off the current feedback. This measurement procedure ensured minimal drift during the long force map measurements, which lasted up to 40 h (limited by the hold time of the liquid nitrogen tank of the cryostat).

The results of a 3D force map measurement with a CO-terminated tip are shown in Fig. 5.3a,b. The frequency shift was measured in a box of $25\,\text{Å} \times 12.5\,\text{Å} \times 13\,\text{Å}$ above a pentacene molecule by recording 80×40 individual $\Delta f(z)$ spectra. The vertical force F_z was extracted using the method of Sader and Jarvis [74] (Eq. 2.14). Fig. 5.3a shows constant-height Δf maps extracted from the complete data set at different heights, and Fig. 5.3b shows the corresponding F_z maps. For distances greater than $z = 4.2\,\text{Å}$, we measured only relatively small attractive long-range forces ($F_z < 20\,\text{pN}$), and the molecule was imaged as a featureless depression. With decreasing tip height, $\Delta f(z)$ decreased before reaching a minimum

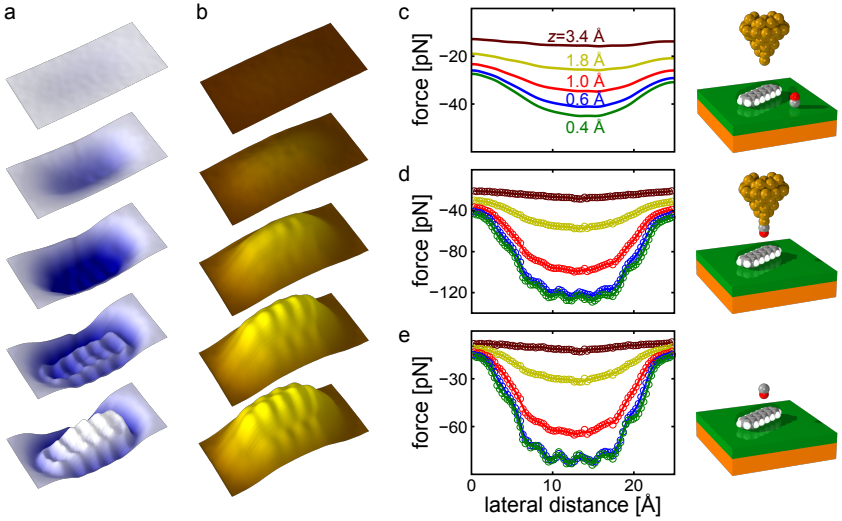

Fig. 5.3 Force map measurements of pentacene on NaCl(2ML)/Cu(111). **a**,**b**, Maps of measured frequency shift (**a**) and extracted vertical force (**b**) at different tip heights ($z = 4.2$, 2.6, 1.8, 1.4, and 1.2 Å, decreasing from top to bottom). The data shown are part of a complete 3D force field captured with a CO tip in a box of 25 Å × 12.5 Å × 13 Å above the pentacene molecule. The color scales range from −3 Hz (blue) to 0 Hz (white) and from −120 pN (yellow) to 0 pN (brown), respectively. **c**-**e**, Line scans of the vertical force extracted at different heights from complete 3D force maps measured with a metal tip (**c**) and with a CO tip (**d**). The difference between the two tips (**e**) gives the contribution of the CO alone, as indicated in the schematic representations of the tip and sample system to the right of the graphs. All tip heights are given with respect to the height determined by the STM set point ($I = 2$ pA, $V = 0.2$ V) with the CO-terminated tip above the substrate.

at about $z = 1.8$ Å above the center of the molecule. Near this minimum, we started observing lateral corrugation on the atomic scale, and when z was decreased further, Δf increased again and finally became even positive over some parts of the molecule at $z = 1.2$Å. In general, the contrast and lateral resolution in Δf increased with decreasing tip height, and the highest resolution was achieved at the height at which Δf crossed zero. Decreasing the tip height even further would result in instabilities and eventually in

picking up the molecule with the tip. In the force maps (Fig. 5.3b), the contrast was also found to increase with decreasing z. However, due to the integration over z, the atomic contrast in F_z is much lower than in Δf at the same height. At the closest distance ($z = 1.2\,\text{Å}$), we measured an attractive force of 110 pN above the central carbon ring. The forces above the positions of the C atoms were found to be significantly smaller, between 60 and 90 pN. These values are comparable to the short-range forces recently measured with a silicon tip above the hollow sites and carbon sites of a single-walled carbon nanotube [30].

The interaction between the CO-terminated tip and the sample contains contributions both from the CO at the tip apex and from the metal part of the tip behind the CO. To separate these contributions, in another measurement we first measured a 3D force map with a metallic tip, then picked up a single CO molecule from the surface to create a CO tip, and finally measured another force map of the same pentacene molecule. In Fig. 5.3c,d, force linescans extracted from these 3D force maps are shown. In the graphs, lines of the same color correspond to the same absolute tip height (in particular the fact that the height corresponding to the STM set point changed when picking up the CO has been taken into account). Because no other tip change except the intentional pickup of the CO was observed during the measurement, we can subtract the two force maps to estimate the contribution from the CO molecule (Fig. 5.3e). We observe that the contribution from the CO predominates in the relevant region, whereas the metal part of the tip contributes only about 30 % to the attractive forces and gives no corrugation on the atomic scale. These results facilitate the comparison of our measurements with DFT calculations, where the unknown structure of the metal part of the tip is difficult to take into account. Before presenting such DFT calculations in the last part of this chapter, we describe a refined force mapping method that enables measurements of the complete short-range force field even for nonplanar molecules.

5.3.1 Smart tip approach

We have seen that atomic resolution of single molecules is obtained only within a narrow distance region around the minimum of the $\Delta f(z)$ curve, where the frequency shift is a nonmonotonic function of the tip–sample distance. This prevents imaging with constant-frequency-shift feedback

and restricts us to the constant-height mode[2]. If the tip–sample distance for a constant-height AFM image or the distance of closest tip approach for a force map measurement is chosen to be sufficiently large (such that no unwanted manipulations occur), then the substrate is not atomically resolved. Furthermore, in the case of nonplanar molecules, atomic resolution is only obtained on the part of the molecule closest to the tip [30, 139]. To overcome these limitations, we have developed a force mapping method that incorporates a variable distance of tip approach, which is determined in real time for each $\Delta f(z)$ spectrum [140]. To that end, we define two threshold frequencies, typically $\Delta f_1 = -2\,\mathrm{Hz}$ and $\Delta f_2 = 0\,\mathrm{Hz}$. During the approach of the tip, the condition $\Delta f(z) < \Delta f_1$ has to be fulfilled to activate the actual abort criterion. The approach then continues, until the second condition $\Delta f(z) > \Delta f_2$ is fulfilled, and the tip is immediately stopped at that position and not approached any further. In this way, we are able to approach the tip until we have passed through the minimum of $\Delta f(z)$ and reached the repulsive branch of the curve, where $\partial(\Delta f)/\partial z < 0$. In addition, we set an absolute closest tip-approach distance (in case the aforementioned abort criterion were to fail), which we define as the $z = 0$ origin in Fig. 5.4a,b. Using this enhanced protocol, we were able to record complete 2D and 3D force maps even of nonplanar molecules. Both the imaged molecules and the CO-terminated tip remained unaltered during these measurements, which lasted up to 40 h.

To test our modified method, we first measured a 2D force map of pentacene on NaCl(2ML)/Cu(111). We were now able to reach the repulsive branch of the $\Delta f(z)$ curve not only on top of the molecule, but also over the substrate. In Fig. 5.4a, $\Delta f(z)$ spectra are shown for three selected positions: above the pentacene molecule, above the substrate, and above the edge of the molecule. The curves clearly differ from one another: On the molecule (squares), the minimum in $\Delta f(z)$, which indicates the onset of repulsive force contributions, was found at $z = 4.8\,\text{Å}$. On the substrate (circles), the tip had to be approached much closer before the minimum

2 In principle, it is also possible to record AFM images with STM constant-current feedback. As we will see in the next chapter, this can be helpful in certain cases, for example to determine the lateral adsorption position of a molecule. In general, however, such images are difficult to interpret, because of the intermixing of the force and the current signal.

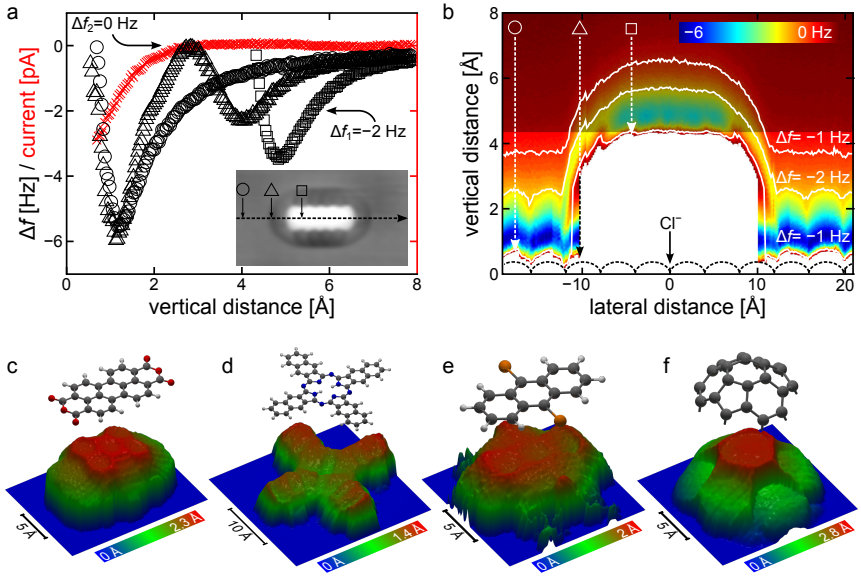

Fig. 5.4 Force maps recorded with the smart tip approach. **a**, $\Delta f(z)$ spectra at different sites: above pentacene (squares), above the NaCl(2ML)/Cu(111) substrate (circles), and above the edge of the molecule (triangles), as indicated in the STM image shown as inset. Red crosses: simultaneously recorded current signal above the substrate ($V = 10\,\mathrm{mV}$, $A = 0.35\,\text{Å}$). **b**, 2D force mapping: $\Delta f(z)$ spectra recorded on a line along the pentacene molecule. The color scale reflects the value of Δf, and constant-Δf topographies are overlaid (white solid lines). The dotted line at the bottom is drawn as a guide to the eye to indicate the Cl^- sites of the substrate. **c-f**, Constant-Δf topographies of PTCDA (**c**), naphthalocyanine (**d**), DBA (**e**), and C_{60} (**f**). The topographies were extracted from 3D force maps for $\Delta f = 0\,\mathrm{Hz}$ on the repulsive branch of the $\Delta f(z)$ curve. Ball-and-stick models of the molecules are overlaid.

was reached at $z = 1.2\,\text{Å}$. The curve recorded at the edge of the molecule (triangles) exhibits a peculiar behavior. It has two minima, indicating that the tip 'feels' first the molecule and then the substrate as it is approached towards the sample at close lateral distance to the molecule. The complete 2D Δf map from which the curves in Fig. 5.4a have been taken, is shown in Fig. 5.4b. A set of 250 individual $\Delta f(z)$ spectra was measured on a line

along the long axis of the pentacene molecule (the reference STM image used for lateral drift correction is shown in the inset of Fig. 5.4a). In the $\Delta f(x, z)$ map in Fig. 5.4b, we can clearly identify the pentacene molecule at an apparent height of $\sim$ 3–4 Å above the NaCl substrate. The positions of the five carbon rings are visible, and lines of constant Δf were extracted for frequencies on both the attractive and the repulsive branch of the $\Delta f(z)$ curve. In the Δf map, we also observe atomic resolution of the substrate, and by comparison with atomically resolved STM images we can assign the depressions in the constant-Δf topographies to the positions of the Cl^- ions. The shaded area in Fig. 5.4b indicates the portion of the data that would have been accessible with the conventional method with fixed tip-approach distance. As described above, in the border region of the molecule (at lateral distances around $x = \pm 10$ Å), we measured curves that differ from the generic $\Delta f(z)$ curve with one minimum. In this region, instabilities during the measurement were also found to be most likely to occur. This can be understood from the fact that with our approach procedure, we are able to limit the vertical force, but not the lateral force, which our AFM sensor is insensitive to. However, lateral forces may become significant when the tip is approached to the sample in the immediate neighborhood of an adsorbed molecule[3].

To demonstrate that our method can also be used to measure complete 3D force maps, constant-Δf topographies of different molecules are shown in Fig. 5.4c-f. These topographies were all extracted for $\Delta f = 0$ Hz on the repulsive branch, from 3D Δf maps each constructed from $\sim$ 5000 individual $\Delta f(z)$ spectra. The substrate was not atomically resolved in these measurements because we have chosen an absolute closest tip-approach distance further away from the substrate, to reduce the risk of instabilities when the tip is approached at the edges of the molecule. For PTCDA on NaCl(2ML)/Cu(111) (Fig. 5.4c), the perylene core is atomically resolved in the constant-Δf topography, whereas the anhydride end groups appear only as featureless elevated regions. The atomic corrugation is only on the order of 0.1 Å, because of the Δf set point on the steep repulsive branch of the $\Delta f(z)$ curve. The ends of the perylene core appear to be bent down towards the

3 A lateral force acting on the CO at the tip apex can also cause a bending of the CO [141], which could explain the often distorted appearance of the peripheral C_6 rings in the AFM images recorded with CO tips (see e.g. Fig. 5.1h) [142].

substrate, indicating a slightly nonplanar topography, which is in agreement with DFT calculations carried out for the Au-PTCDA complex discussed in the next chapter [143]. For naphthalocyanine on NaCl(2ML)/Cu(111) (Fig. 5.4d), the individual carbon rings of the four molecular lobes are resolved, and also the atomic structure of the porphine core is reflected in the topography (see also Chapter 8 and Appendix B). For DBA on NaCl(2ML)/Cu(111) (Fig. 5.4e), the three carbon rings of the anthracene core appear completely flat and the Br atoms are also clearly resolved in the topography. For the strongly nonplanar C_{60} fullerene on Cu(111) (Fig. 5.4f), the C_6 ring facing upward is atomically resolved with strongly distorted shape, which is due to the different bond orders of the bonds fusing two hexagons and those fusing a hexagon and a pentagon [142]. Furthermore, the adjacent hexagons and pentagons can be clearly distinguished in the constant-Δf topography, due to a stronger attractive interaction measured above the hexagons.

5.4 Comparison with DFT calculations

In the last part of this chapter, we return to our standard system – pentacene on NaCl(2ML)/Cu(111) imaged with a CO tip – and compare our experimental results to DFT simulations carried out by Nikolaj Moll of the Computational Sciences department at IBM Research – Zurich [121, 144]. For these calculations, the highly optimized plane-wave code CPMD [145] was used, with the Perdew-Burke-Ernzerhof exchange-correlation functional [146] and ab initio norm-conserving pseudopotentials [147] created according to the scheme of Trouiller and Martins [148]. Van der Waals forces are nonlocal correlations that are beyond the scope of the local density approximation and generalized gradient approximation commonly used in DFT. To overcome this limitation, we added a contribution proportional to R^{-6} to the dispersion energy (where R is the distance to the center of the atom), following the semiempirical approach described by Grimme [149]. When expanding the wave functions into plane waves, a high energy cutoff of about 2.7 keV had to be used to achieve a sufficiently high precision for the convergence of the interaction energies. In our calculations, only the pentacene and the CO are included, neglecting both the substrate and the metal part of the tip. It was assumed that the CO is oriented

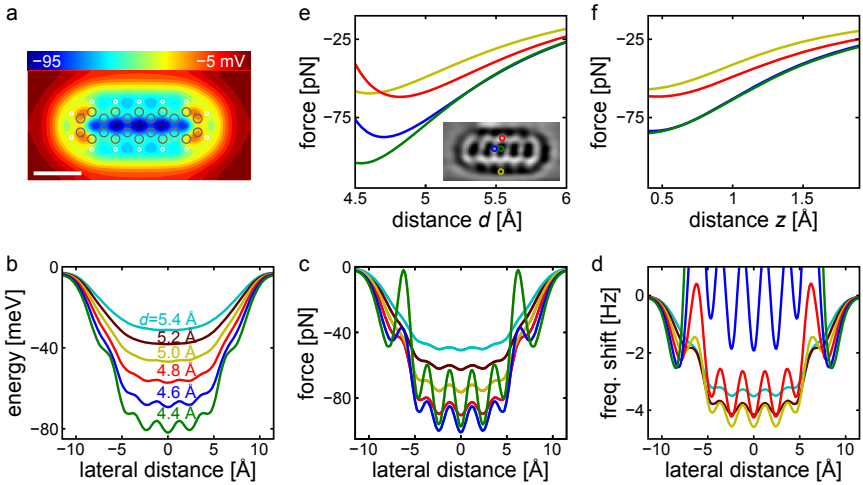

Fig. 5.5 Comparison of experimental AFM results with DFT simulations. **a**, Calculated map of the CO–pentacene interaction energy for an intermolecular distance (CO carbon atom to the pentacene molecular plane) of $d = 4.5$ Å. **b-d**, Calculated line profiles of the energy (**b**), force (**c**), and frequency shift (**d**) above the long molecular axis for different distances (indicated in **b**). **e**,**f**, Comparison of calculated (**e**) and measured (**f**) force curves above different molecular sites: central hollow site (green), C–C bond of the central ring on the long molecular axis (blue), C atom of the central ring on the short axis (red), and H atom on the short axis (yellow). The experimental curves were extracted from a complete 3D force map where the force contribution from the metal part of the tip has been subtracted. The inset in **e** shows a filtered constant-height Δf map extracted from the experimental data.

perpendicularly to the plane of the pentacene molecule, with the O atom pointing towards the pentacene. The CO was 'scanned' over the pentacene, and for each position, the interaction energy was calculated. The atomic positions were held fixed at the equilibrium positions calculated separately for each molecule, because for the investigated heights, relaxing the atoms did not change the results.

In Fig. 5.5a, a map of the interaction energy E is shown, calculated for a CO–pentacene distance of $d = 4.5$ Å (distance of the CO carbon atom to the

pentacene molecular plane). At this distance, atomic-scale variations can be observed in the interaction energy, with stronger attractive interaction above the centers of the five hexagonal carbon rings, and less attractive interaction above the positions of bonds and atoms. The ends of the (flat) molecule appear enhanced in brightness, indicating that such features can be due to electronic rather than structural properties of the molecule. In Fig. 5.5b-d, calculated line profiles of the interaction energy, vertical force, and frequency shift along the long molecular axis are shown for different CO–pentacene distances. To obtain the vertical force $F_z(d)$ and the frequency shift $\Delta f(d)$, the distance dependence of the interaction energy was fitted by a potential of the form $E_{\mathrm{vdW}}(d) = (a/d)^b - (u/d)^v$, with fitting parameters a, b, u, v. The force and frequency shift were then obtained from the fitted curve by differentiation with respect to d [121, 144]. In agreement with our experimental findings (Fig. 5.3e), we observe maximal attractive forces on the order of 100 pN above the hollow sites of the molecule and less attractive forces above the C-C bonds. The difference in the forces above these two sites increases with decreasing distance. The differentiation with respect to d shifts the minimum in the $F_z(d)$ and $\Delta f(d)$ curves to greater distances (≈ 0.45 Å for each differentiation [144]) compared to the $E(d)$ curve, and accordingly, atomic contrast is observed already at greater distances in Δf than in F_z and in E.

In Fig. 5.5e,f, calculated and experimental force-distance curves above different molecular sites (indicated in the inset of Fig. 5.5e) are compared. The experimental curves were extracted from the same data set as those shown in Fig. 5.3e, where the contribution of the metal part of the tip has been subtracted to achieve better comparability with our simplified theoretical model. We use different distance scales for the experimental (z) and theoretical data (d). In principle, they could be related to each other, for example by comparing the positions of the force minimum above a certain molecular site. However, the experimental z position of the force minimum was found to vary significantly between measurements with different CO tips. We attribute this to the fact that the tunneling current, and hence the tip height corresponding to the STM set point, strongly depends on the exact adsorption geometry of the CO at the tip apex. Therefore, we abstain from giving an explicit relation between z and d. In Fig. 5.5e,f, we observe good qualitative agreement between the calculated and experimental curves in terms of the maximal values of the force and the relative order in which

these maxima are reached above the different sites. Also quantitatively, the agreement is excellent for distances $d > 5\,\text{Å}$. For closer distances, the calculations seem to overestimate the force differences between the different sites. These discrepancies might be due to the simplifications of the theoretical model, namely neglecting the substrate and the metal part of the tip.

Our simulations of the CO–pentacene interaction take into account the different forces discussed in Chapter 2.3.1: electrostatic force, vdW force, and short-range chemical force. Comparing their contributions to the calculated overall force, we found that the electrostatic force is small ($\sim 10\,\%$) compared with the vdW force. These two contributions show little variation on the atomic scale, and together they yield a diffuse attractive background that gives rise to the dark halos surrounding the molecules in the Δf images. The atomic contrast in our images is therefore due to a short-ranged chemical interaction that leads to a repulsive force contribution varying on the atomic scale. The origin of this repulsive interaction is the Pauli exclusion principle, which leads to an energy increase when regions of high electron density in the two molecules overlap. Within a molecule, these regions are concentrated at the positions of atoms and bonds, and the total electron density can be used as a qualitative explanation of the contrast in atomically resolved AFM images (see Chapter 8) [150].

We conclude that atomic resolution in AFM images of single molecules can only be achieved in a tip–sample distance region where repulsive forces give significant contributions. To be able to operate at such close distances, while still maintaining stable imaging conditions, a modification of the tip with suitable atomic or molecular terminations is necessary. With the CO tip termination, we achieved the highest resolution, but comparison with other tip terminations that yield qualitatively different contrasts might be necessary to enable imaging with chemical contrast [151].

CHAPTER 6

Investigation of a switchable atom-molecule complex

The concept of using single atoms and molecules as memory elements or switches in electronic devices was established long ago and promises to drastically reduce the energy consumed by such devices and allow faster switching cycles [1]. Scanning tunneling microscopy has been used repeatedly to identify and characterize promising molecular switches at the level of single molecules, due to its atomic-scale imaging and manipulation capabilities [19, 27, 152–158]. Using such manipulation procedures, it was also possible to induce with an STM tip the controlled making and breaking of single chemical bonds between metal atoms and molecules [10, 13, 14, 26, 159] and between molecules [11, 160]. Those previous examples of STM-induced bond formation, however, were not suited as molecular switches for several reasons: They required complex protocols of STM tip positioning, voltage pulses or current injection, involved various possible configurations of the constituents, or resulted in only a slight change of the tunneling current. Furthermore, the examples mentioned lacked the possibility of switching between the bonded and the nonbonded configuration in a reliable and directed manner (meaning that it should be possible to switch with certainty to the desired state).

In this chapter, we describe a molecular switch based on the reversible bond formation between a Au adatom and a PTCDA (perylene-3,4,9,10-tetracarboxylic dianhydride) molecule on NaCl(2ML)/Cu(111) [143]. We have found that the Au-PTCDA complex can be switched between a bonded

and a nonbonded configuration in a reversible and highly repeatable manner. The bond making and breaking were controlled simply by applying voltage pulses of according polarity and did not require an exact tip movement or positioning over a particular part of the molecule. The operation and electronic characterization of the switch were performed with STM, as described in the first part of this chapter. From the experimental STM data, we are able to draw a clear-cut picture of the charge states of the complex in its different configurations. This picture is fully confirmed by DFT calculations of the electronic structure of the complex, which were done in the group of Prof. Persson in Liverpool. Next, we describe, how the exact atomic geometry of the complex before and after switching was determined using the method of atomically resolved AFM imaging with a CO-functionalized tip, which was described in the preceding chapter. Finally, we propose a new mechanism of bond formation that involves different charge states of the complex in the two configurations and is responsible for the high reliability of the switching compared to previous studies of STM-induced bond formation. This study exemplifies the high degree of insight into atomic-scale processes that can be obtained by combining information about the atomic structure of a molecular system from atomically-resolved AFM imaging with the information about its electronic structure from STM imaging and spectroscopy.

6.1 Bond formation as a reliable molecular switch

In Fig. 6.1, the switching of a Au-PTCDA complex on NaCl(2ML)/Cu(111) is shown. First of all, a single Au adatom and a PTCDA molecule had to be brought together close enough to enable a bond activation. To this end, we used vibrational excitation by inelastic electron tunneling into a negatively charged Au adatom (identified by its characteristic surrounding depression [17]) to successively move it towards a PTCDA molecule. To move the Au^-, we would position the tip over the center of the adatom, retract it by $z = -1.2$ Å from the STM set point ($I = 2.7$ pA, $V = 0.2$ V), and apply a voltage pulse of -1.5 V, which would lead to a lateral motion of the atom in a more or less random direction. Once the Au^- and the PTCDA had been positioned close enough to each other (Fig. 6.1a), it was possible to switch the complex to a different state by ramping the sample bias voltage

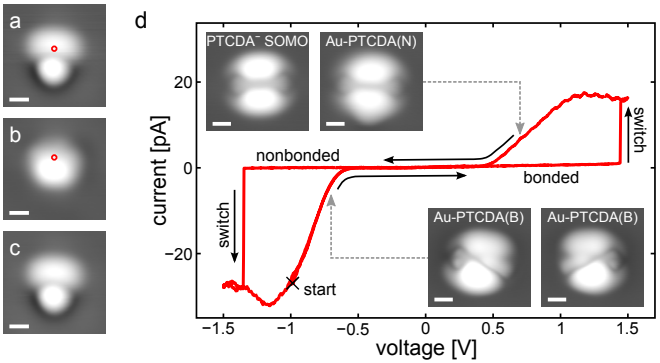

Fig. 6.1 Reversible switching of a Au-PTCDA complex on NaCl(2ML)/Cu(111). **a**, STM image of a Au^- adatom within close proximity of a PTCDA molecule. With the tip at the position indicated by the red circle, the bias voltage was ramped to $V = -1.5\,\mathrm{V}$. A sudden jump in the tunneling current indicated the successful modification of the complex. **b**, In the subsequent image, the constituents of the complex no longer appear separated. **c**, By ramping the voltage to $V = 1.5\,\mathrm{V}$, the complex was switched back to the initial state. **d**, I-V curve corresponding to a complete switching cycle, measured with the tip above the center of the complex. The voltage cycling is indicated by the black arrows. The insets show STM orbital images of PTCDA and the different states of Au-PTCDA. Imaging parameters: $I = 5\,\mathrm{pA}$ for all images, $V = 0.2\,\mathrm{V}$ in **a-c**, and $V = 0.8$, 0.7, and $-0.7\,\mathrm{V}$ for the orbital images of PTCDA, Au-PTCDA(N), and Au-PTCDA(B), respectively. Scale bars: 5 Å.

to $V = -1.5\,\mathrm{V}$. A sudden increase in the tunneling current indicated the successful manipulation, and in the subsequent STM image (Fig. 6.1b), the adatom and the molecule no longer appear as separate entities. The switching process was found to be completely reversible, as it was possible to switch back the complex to its initial configuration by ramping the voltage to $V = 1.5\,\mathrm{V}$ (Fig. 6.1c). We never observed spontaneous switching of Au-PTCDA in either direction; both configurations of the complex appeared to be indefinitely stable at the sample temperature of $T \approx 5\,\mathrm{K}$, at which all our experiments were performed. In the following, we refer to the two different states of the complex in Fig. 6.1a,b as the nonbonded [Au-PTCDA(N)] and the bonded [Au-PTCDA(B)] configuration, respectively.

Using STM imaging and spectroscopy, we studied the adsorption sites, charge states, and the electron and hole addition spectra of Au-PTCDA in the two configurations. The adsorption sites were determined from STM images in which the NaCl substrate was atomically resolved. We found that PTCDA adsorbs in two different geometries, with the long molecule axis oriented either along the polar ⟨011⟩ or the nonpolar ⟨001⟩ atomic rows of the NaCl(100) surface. In both cases the molecule was found to be centered on a Cl site, in agreement with previous studies of the adsorption of PTCDA on alkali halides [161, 162]. The adsorption geometry of PTCDA remained unaffected by bringing the Au^- adatom within close proximity and switching to the bonded configuration. Therefore, the Au-PTCDA complex likewise has these two possible adsorption orientations. The ⟨011⟩ orientation was found to prevail, and all experimental and theoretical data presented in this chapter were obtained for this particular adsorption geometry.

We investigated the electronic structure of the different states of the complex by $\mathrm{d}I/\mathrm{d}V$ spectroscopy and STM imaging [25]. The $\mathrm{d}I/\mathrm{d}V$ spectrum of a single PTCDA molecule on NaCl(2ML)/Cu(111) has a distinct peak at $V \approx 0.8\,\mathrm{V}$, which we attribute to electron tunneling from the tip into the singly occupied molecular orbital (SOMO) of $PTCDA^-$ (an explanation why the PTCDA is assumed to be negatively charged will be given below). At voltages around $-1\,\mathrm{V}$, we also observed a peak. We ascribe this peak at negative bias to bipolar tunneling [163], because it shifted when varying the tip–sample distance, and the corresponding orbital images were similar to the SOMO image at positive bias but strongly tip-dependent. The two configurations of Au-PTCDA exhibited distinctively different spectra, as can be seen from the I-V curve shown in Fig. 6.1d. For Au-PTCDA(N), a high current was measured only for voltages above $+0.6\,\mathrm{V}$, whereas for Au-PTCDA(B), a high current was measured below $-0.6\,\mathrm{V}$. The corresponding orbital images are shown in the insets of Fig. 6.1d, together with an image of the SOMO of a single $PTCDA^-$ admolecule[1]. For Au-PTCDA(N), the image is simply given by the superposition of the image of the SOMO of $PTCDA^-$ and a circular protrusion at the position of the Au^- adatom. For Au-PTCDA(B), on the other hand, the orbital

1 For simplicity, we refer to STM images recorded at voltages corresponding to peaks in the $\mathrm{d}I/\mathrm{d}V$ spectrum of a molecule as orbital images, because of their close resemblance to contours of constant orbital density [25].

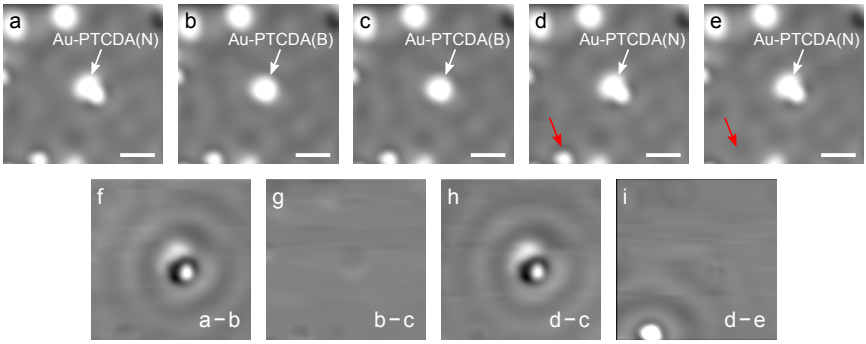

Fig. 6.2 Interface state scattering patterns around Au-PTCDA. **a-e**, STM images recorded at low bias voltage, showing the scattering wave pattern of the NaCl(2ML)/Cu(111) interface state around a Au-PTCDA complex ($I = 5\,\mathrm{pA}$, $V = 50\,\mathrm{mV}$). Between **a** and **b**, and between **c** and **d**, the complex was switched from the nonbonded to the bonded configuration and vice versa. Between **d** and **e**, a Au^- adatom at the location indicated by the red arrow was picked up with the STM tip. **f-i**, Corresponding difference images obtained by subtracting two STM images, as indicated in the bottom right corner of each panel. Scale bars: 20 Å.

was found to be strongly distorted, with an additional diagonally oriented nodal plane, in agreement with the DFT calculations discussed below. This indicates a strong coupling between the electronic states of the molecule and the Au atom, which is characteristic of the formation of a covalent bond [13]. Furthermore, we found that there exist two equivalent mirrored configurations of Au-PTCDA(B), which occurred with equal probability (lower insets in Fig. 6.1d). It should be noted that the I-V curve in Fig. 6.1d represents a complete switching cycle, demonstrating directed switching from the bonded to the nonbonded configuration and back. Furthermore, the switching was found to be highly reproducible: the complex could be switched back and forth several dozens of times, with only minor variations ($< 0.1\,\mathrm{V}$) in the switching voltage.

The charge state of adsorbates on NaCl(2ML)/Cu(111) is revealed in STM images by the scattering wave pattern of the substrate's interface state [17, 89]. A single PTCDA molecule was found to scatter the interface electrons to a similar extent as a Au^- adatom. Considering that the affinity

energy of PTCDA ($E_A \approx 4.6\,\text{eV}$ [164]) is substantially greater than the work function of the substrate ($\Phi \approx 3.9\,\text{eV}$ [95, 112]), we propose that PTCDA becomes singly negatively charged upon adsorption. The charge states of the Au-PTCDA complex in its two different configurations were studied by imaging scattering wave patterns with STM at low voltages, as shown in Fig. 6.2. For Au-PTCDA(N), the sombrero-shaped appearance of the Au atom indicates that it is negatively charged. The observed scattering pattern around Au-PTCDA(N), however, cannot be reconciled with the assumption that only the Au atom is charged, indicating that the entire complex is doubly negatively charged. When we switched the complex to the bonded configuration, we observed a clear change in the scattering wave pattern, with Au-PTCDA(B) still exhibiting the characteristic scattering of a charged species. This change in the scattering wave pattern becomes even clearer in the corresponding difference image (Fig. 6.2f), which is obtained by subtracting the topographies before and after switching [165]. The scattering pattern in this difference image is of similar intensity as the one obtained by subtracting two images before and after picking up a singly charged Au^- adatom from the surface (Fig. 6.2i). This similarity of the scattering patterns in the difference images suggests that Au-PTCDA(N) is more negatively charged than Au-PTCDA(B) by one elementary charge. Therefore, we propose that Au-PTCDA(B) is singly negatively charged, and Au-PTCDA(N) is doubly negatively charged.

To corroborate this picture, extensive periodic DFT calculations were carried out in the group of Prof. Persson in Liverpool. These calculations were done using the projector augmented wave method [166] as implemented in the plane-wave-based VASP code [167]. Exchange-correlation effects were described by the generalized gradient approximation [168]. As the (100)-terminated NaCl bilayer is incommensurate with the Cu(111) surface, the calculations were carried out for the closely related system NaCl(2ML)/Cu(100), for which the NaCl bilayer lattice is in good match with the Cu(100) surface lattice. The metal support was modeled by a four-layer slab of Cu atoms, the vacuum region was about 17.5 Å in height, and the surface unit cell was 23.1 Å × 15.4 Å. The full structural optimization of all the ion cores except the two bottom layers of the Cu slab was carried out using a plane wave cut-off of 400 eV on a $2 \times 2 \times 1$ k-point grid, until the forces acting on the ion cores were smaller than 0.03 eV/Å.

In Fig. 6.3a-c, simulated STM images of the orbitals of PTCDA, Au-

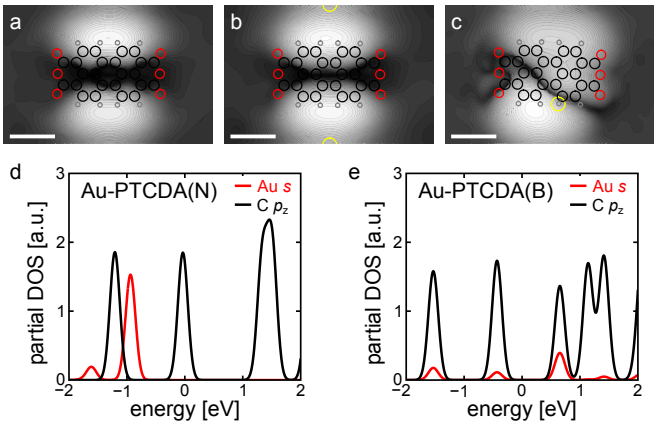

Fig. 6.3 DFT-calculated orbital images and partial densities of states. **a-c**, Simulated orbital images, given by topographical contours of constant local density of states for PTCDA (**a**), Au-PTCDA(N) (**b**), and Au-PTCDA(B) (**c**) on NaCl(2ML)/Cu(100). The SOMO is covered in **a** and **b** by integrating states in the energy intervals $[E_F - 0.1\,\text{eV},\ E_F + 0.8\,\text{eV}]$ and $[E_F - 0.1\,\text{eV},\ E_F + 0.7\,\text{eV}]$, respectively, whereas the HOMO is covered in **c** by integrating states in the interval $[E_F - 0.7\,\text{eV},\ E_F]$. The atomic positions of the molecule and the Au atom are overlaid; carbon, hydrogen, oxygen, and gold atoms are colored in black, gray, red, and yellow, respectively. Scale bars: 5 Å. **d**,**e**, Partial densities of electronic states of s and p_z partial waves around the Au atom and all the C atoms, calculated for Au-PTCDA(N) (**d**) and Au-PTCDA(B) (**e**) on NaCl(2ML)/Cu(100). The energies are given with respect to the Fermi level.

PTCDA(N), and Au-PTCDA(B) are shown. These simulated images compare very well to the experimental orbital images shown as insets in Fig. 6.1d (the Au adatom does not appear in Fig. 6.3b, because the Au 6s state does not have any overlap with the PTCDA$^-$ SOMO). This good agreement supports our approach to use Cu(100) as the metal substrate in the calculations, instead of Cu(111) as in the experiments. To corroborate the assignment of the charge states to the different states of the Au-PTCDA complex, the partial densities of states (DOS) of s and p_z waves around the Au atom and the C atoms (i.e. the DOS projected onto Au 6s and C p_z atomic orbitals, respectively) are shown in Fig. 6.3d,e. The occupation of

molecular orbitals is revealed by the location of the corresponding peaks in the partial DOS with respect to the Fermi level. For Au-PTCDA(N), the partial DOS of the s and p_z partial waves remain essentially the same as for the single adatom and the single PTCDA admolecule. Upon adsorption, the 6s state of the Au atom becomes fully occupied and the LUMO of the PTCDA molecule, being of π character, becomes a SOMO partially occupied by one electron, which confirms our assumption that Au-PTCDA(N) is doubly negatively charged. In contrast, the partial DOS for Au-PTCDA(B) indicates the formation of a covalent bond arising from the strong mixing of the Au 6s state with the π orbitals of the PTCDA admolecule. In this case, there are no partially occupied molecules, and the calculations show that Au-PTCDA(B) is occupied with one electron less than Au-PTCDA(N), which confirms that Au-PTCDA(B) is singly negatively charged. It should be noted that the different work function of the Cu(100) substrate used in the calculations (4.59 eV for Cu(100) [169] versus 4.85 eV for Cu(111) [170]) could have an influence on the stability of the different charge states of adsorbates. Therefore, our comparison between experiment and theory only regards the clear assignment of the different charge states of the Au-PTCDA complex (which is supported by the excellent agreement between the experimental and theoretical evidence for these charge states), but we do not attempt to extract any quantitative information, for example about the energy barrier for switching between the different states.

6.2 Determination of the bonding geometry

The exact nature of the apparent conformational change that the Au-PTCDA complex undergoes when switched between the two states is not clear from the STM images presented in Fig. 6.1. The STM data together with the ab initio calculations indicate that a covalent bond is formed between the Au atom and the molecule when switching from Au-PTCDA(N) to Au-PTCDA(B). To determine the exact geometry of this metal-molecule bond, we recorded atomically resolved AFM images and compared them to the relaxed atomic positions obtained from DFT calculations. For the measurements, we used a CO-terminated tip, which yielded enhanced resolution also in topographical STM imaging (Fig. 6.4a,b). In the corresponding constant-height AFM images (Fig. 6.4c,d), the perylene core of the PTCDA

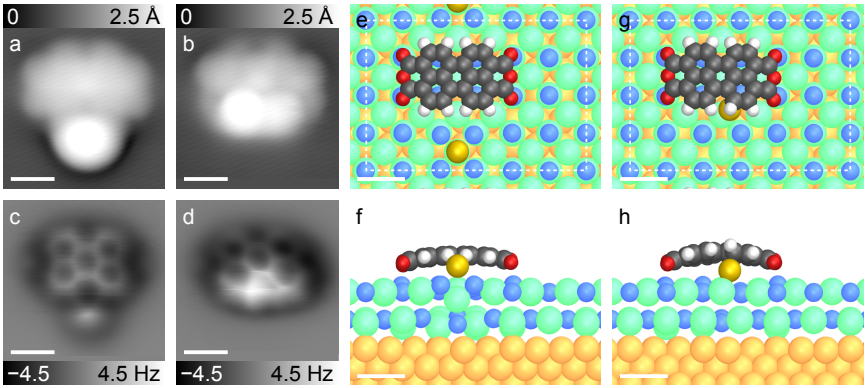

Fig. 6.4 Bonding geometry of Au-PTCDA. **a**,**b**, STM images of Au-PTCDA in the nonbonded (**a**) and the bonded (**b**) configuration ($I = 3\,\text{pA}$, $V = 0.2\,\text{V}$). The tip was terminated with a CO molecule. **c**,**d**, Corresponding constant-height AFM images ($A = 0.4\,\text{Å}$, $z = 0.8$ and $1.0\,\text{Å}$ from the STM set point over the substrate). **e**-**h**, DFT-calculated geometries of the complex in the nonbonded (**e**,**f**) and the bonded (**g**,**h**) state. Carbon, oxygen, hydrogen, chlorine, sodium, copper, and gold atoms are colored in gray, red, white, green, blue, orange, and yellow, respectively. The unit cell used for the calculations is indicated by the white dashed lines in (e) and (g). Scale bars: 5 Å.

is clearly resolved, in contrast to the STM images. For Au-PTCDA(N), the AFM image shows that the molecule and the adatom are clearly separated, with the distance between the Au atom and the center of the central carbon ring of the PTCDA being close to twice the Cl-Cl distance in the topmost NaCl layer. After switching to Au-PTCDA(B), in both the STM and AFM images we observe that while the PTCDA basically maintains its position, the Au atom no longer appears separated from the molecule. In the AFM images of Au-PTCDA(B), the brightness of the lower part of the atom-molecule complex is enhanced, which corresponds to a stronger Pauli repulsive force and indicates that this region of the molecule is closer to the tip. A distinct maximum is observed above one of the two inner C sites at the lower edge of the molecule, and the two mirrored configurations can be clearly distinguished. This suggests that upon switching from Au-PTCDA(N) to Au-PTCDA(B), the Au adatom moves towards the PTCDA

molecule and is then located underneath one of the C atoms at the lower edge of the molecule. This picture is fully confirmed by the DFT calculations shown in Fig. 6.4e-h. The PTCDA was found to be centered on a Cl^- ion, with the oxygen end-groups bent towards the substrate (this could explain why these atoms are not visible in the AFM images), similar to the situation on metal surfaces [171]. A stable configuration was found with the Au atom adsorbed on top of a Cl site two atom rows away from the adsorbed PTCDA molecule, which corresponds to the observed nonbonded configuration. Bringing the Au atom closer to the molecule, we found two equivalent mirrored configurations with the atom bonded to the PTCDA. The Au atom is one Cl site closer to the molecule than in Au-PTCDA(N) and bonds to a Cl^- ion and a C atom by tilting the H atom away from the molecular plane, which indicates an sp^2 to sp^3 rehybridization of the C atom [13]. This tilting is consistent with the enhanced brightness observed above one of the C sites at the lower edge of the molecule in Fig. 6.4d.

6.3 Proposed mechanism of bond formation

The detailed knowledge of both electronic and structural properties of the Au-PTCDA complex, gained from the combination of STM, AFM, and DFT, leads us to the conclusion that a particular mechanism of bond making and breaking must be responsible for the expedient characteristics of this molecular switch. We propose such a new mechanism of bond formation, which is shown schematically in Fig. 6.5. For Au-PTCDA in the nonbonded state, we conclude from the STM and DFT data that the adatom and the molecule are both negatively charged. The negative charges repel each other and stabilize the constituents of the complex in the nonbonded configuration, with the Au^- two Cl sites away from the center of the $PTCDA^-$ (Fig. 6.5a). When the sample voltage is ramped to a certain negative bias, electrons tunnel out of the SOMO of $PTCDA^-$, thus temporarily neutralizing the molecule and reducing the repulsive Coulomb interaction between the two adsorbates (Fig. 6.5b). If the hole attachment to the SOMO state is sufficiently long-lived, this can enable the Au adatom to move towards the PTCDA and form the bond with the molecule (Fig. 6.5c). In the energy landscape of the excited state, the barrier between the nonbonded and bonded configuration of the complex

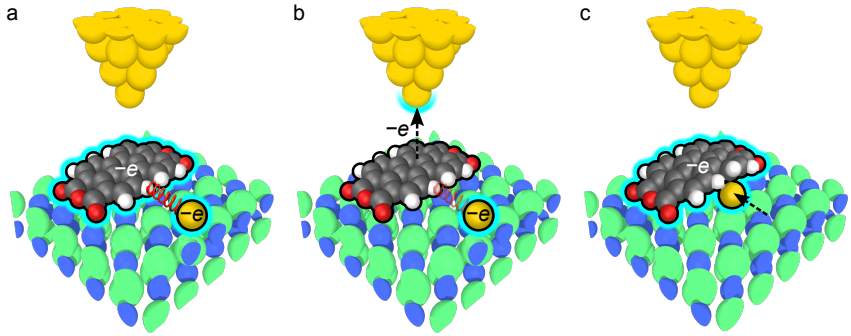

Fig. 6.5 Illustration of the proposed switching mechanism of Au-PTCDA. **a**, The complex in the nonbonded configuration is stabilized by the Coulomb repulsion between the negative charges on the $PTCDA^-$ and the Au^-. **b**, By tunneling out of the SOMO of $PTCDA^-$ at negative sample bias voltage, the molecule is temporarily neutralized and the repulsive interaction between the two adsorbates is reduced. **c**, This allows the Au^- adatom to change its position and form a bond with the molecule. The entire complex is now only singly negatively charged. The positions of the atoms of the NaCl substrate and the Au-PTCDA complex are derived from the DFT calculations shown in Fig. 6.4, whereas a tip apex with arbitrary atomic structure has been included for illustrative purposes.

should thus be greatly reduced or even vanish completely. Reversibly, the attachment of a long-lived electron to the LUMO state of Au-PTCDA(B) would lead to an increased Coulomb repulsion between the molecule and the adatom, thus destabilizing the complex in the bonded configuration and inducing the breaking of the bond. To provide a clear-cut proof for this picture, extensive further calculations, for example using DFT with the nudged elastic band method, would be necessary. This is beyond the scope of this work, but there are two simple experimental findings that support our hypothesis: First, the bond formation always occurred by the Au atom moving towards the PTCDA molecule, even when we ramped the voltage with the tip positioned at the opposite end of the molecule. This suggests that the mechanism at work is different from bond activation by simple inelastic excitation of one of the constituents, which was used in the case of STM-induced bond formation between Au and pentacene [13] (in this case one would expect the molecule to change its position when it is mechanically

excited by inelastic electron tunneling into one of the molecular orbitals). Second, we never found a neutral Au^0 at such close distance to a PTCDA molecule as the Au^- in Au-PTCDA(N). This supports the idea that the adsorbates are stabilized in this position by the repulsion of their negative charges.

In conclusion, we have found that reducing the barrier for bond formation by a transient modification of the charge state can lead to a much more reliable bond formation than mechanical excitation of the system over that barrier. This finding might emerge as an important guiding principle in future studies which involve the assembly of atomically well-defined molecular circuits.

CHAPTER 7

Imaging the structure of an unknown molecule

Nature provides us with a huge and only partially explored variety of small molecules, often with potential pharmaceutical applications. In particular the marine environment offers a range of diverse habitats from which sources of such natural products can be obtained; marine organisms often produce metabolites with novel chemical structures and potent biological activities. A number of well-established characterization methods exist for structure elucidation of natural products [172], including spectroscopic techniques such as nuclear magnetic resonance (NMR) spectroscopy and mass spectrometry. However, for certain classes of natural products, these established techniques may not succeed in the unambiguous determination of the chemical structure of an unknown compound. Here we show that our technique of atomic-resolution molecular imaging with AFM can help in such cases [139]. We study a natural product extracted from a sample collected in the deep sea, for which the spectroscopic data were not sufficient for an unambiguous structure determination. The combination of the NMR and mass spectrometry results with AFM imaging and DFT calculations eventually enabled the identification of the compound as cephalandole A, a structure which had been previously misassigned.

7.1 Structure elucidation with NMR and AFM

Although a number of powerful methods for structure elucidation are available, the ab initio structural characterization of natural products can be very challenging. This is particularly the case when an X-ray crystallographic solution is not possible because suitable crystals cannot be grown. When NMR methods are used instead, certain structures are problematic, which have their carbon skeleton interrupted by heteroatoms, or structures that contain only a small number of protons or have quaternary carbon atoms that show no long-range correlations to protons [172]. Such features are often present in planar molecules isolated from a range of marine microorganisms [173]. In these cases, the structure often cannot be confirmed without a complex and time-consuming synthesis process [174, 175]. Here we demonstrate the first successful use of atomic-resolution noncontact-AFM to assist in the identification of a natural product.

In their search for novel natural products with potential pharmaceutical applications, the group of Prof. Jaspars in Aberdeen worked with the pressure-tolerant actinobacterium *Dermacoccus abyssi*, which had been isolated from a sediment collected by the unmanned Japanese submarine *Kaikō* from the deepest place on earth, the Challenger Deep in the Mariana Trench [176]. They extracted several compounds of interest from this bacterium, one of them the metabolite that is the object of this study. The chemical formula of this metabolite was quickly identified as $C_{16}H_{10}N_2O_2$ by high-resolution mass spectrometry. Structure elucidation with state-of-the-art NMR spectroscopy relies heavily on the use of two-dimensional techniques, such as correlation spectroscopy (COSY) and heteronuclear multiple bond correlation spectroscopy (HMBC), which detect interactions of protons with neighboring protons (2–4 bonds away) or with neighboring carbon atoms (2–3 bonds away), respectively. The Aberdeen group recorded 1D and 2D NMR data sets of the compound in question and were able to identify a complete set of substructures (Fig. 7.1a), including two alternative substitution patterns for the indole substructure that cannot be distinguished from the NMR data. These substructures could be assembled into the four possible working structures **1** to **4** shown in Fig. 7.1b. Structure **1** (which we were later able to identify as the correct structure of the metabolite) is known as cephalandole A and was originally isolated from the

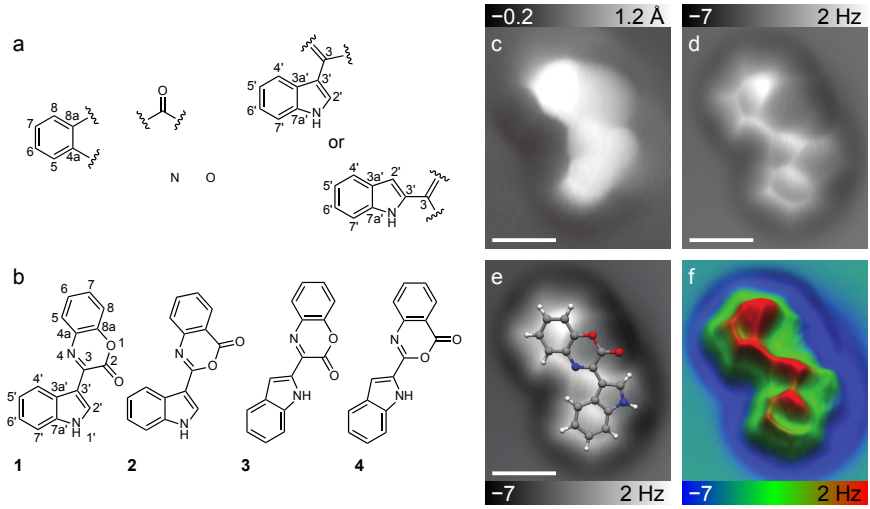

Fig. 7.1 Structure determination with NMR and AFM. **a**, Three substructures of the unknown compound could be identified from the NMR data. High-resolution mass spectrometry indicated the presence of further N and O atoms in the structure. The NMR data did not the allow distinction between a C2- or C3-substituted indole substructure. **b**, The substructures can be assembled into the four equally plausible structures **1** to **4**. **c**, Constant-current STM image of the unknown compound on NaCl(2ML)/Cu(111) ($I = 1.2\,\text{pA}$, $V = 0.15\,\text{V}$). **d-f**, Constant-height AFM measurement of the same molecule ($A = 0.5\,\text{Å}$, $z = 0.5\,\text{Å}$ from the STM set point). The images show the original data (**d**), the same image with an overlaid ball-and-stick model of **1** (**e**), and a low-pass filtered 3D representation of the data (**f**). Carbon, hydrogen, oxygen, and nitrogen atoms are colored in gray, white, red, and blue, respectively. Scale bars: 5 Å.

Taiwanese orchid *Cephalanceropsis gracilis* [177]. It exhibits all the features mentioned above that make structure analysis with 2D NMR spectroscopy especially difficult: the O and N atoms at positions 1 and 4 interrupt the carbon skeleton completely, the ratio of heavy atoms to protons is 2:1, and the C atom of the carbonyl group at position 2 is four bonds away from the nearest H atom and therefore not expected to show any correlations in HMBC spectroscopy. In fact, owing to these difficulties, the structure of cephalandole A had initially been misassigned as structure **2** in the original

investigation [177] and was only later corrected after both structures in question had been synthesized [178]. For us at this point, all working structures in Fig. 7.1b were equally plausible, as there were no HMBC correlations to guide in the assembly of the isolated substructures, and each bicycle in the proposed structures had been reported previously [178].

Next, we conducted STM and AFM measurements with CO-functionalized tips on individual specimens of the metabolite on NaCl(2ML)/Cu(111). The STM constant-current image in Fig. 7.1c shows submolecular resolution vaguely reminiscent of molecular images obtained with scanning tunneling hydrogen microscopy [179], but no clear structure identification is possible. In the constant-height AFM image (Fig. 7.1d), part of the molecular structure is resolved, with indications of atomic sites, bonds, and cyclic systems. As discussed in Chapter 5, the dark halo surrounding the molecule can be attributed to van der Waals and electrostatic interactions between the tip and the molecule, whereas atomic corrugation is due to Pauli repulsive forces, leading to bright features that reflect areas of high electron density such as atoms and bonds within the molecule [121]. Therefore, the bright features in the AFM images can be directly compared to the four proposed molecular structures. The placement of the indole bicycle becomes immediately clear, namely in the lower part of Fig. 7.1d, where a six-membered ring connected to a five-membered ring is visible. The structures **3** and **4** can already be ruled out at this point, because the angle between the two bicyclic systems within the molecule cannot be brought into accordance with the AFM measurements. This leaves only cephalandole A (**1**) and the previously misassigned structure **2** as remaining candidates. In Fig.7.1e, the structural model of **1** is overlaid on the AFM image. Unfortunately, the molecular structure is not resolved on the entire molecule, and structure **2** cannot be excluded at this stage, because no atomic contrast is observed in the region around C2 that distinguishes the two structures. The limited contrast in this region might be due to chemical sensitivity (different interactions with different atomic species) or a nonplanar topography of the molecule. It should be noted that all molecules observed on the surface (more than 100) exhibited similar contrast in the STM images, except for a mirrored configuration, which we attribute to the molecule being adsorbed with the opposite side facing the surface. High-resolution AFM images recorded for about ten different specimens all showed qualitatively the same (or mirrored) contrast, indicating that only one molecular species was

present in the purified sample.

7.2 Determination of the adsorption position

We show now that the exact adsorption position and orientation of the investigated metabolite on the substrate can serve as an additional criterion for the distinction between the remaining two possible structures. To experimentally determine the adsorption geometry of the metabolite on NaCl(2ML)/Cu(111), we recorded AFM images with STM feedback, i.e., we scanned the tip on a constant-current topography while at the same time oscillating the tuning fork and recording the frequency shift signal. Such a constant-current Δf image is shown in Fig. 7.2a-c. In this measurement mode, the STM and AFM signals are convoluted, which makes a quantitative interpretation of the images difficult. On the other hand, this mode enables atomic resolution on the molecule and the substrate at the same time, without being as involved and time-consuming as the 3D force mapping method presented in Chapter 5. The faint bright maxima visible in the high-contrast representation of the Δf data in Fig. 7.2a can be attributed to the Cl sites of the substrate, by comparison with the STM constant-current topography [92, 139]. In the low-contrast representation of the same data in Fig. 7.2b, the six-membered ring structures of the molecule are clearly visible and the proposed molecular structures can be overlaid (Fig. 7.2c). In Fig. 7.2d, a model of the adsorption position extracted from the experiment is shown. Assuming structure **2** instead of **1** would have led to identical results, because the region around C2 is not atomically resolved in the constant-current AFM image and therefore not taken into account when matching the image with the molecular model.

– Nikolaj Moll of the Computational Science department at IBM Research – Zurich carried out DFT calculations of the adsorption geometries of the possible molecular structures **1** and **2**. In these calculations, the substrate was modeled as a four-layer NaCl slab, and the molecule was initially placed on the surface in the experimentally determined geometry. From this starting condition, all atoms in the system except the two bottom layers of the NaCl slab were fully relaxed, which yielded the energetically most favorable adsorption positions for structure **1** (Fig. 7.2e) and **2** (Fig. 7.2f). When comparing the experimental and calculated adsorption positions, we

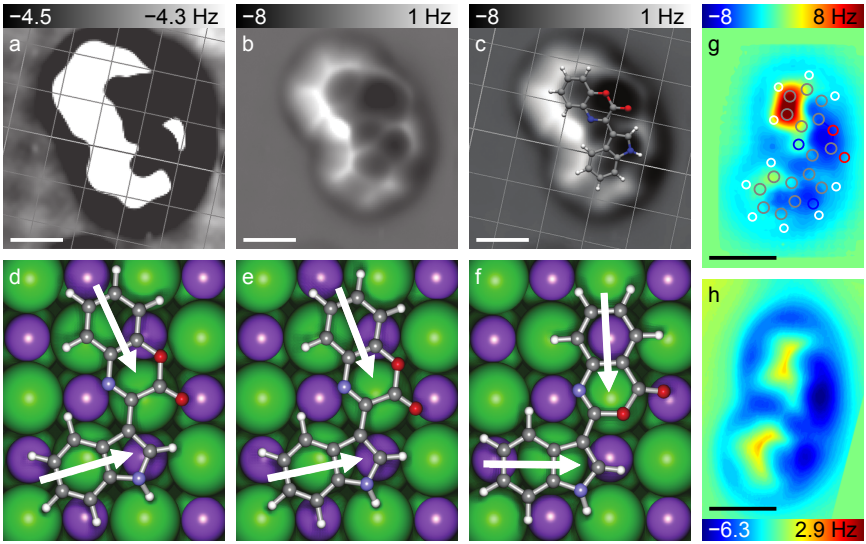

Fig. 7.2 Determination of the adsorption position of the unknown compound. **a-c**, Constant-current AFM images on NaCl(2ML)/Cu(111) ($I = 1.2\,\text{pA}$, $V = 0.15\,\text{V}$, $A = 0.5\,\text{Å}$). The images show the same data with different Δf scales. At high contrast (**a**), the atomic positions of the substrate can be deduced and a grid indicating the Cl sites is overlaid. At lower contrast (**b**), the molecular position and orientation can be deduced. In **c**, the Cl grid and the model of structure **1** are overlaid. **d**, Adsorption geometry deduced from the experimental data. **e,f**, DFT-calculated adsorption geometries for structures **1** and **2**, respectively. White arrows indicate the orientations of the bicyclic systems. **g**, DFT-simulated map of the frequency shift above structure **1** (distance $d = 7.88\,\text{Å}$ from the C atom of the CO tip to the topmost NaCl layer). **h**, Constant-height AFM image with CO-functionalized tip ($A = 0.5\,\text{Å}$). Carbon, hydrogen, oxygen, and nitrogen atoms are colored in gray, white, red, and blue, respectively. Scale bars: 5 Å.

find good agreement for structure **1**, but a clear mismatch for structure **2**, where the in-plane orientation of the molecule differs significantly from the experimental data. Therefore, we can rule out **2** as a possible structure of the investigated metabolite, leading to the final structural assignment as cephalandole A (**1**). To confirm this assignment, a simulation of a CO-tip AFM image of cephalandole A was performed, using the same method as

in Chapter 5.4. This DFT-simulated constant-height Δf map is shown in Fig. 7.2g and compared to the experimental Δf image in Fig. 7.2h. For the DFT simulation, the relaxed atomic positions of cephalandole A on NaCl were used, but the substrate was found to have no influence on the calculated frequency shift and was therefore neglected in the final calculation of the Δf image. In the measurement shown in Fig. 7.2h, the tip height was about 0.15 Å greater than in the measurement shown in Fig. 7.1d, resulting in slightly reduced contrast. At this distance, we observe good qualitative agreement between the experimental and calculated Δf images. In both images, local minima are observed near the positions of the oxygen atoms and the NH group, which agree well in shape and relative intensity. From the calculations, we find that the molecule–substrate interaction is maximal at these sites, which are therefore relaxed towards the substrate. The calculated distances of the surrounding atoms to the topmost NaCl layer are $h(\mathrm{O1}) = 2.68$ Å, $h(\mathrm{O2}) = 2.52$ Å, and $h(\mathrm{N1'}) = 2.69$ Å. Accordingly, at the opposite edge of the molecule, the distances to the substrate are found to be maximal ($h(\mathrm{C5}) = 3.23$ Å, $h(\mathrm{C4'}) = 2.97$ Å), which explains the pronounced maxima observed in the Δf image at the positions of the C5–C6 and C4'–C5' bonds. The DFT calculations for structure **2**, on the other hand, yielded a more planar adsorption geometry, with even a slight outward relaxation of the oxygen atom in the six-membered ring ($h(\mathrm{C5}) = 2.89$ Å, $h(\mathrm{C4'}) = 2.89$ Å, $h(\mathrm{O2}) = 2.92$). This molecular topography is in clear disagreement with the experimental results, which lends further support to our structural assignment.

CHAPTER 8

Imaging the charge distribution within a molecule

The Kelvin probe force microscopy (KPFM) method described in Chapter 2.3.2 allows imaging of the local contact potential difference (LCPD) between the scanning probe tip and the sample surface with high lateral resolution. With KPFM, the LCPD was measured for a wide range of surfaces, in some cases even with atomic resolution [105, 106, 108, 109]. In Chapter 4, we have shown that KPFM can be used to study charge states of single metal atoms on thin insulating films [110], and similar results have been reported for atomic point defects [180] and molecules [181]. Furthermore, we have demonstrated submolecular resolution in AFM imaging and force-distance spectroscopy of single molecules with CO-terminated tips in Chapter 5. These results suggest the possibility of combining the high charge sensitivity of KPFM with submolecular lateral resolution to measure the charge distribution within single molecular adsorbates. However, the exact imaging mechanism of atomic-resolution KPFM is still under discussion [106, 182], and no submolecularly resolved KPFM images have been presented until now.

Here we demonstrate for the first time KPFM imaging with submolecular resolution [150]. As a model system, we chose the molecule naphthalocyanine, which can be switched controllably between two tautomerization states [27]. As described in the first part of this chapter, we used STM and AFM experiments in combination with DFT calculations to show that there exists a quadrupole-like charge distribution in the four lobes of the

naphthalocyanine molecule. Next, we show that this charge distribution is reflected in images of the LCPD acquired with a metal-terminated tip. These KPFM images compare very well to the calculated electric field distribution above the free molecule. Finally, we demonstrate that also in KPFM imaging, the CO-terminated tip greatly enhances the resolution, which enables imaging of the charge distribution within the molecule on the atomic scale.

8.1 Ideal model system for KPFM imaging

To unambiguously demonstrate that we can measure LCPD maps with submolecular resolution, we chose to investigate single naphthalocyanine molecules on NaCl(2ML)/Cu(111). This system constitutes a molecular switch based on the current-induced movement of the two inner hydrogen atoms in the free-base naphthalocyanine molecule, as shown in a previous STM study [27]. It has several advantages for our purpose: The insulating NaCl film efficiently decouples the adsorbed molecules from the underlying metal, which prevents a strong hybridization with the substrate electron states and facilitates the comparison of our results with calculations carried out for the free naphthalocyanine molecule. Furthermore, by comparing images of the different tautomers (which correspond to different adsorption orientations of the molecule), we can rule out that the contrast in the LCPD images is disturbed by a possible asymmetry of the microscope tip or the underlying substrate. The molecule maintains a flat adsorption geometry in both states, and the tautomerization switching involves only a minor structural change. This excludes spurious geometrical effects on the measured LCPD that might be expected for systems in which the switching of a molecule is accompanied by a major change in the molecular structure [181].

In Fig. 8.1a, a constant-current STM image of a naphthalocyanine molecule on NaCl(2ML)/Cu(111) is shown, recorded at a bias voltage of $V = 0.25\,\mathrm{V}$. At this voltage, the molecule appears as a cross-like structure, with a central protrusion surrounded by four lobes. There is no apparent asymmetry between the lobes parallel (H-lobes) and perpendicular (N-lobes) to the two inner hydrogen atoms. This changes when the bias voltage is increased to $V = 0.6\,\mathrm{V}$ (Fig. 8.1b). This voltage corresponds to

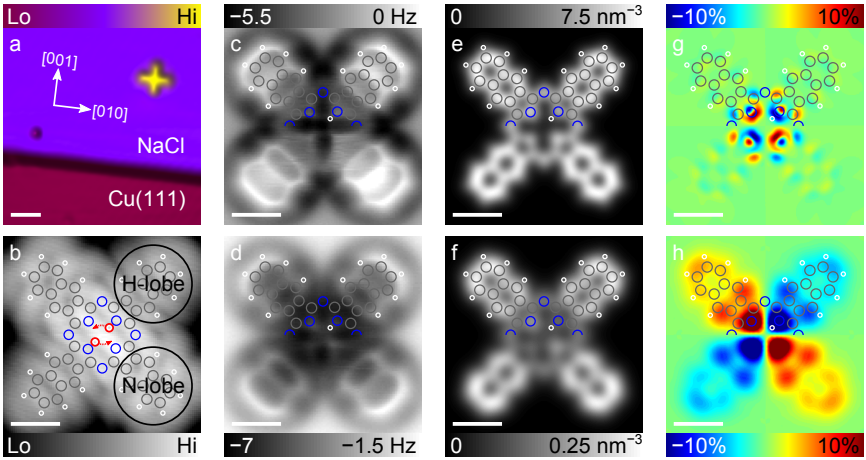

Fig. 8.1 STM and AFM imaging of naphthalocyanine on NaCl(2ML)/Cu(111). **a**, STM constant-current image ($I = 2\,\text{pA}$, $V = 0.25\,\text{V}$) recorded at the edge of a NaCl island. A single naphthalocyanine molecule (yellow) and a single CO molecule (depression close to the NaCl step edge) can be identified. The crystallographic directions of the topmost NaCl layer are indicated. **b**, STM constant-current image of a naphthalocyanine molecule ($I = 2\,\text{pA}$, $V = 0.6\,\text{V}$), recorded with a CO-terminated tip. The positions of the central hydrogens and the tautomerization path are highlighted in red, and the definition of H-lobes and N-lobes is illustrated. **c**,**d**, Constant-height AFM images of the same molecule measured with a CO-terminated tip. The images were recorded at distances $z = 1.45\,\text{Å}$ (**c**), and $z = 1.75\,\text{Å}$ (**d**) from the STM set point ($I = 2\,\text{pA}$, $V = 0.2\,\text{V}$) over the substrate ($A = 0.3\,\text{Å}$). **e**,**f**, DFT-calculated electron density at distances $d = 2.0\,\text{Å}$ (**e**) and $d = 3.0\,\text{Å}$ (**f**) from the molecular plane. **g**,**h**, Asymmetry of the calculated electron density at $d = 1.0\,\text{Å}$ (**g**) and $d = 4.0\,\text{Å}$ (**h**) from the molecular plane. The DFT-calculated atomic positions are overlaid in **b** and in the upper halves of **c**-**h**. Carbon, hydrogen, and nitrogen atoms are colored in gray, white, and blue, respectively. Scale bars: 20 Å in **a** and 5 Å elsewhere.

the lowest unoccupied molecular orbital (LUMO) resonance, and an image closely related to the orbital of the free molecule is obtained [25, 114]. The LUMO of naphthalocyanine has a twofold symmetry, with a central nodal plane along the N-lobes. Thus, we are able to unambiguously determine the tautomerization state (i.e., the positions of the inner hydrogen atoms) from STM images recorded either with a metal-terminated tip [27] or, as shown

in Fig. 8.1b, with a CO-terminated tip [114]. After switching to constant-height mode we recorded AFM images of the same molecule (Fig. 8.1c,d). The images were acquired at two different tip–sample distances and exhibit clear atomic resolution of the C_6 rings in all four lobes. For the closer tip–sample distance (Fig. 8.1c), the molecule appeared fourfold symmetric. When we increased this distance, however, the symmetry was reduced to twofold, and a distinct asymmetry developed in the center region of the molecule, with brighter protrusions at the hydrogen-free N sites (Fig. 8.1d, see also Appendix B for a complete 3D force map measurement). This behavior is reproduced in DFT-calculated maps of the CO–naphthalocyanine interaction energy shown in Appendix B, as well as in the calculated electron density of the free naphthalocyanine molecule shown in Fig. 8.1e,f (for a detailed description of the DFT calculations presented in this chapter, see Appendix B). This indicates that the atomic-scale contrast in the AFM images is mainly determined by the electron density at a certain height above the molecule.

To further expose the asymmetry in the electron density, the difference between the two configurations, $A_\rho = [\rho_{0^\circ}(x,y) - \rho_{90^\circ}(x,y)]/\max(\rho)$, is shown in Fig. 8.1g,h for different distances from the molecular (xy) plane. Here ρ_{0° denotes the calculated electron density for the configuration overlaid in Fig. 8.1g,h and ρ_{90° that for the tautomerized configuration (corresponding to a 90° rotation of the molecule). A_ρ is normalized with respect to the maximum value of the electron density at the respective height, to give a better impression of the relative magnitude of the asymmetry, expressed in percent. At close distance to the molecular plane, the asymmetry is most pronounced near the positions of the inner hydrogen atoms (Fig. 8.1g). There is only a small asymmetry between the H-lobes and the N-lobes, which arises from a slight elongation of the molecule along the direction of the H-lobes. Further away from the molecular plane, a much more extended asymmetry is observed, with higher electron density values above the N-lobes, even several bonds away from the center of the molecule (Fig. 8.1h). The asymmetry in the calculated charge distribution within the molecule yields a total quadrupole moment (including the charges of electrons and nuclei) of $0.14\,e\mathrm{nm}^2$, where e is the elementary charge. In a point-charge model, this would correspond to pairs of positive (H-lobes) and negative (N-lobes) charges of $\pm 0.1\,e$ located 5 Å from the center of the molecule. Apparently, the charge asymmetry between the different lobes does not

affect the AFM images in Fig. 8.1c,d, but we will show that it clearly manifests itself in images of the LCPD. The nonvanishing quadrupole moment together with the possibility of interchanging the positions of the donor-like H-lobes and the acceptor-like N-lobes by tautomerization switching makes this molecule an ideal system for demonstrating KPFM contrast caused by the intramolecular charge distribution.

8.2 KPFM imaging with a metal-terminated tip

For our KPFM measurements, we used the method illustrated in Fig. 8.2a: Similar to the force mapping procedure described in Chapter 5.3, the AFM tip was moved consecutively to the intersections of a lateral grid above the molecule. At each point, a $\Delta f(V)$ spectrum was recorded (inset, red circles), and the position of the maximum of the fitted parabola (inset, solid black line) yielded the LCPD value V^* as well as the frequency shift at compensated LCPD Δf^* for that point. Because the KPFM measurements take very long with this method (up to 33 h per image for the measurements described in this chapter), we again used the drift correction procedure based on the recording of an STM reference image (see Chapter 5.3) [140]. To unambiguously demonstrate the possibility of submolecular-resolution KPFM, we first present measurements with the well-understood metal-terminated tip obtained by indenting the tip into the bare Cu substrate. The LCPD images shown in Fig. 8.2b,c were recorded with such a tip before and after switching the tautomerization state of the imaged naphthalocyanine molecule. We observe a striking asymmetry between the H-lobes and the N-lobes, with greater values of V^* above the N-lobes. As expected, the tautomerization switching had the effect of a 90° rotation of the LCPD image of the molecule, which excludes that the observed asymmetry between the H-lobes and the N-lobes is due to an asymmetric tip or an effect of the underlying substrate. The asymmetry is even more pronounced in the difference image (Fig. 8.2d) obtained by subtracting the LCPD images of the initial and the switched configuration. The greater LCPD measured above the N-lobes would be expected for a charge asymmetry as in Fig. 8.1h (the more negatively charged N-lobes should lead to an increase in V^*, similar to the Au^- in Chapter 4). However, the charge density in Fig. 8.1h contains only the electrons in a certain plane above the molecule. A more

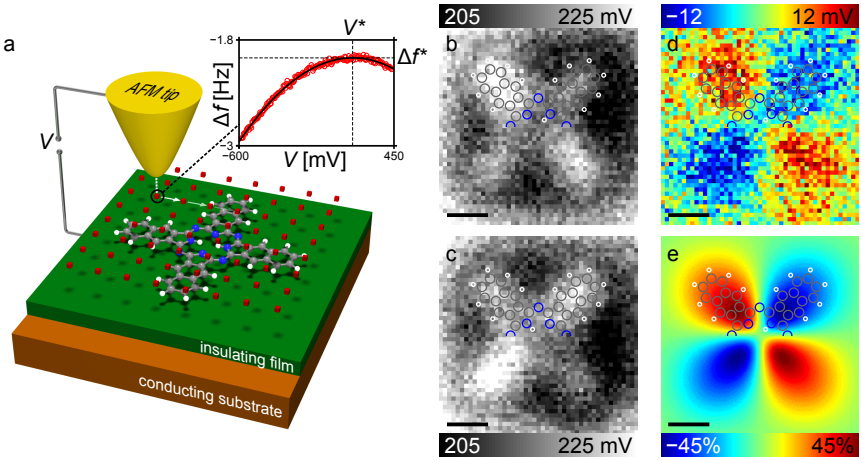

Fig. 8.2 LCPD images of the tautomerization switching of naphthalocyanine. **a**, Schematic of the measurement principle. At each tip position, the frequency shift is recorded as a function of the sample bias voltage (inset, red circles). The maximum of the fitted parabola (inset, solid black line) yields V^* and Δf^* for that position. **b**,**c**, LCPD images of naphthalocyanine on NaCl(2ML)/Cu(111) before (**b**) and after (**c**) switching the tautomerization state of the molecule. The images were recorded with a Cu-terminated tip on a 64×64 lateral grid at a distance $z = 1.0\,\text{Å}$ from the STM set point ($I = 3\,\text{pA}$, $V = 0.2\,\text{V}$) over the substrate ($A = 0.4\,\text{Å}$). **d**, Difference image obtained by subtracting **c** from **b**. **e**, DFT-calculated asymmetry of the z-component of the electric field above a free naphthalocyanine molecule at a distance $d = 5.0\,\text{Å}$ from the molecular plane. The DFT-calculated atomic positions are overlaid in the upper halves of **b**-**e**. Carbon, hydrogen, and nitrogen atoms are colored in gray, white, and blue, respectively. Scale bars: 5 Å.

appropriate quantity to compare with our LCPD measurements is the electric field generated by the distribution of the total charge within the molecule, including all electrons and nuclei. The normalized asymmetry of the calculated electric field, $A_E = [E_{0^\circ}(x,y) - E_{90^\circ}(x,y)]/\max(E)$, is shown in Fig. 8.2e at a distance $d = 5.0\,\text{Å}$ above the molecular plane. Here E_{0° and E_{90° denote the z-components of the electric fields obtained by differentiating the DFT-calculated electrostatic potential for the initial and switched configurations, respectively. The asymmetry of the field generated

by the quadrupole-like distribution of charge within the molecule exhibits a remarkable similarity to the experimental difference image in Fig. 8.2d. This leads us to the conclusion that the submolecular resolution in the LCPD images reflects the total charge distribution within the molecule (a justification for the distances used for comparing the calculated electric fields with the experimental LCPD images is given in Appendix B). This conclusion is further supported by LCPD measurements with CO-terminated tips, which are discussed in the following paragraph.

8.3 KPFM imaging with a CO-terminated tip

It has long been known that functionalizing a scanning probe tip with a single CO molecule can lead to enhanced resolution in STM images [10, 91]. In Chapter 5.3, we have shown that this is also the case for AFM imaging, where the tip functionalization with CO enables atomic-resolution imaging of single molecules. The combination of KPFM and controlled tip functionalization, on the other hand, has not been demonstrated until now. We show here that the CO tip termination also leads to dramatically enhanced resolution in KPFM imaging. In Fig. 8.3a-i, KPFM images recorded with the same CO tip as the one used in Fig. 8.1b-d are shown. The contrast in these images was found to strongly depend on the height at which they were recorded: At distances further away from the molecule, the LCPD images recorded with the CO tip resemble those recorded with the Cu tip (Fig. 8.3a,b). However, as the tip–sample distance was decreased, a more pronounced intramolecular contrast gradually evolved (Fig. 8.3c-h). In Fig. 8.3i, a high-resolution LCPD image for the closest investigated tip–sample distance is shown. Pronounced features with greater values of V^* are observed above the outermost C_6 rings and in the vicinity of the four outer N atoms, as well as a distinct asymmetry between the five-membered C_4N rings in the H-lobes and the N-lobes. These features in the LCPD image are qualitatively well reproduced in the calculated electric field distribution in a plane above the free naphthalocyanine molecule (Fig. 8.3j). This further supports our interpretation that the submolecular resolution of our LCPD images reflects the distribution of charge within the molecule.

The picture underlying this interpretation is in fact very intuitive: when the naphthalocyanine molecule is placed between the tip and the substrate,

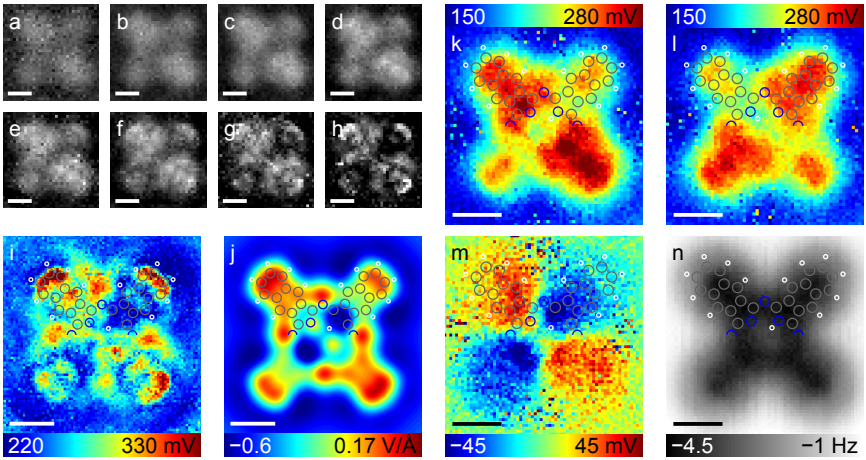

Fig. 8.3 Enhanced KPFM resolution with CO-functionalized tips. **a**-**h**, LCPD images of naphthalocyanine on NaCl(2ML)/Cu(111). The images were recorded with a CO-terminated tip on a 40×40 lateral grid at constant height, at different distances decreasing from **a** to **h**: $z = 2.9$, 2.7, 2.5, 2.3, 2.2, 2.1, 2.0, and 1.9 Å from the STM set point ($I = 2$ pA, $V = 0.2$ V) over the substrate ($A = 0.3$ Å). The color scale ranges from 240 mV (black) to 340 mV (white). **i**, LCPD image recorded with the same tip and imaging parameters as in **h**, but on a 92×92 lateral grid. **j**, DFT-calculated z-component of the electric field above a free naphthalocyanine molecule at a distance $d = 3.0$ Å from the molecular plane. **k**,**l**, LCPD images recorded with a different CO tip on a 70×70 lateral grid, before (**k**) and after (**l**) switching the tautomerization state of the imaged naphthalocyanine ($z = 2.0$ Å, $A = 0.3$ Å). **m**, Difference image obtained by subtracting **l** from **k**. **n**, Δf^* image extracted from the same data set as **k**. The DFT-calculated atomic positions are overlaid in the upper halves of **i**-**n**. Carbon, hydrogen, and nitrogen atoms are colored in gray, white, and blue, respectively. Scale bars: 5 Å.

a locally varying contribution to the electric field arises due to the inhomogeneous charge distribution within the molecule. Compensating the total electric field during the KPFM measurement then results in a variation of V^* that reflects the intramolecular charge distribution (longer-ranging contributions to the electrostatic interaction between the tip and the sample will only give an additional background that does not vary on the submolecular scale). We attribute the high resolution in our KPFM images to the

close tip–sample distances and the small oscillation amplitudes ($< 0.5\,\text{Å}$) used in our experiments. These conditions will both enhance the sensitivity to the short-ranging field generated by charge variation on the submolecular scale. Additional effects that could be imagined to affect the KPFM contrast include possible relaxations of the tip or the probed molecule, a finite polarizability of the tip, and a polarization of the probed molecule under application of an electric field [106] or due to chemical interactions [108]. However, as we show below, we have found that the measured KPFM signal appears to be completely independent of the current and frequency shift signals (a bending of the tip molecule, for example, should also affect the tunneling current). Together with the fact that the calculated electric field is already sufficient for a good qualitative description of our images, this leads us to the conclusion that the distribution of charge within the naphthalocyanine molecule (and the electric field generated thereby) is primarily responsible for the observed submolecular KPFM contrast.

8.3.1 Additional KPFM data set

In Fig. 8.3k-n, data from another KPFM measurement of naphthalocyanine are shown, before and after switching the tautomerization state of the molecule. The images were recorded on a different molecule and with a different CO tip than those shown in Fig. 8.3a-i. Therefore, the z distances cannot be directly compared. However, the lower resolution in both the LCPD images (Fig. 8.3k,l) and the corresponding Δf^* images (Fig. 8.3n, compare Fig. 8.4f) indicate a greater tip–sample distance than in Fig. 8.3i. In the LCPD images of both tautomerization states, we observe an asymmetry between the upper left lobe and the lower right lobe of the molecule, which is not expected from the symmetry of the molecule. Because this feature did not switch with the tautomerization state of the molecule, it can be attributed to a background slope in the LCPD of the substrate or an asymmetry of the tip. A similar feature can be seen in the LCPD image in Fig. 8.3i, where the upper right lobe appears more pronounced than the lower left lobe. The LCPD difference image obtained by subtracting the LCPD images before and after tautomerization switching is shown in Fig. 8.3m. It closely resembles the difference image from the measurement with the metal tip (Fig. 8.2d). This is in agreement with the calculated field asymmetry, which has the same simple quadrupole-like appearance

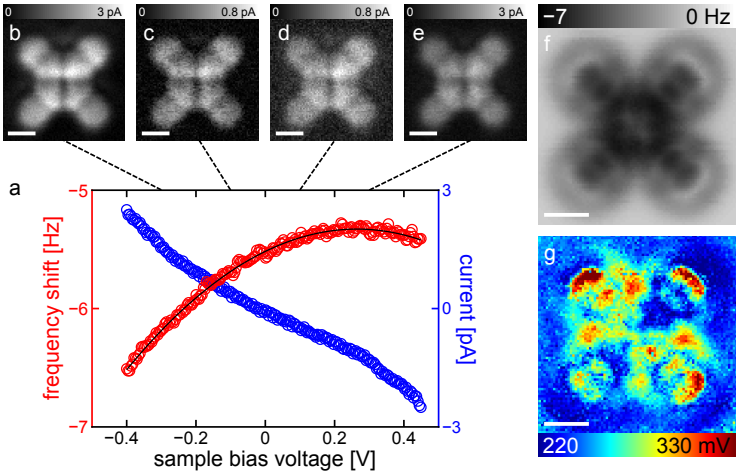

Fig. 8.4 Current and frequency shift measured simultaneously with the LCPD. **a**, Single $\Delta f(V)$ (red) and $I(V)$ (blue) spectrum from the LCPD map of Fig. 8.3i, recorded above the center of the molecule. **b-e**, Constant-height current images extracted from the 92×92 individual spectra for four different voltages ($V = -0.3$, -0.1, 0.1, and 0.3 V). **f**, Image of the frequency shift Δf^* at compensated LCPD, extracted from the same measurement. **g**, The LCPD image resembles neither the current images nor the Δf^* image. Scale bars: 5 Å.

even for closer distances, where the calculated electric field already shows pronounced submolecular variations (see Appendix B). This shows that in addition to the enhanced intramolecular resolution of Fig. 8.3i, the CO tip is also still sensitive to the extended charge asymmetry between the different lobes measured with the metal tip, which corroborates that the same mechanism is responsible for the contrast in the LCPD images with metal tips and CO tips. Furthermore, it supports the assumption that the closer tip–sample distance is the main reason for the enhanced resolution in the CO-tip KPFM images.

8.3.2 Independence of the KPFM signal

Because the presented KPFM technique is highly sensitive, one could suspect that it is also very susceptible to perturbations, for example by the tunneling

current or short-range chemical interactions. Therefore, it is important to show that the LCPD represents an independent channel of information and that there is no crosstalk between the different imaging signals. To prove that the LCPD is independent of the current and frequency shift, we show in Fig. 8.4 the current recorded for different voltages (Fig. 8.4a-e) and the frequency shift Δf^* at compensated LCPD (Fig. 8.4f) measured simultaneously with the LCPD image of Fig. 8.3i. Neither the current images nor the Δf^* image resemble the LCPD image, which effectively proves that the LCPD data is independent of these other channels. In all KPFM measurements presented in this chapter, we did not observe any deviations of the $\Delta f(V)$ spectra from the parabolic shape. Furthermore, we did not observe a significant voltage dependence of the contrast in constant-voltage Δf images extracted from the same data set. This implies that the short-range chemical interaction responsible for the atomic resolution in the AFM images showed no measurable voltage dependence, which again underlines the independence of the AFM and KPFM signal. The same analysis was performed for the LCPD images recorded with the metal tip (Fig. 2b,c), and we come to the same conclusions.

These results show that LCPD images of a single molecule represent an important additional channel of information complementary to STM and AFM images. The contrast in these LCPD images is generated by the inhomogeneous distribution of charge, yielding valuable insights into the intramolecular charge distribution.

CHAPTER 9

Summary

In this thesis, we have shown that the electronic and structural properties of single molecules on surfaces can be revealed in unprecedented detail by a combination of low-temperature STM and AFM. In particular, we have shown in Chapter 5 that the chemical structures of organic molecules can be imaged with AFM if the microscope tip is functionalized with a suitable atomic or molecular termination [121]. For the CO tip termination, with which we obtained the highest resolution, the mechanism responsible for the atomic contrast was identified as Pauli repulsion caused by the overlap of the electron densities of the CO and the imaged molecule [144]. The images therefore show the regions of high total electron density within the molecule, revealing details about the positions of atoms, bonds, and ring structures. Apart from constant-height AFM imaging, we have also developed a method to measure the complete three-dimensional short-range force field above a molecule with atomic resolution [140]. With this force mapping method, the possibility of imaging nonplanar molecules and measuring atomically resolved molecular topographies was demonstrated. This enables precise measurements of the adsorption geometries of single molecular adsorbates and in the future could potentially also lead to molecular imaging with chemical sensitivity [31, 183].

In Chapter 6 and 7, we have successfully applied our method of atomically resolved molecular imaging with AFM to determine the unknown structures of a switchable metal-molecule complex and a natural product from the deep

sea. In Chapter 6, we showed that the reversible bond formation between a Au atom and a PTCDA molecule can be used as a reliable molecular switch [143]. The combination of the information about the electronic structure from STM and DFT data and the information about the atomic geometry from AFM imaging enabled the identification of a new mechanism of bond formation as the origin of the high reliability of bond switching in this system. In Chapter 7, we have shown that atomic-resolution imaging with AFM can aid in the structure elucidation of an unknown molecule for which conventional methods were only able to identify four equally plausible molecular structures [139]. By a combination of atomic-resolution AFM imaging and DFT calculations, we were able to confirm this initial assignment and unambiguously identify the correct structure as cephalandole A. These results show that AFM imaging can provide valuable insights into unknown atomic structures of single molecules or molecular complexes. In the future, extending our method towards imaging of nonplanar adsorbates and towards imaging with chemical sensitivity could make it suitable for structure determination of an even wider class of bioactive compounds or functional molecular complexes.

The other main topic of this thesis was the imaging of charges with AFM and its offspring KPFM. In Chapter 4, we have shown that neutral and negatively charged Au atoms on an ultrathin insulating NaCl film can be distinguished by AFM imaging, due to a stronger electrostatic interaction of the charged adatoms with the AFM tip [110]. With KPFM, it was even possible to distinguish the charge states of negative, neutral, and positive metal adatoms. In Chapter 8, we have combined the charge sensitivity of KPFM with the high resolution of our force mapping method to image for the first time the charge distribution within a single molecule [150]. We showed that the molecule naphthalocyanine exhibits a pronounced charge asymmetry that manifests itself in submolecularly resolved KPFM images. By comparison with DFT calculations, we were able to identify the electric field generated by the inhomogeneous charge distribution within the molecule as the source of contrast in these images. Our method therefore opens up the possibility of directly imaging the charge distribution within single-molecule charge-transfer complexes, which hold promise for future applications such as solar photoconversion or energy storage [184, 185]. Furthermore, it could lead to new fundamental insights into single-molecule switching and bond formation, processes that are usually accompanied by

an intra- or intermolecular redistribution of charge [13, 26, 143, 186–188].

In conclusion, our investigations show that STM, AFM, and KPFM yield complementary images of single molecules, showing the molecular frontier orbitals, the chemical structure, and the electric field generated by the total charge within the molecule. The combination of these different channels of information will improve our understanding of atomic-scale processes in molecular systems on surfaces and could eventually bring us one step closer to the goal of single-molecule functional devices.

APPENDIX A

Definition of the tip–sample distance in Chapter 4

In Chapter 4, absolute values of the tip–sample distance were used, which were defined with respect to the point of mechanical contact of the tip with the NaCl(2ML)/Cu(111) substrate (see Fig. 4.2a). Here we show how this distance was experimentally determined. We denote by d the absolute tip–sample distance and by z the distance to the STM set point ($I_0 = 2\,\mathrm{pA}$, $V_0 = 0.05\,\mathrm{V}$) over the substrate. First, the STM tip was positioned over the NaCl surface, at the position indicated by the red circle in Fig. A.1a. After the feedback loop was opened, the tip was repeatedly approached towards the sample, increasing the distance of approach carefully step by step. At a certain distance of approach ($z_0 \approx -5\,\text{Å}$ from the tunneling set point), a sudden drop of the tunneling current occurred (Fig. A.1b). The subsequent STM image (Fig. A.1c) reveals that both the sample surface and the STM tip have been slightly modified by the approach of the tip. A closeup STM image of the approach location shows that a single Cl vacancy has been created (Fig. A.1d) [92]. Repeated measurements showed little variation in the distance where the discontinuity in the tunneling current occurred. We therefore interpret the point of the sudden drop of the tunneling current in Fig. A.1b as the point of mechanical contact between the tip and the sample surface and assign the absolute distance value $d_0 = 5.0\,\text{Å}$ to the STM set point. All values of the tip–sample distance in Chapter 4 are given with respect to this reference. To obtain the distance $d = d_0 + z$ corresponding to an arbitrary STM set point (I, V), we used the approximative expression

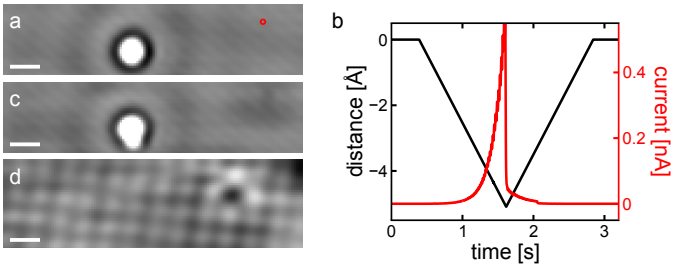

Fig. A.1 Determination of the absolute tip height. **a**, Constant-current STM image ($I = 2\,\mathrm{pA}$, $V = 50\,\mathrm{mV}$) showing a single Au^- adatom on NaCl(2ML)/Cu(111). **b**, Distance from the STM set point and tunneling current during the approach of the tip at the position indicated by the red circle in **a**. A sudden drop in the tunneling current at $z \approx -5\,\text{Å}$ indicated contact with the surface. **c**, The subsequent STM image reveals a slight modification of the NaCl surface at the position of the previous approach of the STM tip. The tip is modified, too, as can be seen from the altered appearance of the Au^-. **d**, From the closeup STM image ($I = 10\,\mathrm{pA}$, $V = 0.2\,\mathrm{V}$), the surface modification can be identified as a single Cl vacancy. Scale bars: 10 Å.

for the tunneling current (see Chapter 2.2.1):

$$I \propto V \mathrm{e}^{-2\kappa d} \tag{A.1a}$$

$$\Rightarrow \frac{I}{I_0} = \frac{V}{V_0} \mathrm{e}^{-2\kappa(d-d_0)} \tag{A.1b}$$

$$\Rightarrow d = d_0 + \frac{1}{2\kappa} \log\left(\frac{I_0 V}{I V_0}\right) . \tag{A.1c}$$

The decay constant κ, which depends on the height of the tunneling barrier, was taken from ref. [95], where a value of $\kappa = 0.93\,\text{Å}^{-1}$ was determined from $I(z)$ curves above NaCl(2ML)/Cu(111).

APPENDIX B

Additional AFM and DFT data of naphthalocyanine

In Chapter 8, we demonstrated KPFM imaging with submolecular resolution and attributed the contrast in the images to the charge distribution within the investigated naphthalocyanine molecule. Here we present additional data that support this conclusion. In particular, we show 3D force map data of naphthalocyanine, together with additional DFT calculations that include also the tip CO molecule. Next, we justify the distances used for comparing the experimental and DFT-calculated images and provide some technical details for the DFT calculations presented in Chapter 8.

B.1 3D force map and DFT-calculated interaction

In Fig. 8.1, we observed a transition between fourfold and twofold symmetry in the atomic-resolution AFM images of naphthalocyanine. To investigate this transition in more detail, we performed a 3D force map measurement using the technique described in Chapter 5.3. Individual $\Delta f(z)$ spectra were measured with a CO-terminated tip on a lateral grid above the naphthalocyanine molecule and merged into a complete 3D Δf data set. In Fig. B.1a-i, constant-height AFM images extracted for different distances from this data set are shown. With increasing tip–sample distance, we observe a smooth transition from fourfold to twofold symmetry in the center region of the molecule, accompanied by a gradual loss of spatial resolution. In

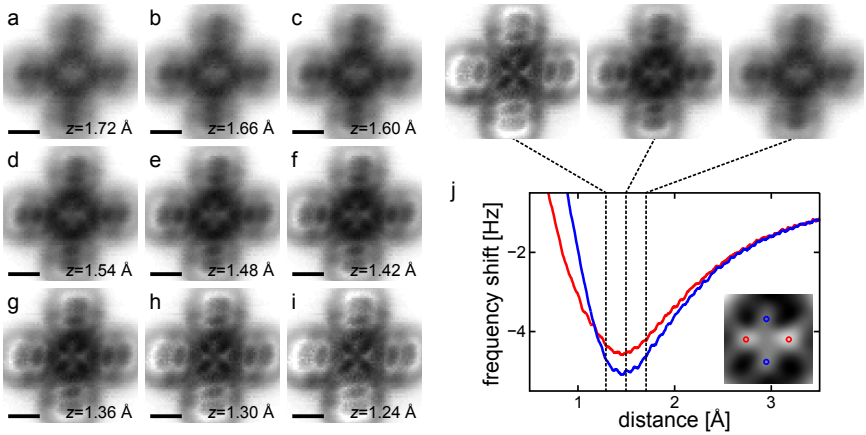

Fig. B.1 3D force mapping of naphthalocyanine on NaCl(2ML)/Cu(111). **a-i**, Constant-height Δf images extracted from a complete 3D Δf map measured with a CO-terminated tip on a 72×72 lateral grid above the molecule. The distance is indicated in each panel, measured from the STM set point over the substrate ($I = 3\,\mathrm{pA}$, $V = 0.2\,\mathrm{V}$). Scale bars: 5 Å. **j**, $\Delta f(z)$ spectra measured above the inner N sites with (blue) and without (red) hydrogen. The curves are an average of the two corresponding equivalent sites indicated in the inset. The distances of three constant-height Δf images are indicated by dashed lines.

Fig. B.1j, $\Delta f(z)$ spectra extracted from the same data set at positions close to the inner nitrogen sites (see inset) are shown. A characteristic crossover is found at a vertical distance of $z \approx 1.1\,\text{Å}$, where the contrast between the two sites is reversed. This crossover could not be observed in the AFM images, because the closest distance for which complete constant-height images could be extracted ($z = 1.24\,\text{Å}$) is already above the crossover point.

In Fig. 8.1, it was shown that the transition between fourfold and twofold symmetry is qualitatively reproduced in cuts through the DFT-calculated electron density of the free molecule. However, the vertical distance between the appearance of twofold and fourfold symmetry did not agree with the experiment (0.3 Å in the experiment versus 1.0 Å in the calculations). A more accurate, but computationally more expensive approach to simulate the AFM images is to 'scan' a CO molecule over the probed molecule and calculate the distance-dependent interaction energy for each lateral position

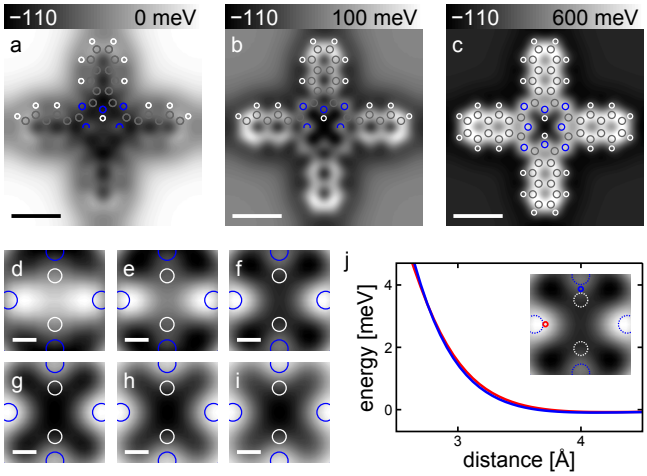

Fig. B.2 DFT-calculated CO–naphthalocyanine interaction energy. **a-c**, Calculated maps of the interaction energy for different intermolecular distances (CO carbon atom to the naphthalocyanine molecular plane) $d = 4.2$ Å (**a**), $d = 3.8$ Å (**b**), and $d = 3.4$ Å (**c**). **d-i**, Closeups of the center region of the molecule for $d = 4.4$, 4.2, 4.0, 3.8, 3.6, and 3.4 Å, decreasing from **d** to **i**. **j**, Distance dependence of the interaction energy at positions close to the inner nitrogen sites with (blue) and without (red) hydrogen, as indicated in the inset. The atomic positions are overlaid in **d-i** and in the upper halves of **a-c**. Carbon, hydrogen, and nitrogen atoms are colored in gray, white, and blue, respectively. Scale bars: 5 Å in **a-c** and 1 Å in **d-i**.

(see Chapter 5.4). The result of such a simulation is shown in Fig. B.2. Again, we find a gradual transition between fourfold and twofold symmetry, but over a distance range that agrees much better with the experiment.

B.2 Comparison between experiment and theory

In the following, we motivate the vertical distances at which the electric field above the molecule was compared to the LCPD images in Fig. 8.2d,e and Fig. 8.3i,j. First, we treat the case of the KPFM measurement with a metal-terminated tip (Fig. 8.2). For such a tip, we have found in Ap-

pendix A that an STM tunneling set point of $I_0 = 2\,\mathrm{pA}$, $V_0 = 0.05\,\mathrm{V}$ above NaCl(2ML)/Cu(111) corresponds to a tip–NaCl distance of about $d_0 = 5.0\,\text{Å}$. The LCPD images shown in Fig. 8.2b,c were recorded at a distance of $z = 1.0\,\text{Å}$ with respect to an STM set point of $I_1 = 3.5\,\mathrm{pA}$, $V_1 = 0.2\,\mathrm{V}$ above the substrate, which then corresponds to a tip–NaCl distance of (Eq. A.1)

$$d_1 = d_0 - \frac{1}{2\kappa}\log\left(\frac{I_1 V_0}{I_0 V_1}\right) + z \approx 6.5\,\text{Å}\ ,$$

where the exponential decay constant $\kappa = 0.93\,\text{Å}^{-1}$ for two monolayers of NaCl on Cu(111) was used [95]. For naphthalocyanine, a planar molecule containing large aromatic groups physisorbed on NaCl, the van der Waals radius of carbon, $r_{\mathrm{C,vdW}} = 1.7\,\text{Å}$, can be expected to yield a good approximation for the adsorption height above the upper boundary surface of the NaCl topmost layer. Using this approximation, we finally arrive at an estimate of the tip–molecule distance in the experiment of $d_{\mathrm{exp}} \approx 4.8\,\text{Å}$, which is close to the value $d = 5.0\text{Å}$, at which the calculated electric field was compared to the measurement in Fig. 8.2. There are several approximations involved in this estimate of d_{exp}, but we believe it is safe to assume that it is accurate at least within $\pm 1\,\text{Å}$. In Fig. B.3a-d, the calculated asymmetry of the electric field is shown for different distances between $d = 3.0\,\text{Å}$ and $d = 6.0\,\text{Å}$. The fact that the appearance of the field asymmetry changes only slightly with distance proves the validity of the qualitative comparison between the KPFM images and the electric field in Fig. 8.2.

Next, we treat the case of the CO-terminated tip, which was used for the measurement shown in Fig. 8.3i and Fig. 8.4g. In this case, to estimate the tip–molecule distance, we can use the fact that atomic resolution in AFM can only be achieved in a very narrow vertical distance range (see Chapter 5). By comparing the appearance of the Δf^* image recorded simultaneously with the KPFM measurement (Fig. 8.4f) to the distance dependence of the AFM images shown in Fig. B.1, we conclude that the LCPD map shown in Fig. 8.3i and Fig. 8.4g was measured at a distance close to the minimum in the $\Delta f(z)$ curve. From the DFT calculations shown in Fig. B.2, we know that in the calculated CO-naphthalocyanine interaction energy, the minimum occurs at a distance of about $d_{\mathrm{C-mol}} = 4.2\,\text{Å}$ from the CO carbon atom to the naphthalocyanine molecular plane. From a previous

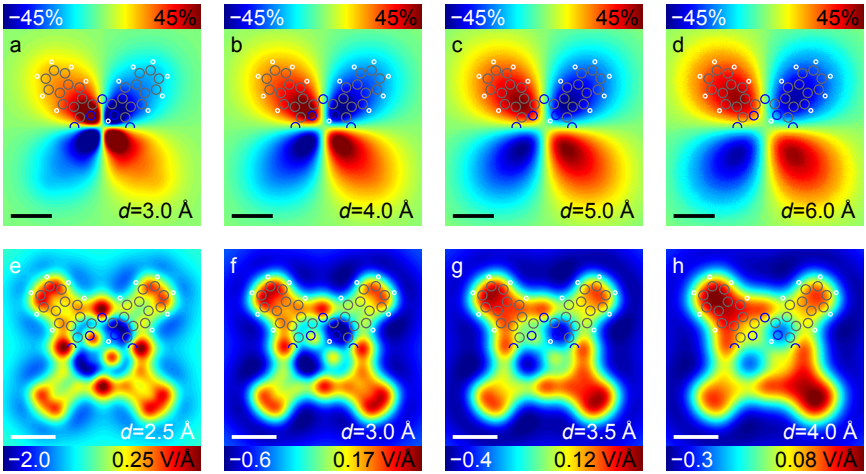

Fig. B.3 Distance dependence of the electric field above naphthalocyanine. **a-d** Normalized asymmetry A_E (see Chapter 8 for the definition of A_E) of the DFT-calculated z-component of the electric field above a free naphthalocyanine molecule, at different distances d from the molecular plane. **e-h** DFT-calculated z-component of the electric field, at different distances from the molecular plane. The atomic positions are overlaid in the upper halves of all panels. Carbon, hydrogen, and nitrogen atoms are colored in gray, white, and blue, respectively. Scale bars: 5 Å.

DFT study it is known that the minimum in Δf occurs about 0.9 Å further away, at $d_{\mathrm{C\text{–}mol}} = 5.1$ Å [144]. Taking into account the C–O bond length of 1.1 Å and using the covalent radius of oxygen, $r_{\mathrm{O,cov}} = 0.7$ Å, as an estimate of the extension of the electron cloud surrounding the last tip atom, we finally arrive at an estimated tip–molecule distance in the experiment of $d_{\mathrm{exp}} = 3.3$ Å, which is in good agreement with the distance $d = 3.0$ Å, for which we have found the best agreement between the calculated electric field distribution and the KPFM experimental data. Although we have a better estimate of the tip height for the CO tip than for the metal tip, again, there are several approximations involved. In Fig. B.3e-h, the calculated electric field distribution above the molecule is shown for different distances between 2.5 Å and 4.0 Å, to demonstrate that the qualitative features we observe in the experimental KPFM images are present within a certain

range of distances. The preceding discussion also shows that the closer tip–sample distance accessible with the CO tip termination is sufficient to explain the enhanced resolution in KPFM imaging with CO tips compared to metal tips.

B.3 Technical details of the DFT calculations

The DFT calculations in Chapter 8 and in this appendix were carried out for a free naphthalocyanine molecule, using the highly optimized plane-wave code CPMD [145]. The Perdew-Burke-Ernzerhof exchange-correlation functional [146] was used with ab initio norm-conserving pseudopotentials [147] created according to the scheme of Trouiller and Martins [148]. In the pseudopotential method, the valence electrons are accurately described outside a certain core region ($\sim 0.6\,\text{Å}$ for C atoms), whereas the core electrons are eliminated within the frozen-core approximation. This approximation yields an excellent description of the total electron density at the distances shown in Fig. 8.1. The size of the unit cell in our calculations was $32\,\text{Å} \times 32\,\text{Å} \times 16\,\text{Å}$. The structural optimization was performed until the forces on all atoms were below $10^{-4}\,\text{eV/Å}$, and a cutoff energy of 2 keV was used for a single k point (Γ). The z-component of the electric field was obtained by differentiating the calculated electrostatic potential with respect to z.

Bibliography

[1] A. Aviram and M. A. Ratner, *Molecular rectifiers*, Chem. Phys. Lett. **29**, 277 (1974).

[2] C. Joachim, J. K. Gimzewski, R. R. Schlittler, and C. Chavy, *Electronic transparence of a single C_{60} molecule*, Phys Rev. Lett. **74**, 2102 (1995).

[3] N. Néel, J. Kröger, L. Limot, T. Frederiksen, M. Brandbyge, and R. Berndt, *Controlled contact to a C_{60} molecule*, Phys. Rev. Lett. **98**, 065502 (2007).

[4] F. Pump, R. Temirov, O. Neucheva, S. Soubatch, S. Tautz, M. Rohlfing, and G. Cuniberti, *Quantum transport through STM-lifted single PTCDA molecules*, Appl. Phys. A **93**, 335 (2008).

[5] L. Lafferentz, F. Ample, H. Yu, S. Hecht, C. Joachim, and L. Grill, *Conductance of a single conjugated polymer as a continuous function of its length*, Science **323**, 1193 (2009).

[6] B. C. Stipe, M. A. Rezaei, and W. Ho, *Single-molecule vibrational spectroscopy and microscopy*, Science **280**, 1732 (1998).

[7] X. H. Qiu, G. V. Nazin, and W. Ho, *Vibronic states in single molecule electron transport*, Phys. Rev. Lett. **92**, 206102 (2004).

[8] D. M. Eigler and E. K. Schweizer, *Positioning single atoms with a scanning tunneling microscope*, Nature **344**, 524 (1990).

[9] D. M. Eigler, C. P. Lutz, and W. E. Rudge, *An atomic switch realized with the scanning tunneling microscope*, Nature **352**, 600 (1991).

[10] H. J. Lee and W. Ho, *Single-bond formation and characterization with a scanning tunneling microscope*, Science **286**, 1719 (1999).

[11] S.-W. Hla, L. Bartels, G. Meyer, and K.-H. Rieder, *Inducing all steps of a chemical reaction with the scanning tunneling microscope tip: Towards single molecule engineering*, Phys. Rev. Lett. **85**, 2777 (2000).

[12] J. R. Hahn and W. Ho, *Oxidation of a single carbon monoxide molecule manipulated and induced with a scanning tunneling microscope*, Phys. Rev. Lett. **87**, 166102 (2001).

[13] J. Repp, G. Meyer, S. Paavilainen, F. E. Olsson, and M. Persson, *Imaging bond formation between a gold atom and pentacene on an insulating surface*, Science **312**, 1196 (2006).

[14] D. Wegner, R. Yamachika, X. Zhang, Y. Wang, T. Baruah, M. R. Pederson, B. M. Bartlett, J. R. Long, and M. F. Crommie, *Tuning molecule-mediated spin coupling in bottom-up-fabricated vanadium-tetracyanoethylene nanostructures*, Phys. Rev. Lett. **103**, 087205 (2009).

[15] A. J. Heinrich, C. P. Lutz, J. A. Gupta, and D. M. Eigler, *Molecule cascades*, Science **298**, 1381 (2002).

[16] G. V. Nazin, X. H. Qiu, and W. Ho, *Visualization and spectroscopy of a metal-molecule-metal bridge*, Science **302**, 77 (2003).

[17] J. Repp, G. Meyer, F. E. Olsson, and M. Persson, *Controlling the charge state of individual gold adatoms*, Science **305**, 493 (2004).

[18] X. H. Qiu, G. V. Nazin, and W. Ho, *Vibrationally resolved fluorescence excited with submolecular precision*, Science **299**, 542 (2003).

[19] S. W. Wu, N. Ogawa, and W. Ho, *Atomic-scale coupling of photons to single-molecule junctions*, Science **312**, 1362 (2006).

[20] C. Chen, P. Chu, C. A. Bobisch, D. L. Mills, and W. Ho, *Viewing the interior of a single molecule: Vibronically resolved photon imaging at submolecular resolution*, Phys. Rev. Lett. **105**, 217402 (2010).

[21] A. J. Heinrich, J. A. Gupta, C. P. Lutz, and D. M. Eigler, *Single-atom spin-flip spectroscopy*, Science **306**, 466 (2004).

[22] S. Loth, M. Etzkorn, C. P. Lutz, D. M. Eigler, and A. J. Heinrich, *Measurement of fast electron spin relaxation times with atomic resolution*, Science **329**, 1628 (2010).

[23] C. F. Hirjibehedin, C. P. Lutz, and A. J. Heinrich, *Spin coupling in engineered atomic structures*, Science **312**, 1021 (2006).

[24] S. Loth, S. Baumann, C. P. Lutz, D. M. Eigler, and A. J. Heinrich, *Bistability in atomic-scale antiferromagnets*, Science **335**, 196 (2012).

[25] J. Repp, G. Meyer, S. M. Stojković, A. Gourdon, and C. Joachim, *Molecules on insulating films: Scanning-tunneling microscopy imaging of individual molecular orbitals*, Phys. Rev. Lett. **94**, 026803 (2005).

[26] P. Liljeroth, I. Swart, S. Paavilainen, J. Repp, and G. Meyer, *Single-molecule synthesis and characterization of metal-ligand complexes by low-temperature STM*, Nano Lett. **10**, 2475 (2010).

[27] P. Liljeroth, J. Repp, and G. Meyer, *Current-induced hydrogen tautomerization and conductance switching of naphthalocyanine molecules*, Science **317**, 1203 (2007).

[28] T. R. Albrecht, P. Grütter, D. Horne, and D. Rugar, *Frequency modulation detection using high-Q cantilevers for enhanced force microscope sensitivity*, J. Appl. Phys. **69**, 668 (1991).

[29] F. J. Giessibl, *Atomic resolution of the silicon (111)-(7 × 7) surface by atomic force microscopy*, Science **267**, 68 (1995).

[30] M. Ashino, A. Schwarz, T. Behnke, and R. Wiesendanger, *Atomic-resolution dynamic force microscopy and spectroscopy of a single-walled carbon nanotube: Characterization of interatomic van der Waals forces*, Phys. Rev. Lett. **93**, 136101 (2004).

[31] Y. Sugimoto, P. Pou, M. Abe, P. Jelinek, R. Pérez, S. Morita, and O. Custance, *Chemical identification of individual surface atoms by atomic force microscopy*, Nature **446**, 64 (2007).

[32] Y. Sugimoto, M. Abe, S. Hirayama, N. Oyabu, O. Custance, and S. Morita, *Atom inlays performed at room temperature using atomic force microscopy*, Nature Mater. **4**, 156 (2005).

[33] Y. Sugimoto, P. Pou, O. Custance, P. Jelinek, M. Abe, R. Perez, and S. Morita, *Complex patterning by vertical interchange atom manipulation using atomic force microscopy*, Science **322**, 413 (2008).

[34] C. Loppacher, M. Guggisberg, O. Pfeiffer, E. Meyer, M. Bammerlin, R. Lüthi, R. Schlittler, J. K. Gimzewski, H. Tang, and C. Joachim, *Direct determination of the energy required to operate a single molecule switch*, Phys. Rev. Lett. **90**, 066107 (2003).

[35] M. Ternes, C. P. Lutz, C. F. Hirjibehedin, F. J. Giessibl, and A. J. Heinrich, *The force needed to move an atom on a surface*, Science **319**, 1066 (2008).

[36] U. Kaiser, A. Schwarz, and R. Wiesendanger, *Magnetic exchange force microscopy with atomic resolution*, Nature **446**, 522 (2007).

[37] F. J. Giessibl, *High-speed force sensor for force microscopy and profilometry utilizing a quartz tuning fork*, Appl. Phys. Lett. **73**, 3956 (1998).

[38] C. J. Chen, *Introduction to scanning tunneling microscopy* (Oxford University Press, 2008).

[39] E. Meyer, H. J. Hug, and R. Bennewitz, *Scanning probe microscopy: the lab on a tip* (Springer, 2003).

[40] B. Bhushan, ed., *Scanning probe microscopy in nanoscience and nanotechnology* (Springer, 2009).

[41] S. Morita, R. Wiesendanger, and E. Meyer, eds., *Noncontact atomic force microscopy* (Springer, 2002).

[42] S. Morita, F. J. Giessibl, and R. Wiesendanger, eds., *Noncontact atomic force microscopy, Volume 2* (Springer, 2009).

[43] S. Sadewasser and T. Glatzel, eds., *Kelvin probe force microscopy* (Springer, 2012).

[44] G. Binnig and H. Rohrer, *In touch with atoms*, Rev. Mod. Phys. **71**, S324 (1999).

[45] F. J. Giessibl, *Advances in atomic force microscopy*, Rev. Mod. Phys. **75**, 949 (2003).

[46] G. Binnig, H. Rohrer, C. Gerber, and E. Weibel, *Surface studies by scanning tunneling microscopy*, Phys. Rev. Lett. **49**, 57 (1982).

[47] G. Binnig, H. Rohrer, C. Gerber, and E. Weibel, *7 × 7 reconstruction on Si(111) resolved in real space*, Phys. Rev. Lett. **50**, 120 (1983).

[48] K. Takayanagi, Y. Tanishiro, M. Takahashi, and S. Takahashi, *Structural analysis of Si(111)-7 × 7 by UHV-transmission electron diffraction and microscopy*, J. Vac. Sci. Technol. A **3**, 1502 (1985).

[49] G. Binnig, C. F. Quate, and C. Gerber, *Atomic force microscope*, Phys. Rev. Lett. **56**, 930 (1986).

[50] G. Binnig, C. Gerber, E. Stoll, T. R. Albrecht, and C. F. Quate, *Atomic resolution with atomic force microscope*, Europhys. Lett. **3**, 1281 (1987).

[51] G. Meyer and N. M. Amer, *Optical-beam-deflection atomic force microscopy: The NaCl(001) surface*, Appl. Phys. Lett. **56**, 2100 (1990).

[52] J. B. Pethica and W. C. Oliver, *Tip surface interactions in STM and AFM*, Phys. Scr. **T19**, 61 (1987).

[53] S. Kitamura and M. Iwatsuki, *Observation of 7×7 reconstructed structure on the silicon (111) surface using ultrahigh vacuum noncontact atomic force microscopy*, Jpn. J. Appl. Phys. **34**, L145 (1995).

[54] J. E. Stern, B. D. Terris, H. J. Mamin, and D. Rugar, *Deposition and imaging of localized charge on insulator surfaces using a force microscope*, Appl. Phys. Lett. **53**, 2717 (1988).

[55] M. Nonnenmacher, M. P. O'Boyle, and H. K. Wickramasinghe, *Kelvin probe force microscopy*, Appl. Phys. Lett. **58**, 2921 (1991).

[56] J. R. Matey and J. Blanc, *Scanning capacitance microscopy*, J. Appl. Phys. **57**, 1437 (1985).

[57] Y. Martin and H. K. Wickramasinghe, *Magnetic imaging by "force microscopy" with 1000 Å resolution*, Appl. Phys. Lett. **50**, 1455 (1987).

[58] R. Wiesendanger, H.-J. Güntherodt, G. Güntherodt, R. J. Gambino, and R. Ruf, *Observation of vacuum tunneling of spin-polarized electrons with the scanning tunneling microscope*, Phys. Rev. Lett. **65**, 247 (1990).

[59] I. Giaever, *Energy gap in superconductors measured by electron tunneling*, Phys. Rev. Lett. **5**, 147 (1960).

[60] G. Gamow, *Zur Quantentheorie des Atomkerns*, Z. Phys. A: Hadrons Nucl. **51**, 204 (1928).

[61] G. Binnig and D. P. E. Smith, *Single-tube three-dimensional scanner for scanning tunneling microscopy*, Rev. Sci. Instrum. **57**, 1688 (1986).

[62] C. Cohen-Tannoudji, B. Diu, and F. Laloe, *Quantum mechanics* (Wiley Interscience, 1977).

[63] J. Bardeen, *Tunneling from a many-particle point of view*, Phys. Rev. Lett. **6**, 57 (1961).

[64] J. Tersoff and D. R. Hamann, *Theory of the scanning tunneling microscope*, Phys. Rev. B **31**, 805 (1985).

[65] O. Wolter, T. Bayer, and J. Greschner, *Micromachined silicon sensors for scanning force microscopy*, J. Vac. Sci. Technol. B **9**, 1353 (1991).

[66] G. Meyer and N. M. Amer, *Novel optical approach to atomic force microscopy*, Appl. Phys. Lett. **53**, 2400 (1988).

[67] P. Günther, U. C. Fischer, and K. Dransfeld, *Scanning near-field acoustic microscopy*, Appl. Phys. B **48**, 89 (1989).

[68] Y. Martin, C. C. Williams, and H. K. Wickramasinghe, *Atomic force microsope – force mapping and profiling on a sub 100-Å scale*, J. Appl. Phys. **61**, 4723 (1987).

[69] F. J. Giessibl, *Forces and frequency shifts in atomic-resolution dynamic-force microscopy*, Phys. Rev. B **56**, 16010 (1997).

[70] B. Gotsmann, B. Anczykowski, C. Seidel, and H. Fuchs, *Determination of tip–sample interaction forces from measured dynamic force spectroscopy curves*, Appl. Surf. Sci. **140**, 314 (1999).

[71] U. Dürig, *Relations between interaction force and frequency shift in large-amplitude dynamic force microscopy*, Appl. Phys. Lett. **75**, 433 (1999).

[72] U. Dürig, *Interaction sensing in dynamic force microscopy*, New J. Phys. **2**, 5.1 (2000).

[73] F. J. Giessibl, *A direct method to calculate tip–sample forces from frequency shifts in frequency-modulation atomic force microscopy*, Appl. Phys. Lett. **78**, 123 (2001).

[74] J. E. Sader and S. P. Jarvis, *Accurate formulas for interaction force and energy in frequency modulation force spectroscopy*, Appl. Phys. Lett. **84**, 1801 (2004).

[75] J. E. Sader, T. Uchihashi, M. J. Higgins, A. Farrell, Y. Nakayama, and S. P. Jarvis, *Quantitative force measurements using frequency modulation atomic force microscopy—theoretical foundations*, Nanotechnology **16**, S94 (2005).

[76] H. C. Hamaker, *The London-van der Waals attraction between spherical particles*, Physica **4**, 1058 (1937).

[77] L. Olsson, N. Lin, V. Yakimov, and R. Erlandsson, *A method for in situ characterization of tip shape in ac-mode atomic force microscopy using electrostatic interaction*, J. Appl. Phys. **84**, 4060 (1998).

[78] F. J. Giessibl, *Theory for an electrostatic imaging mechanism allowing atomic resolution of ionic crystals by atomic force microscopy*, Phys. Rev. B **45**, 13815 (1992).

[79] J. E. Jones, *On the determination of molecular fields.—II. From the equation of state of a gas*, Proc. R. Soc. A **106**, 463 (1924).

[80] Lord Kelvin, *Contact electricity of metals*, Phil. Mag. **46**, 82 (1898).

[81] G. Meyer, *A simple low-temperature ultrahigh-vacuum scanning tunneling microscope capable of atomic manipulation*, Rev. Sci. Instrum. **67**, 2960 (1996).

[82] F. J. Giessibl, *Atomic resolution on Si(111)-(7 × 7) by noncontact atomic force microscopy with a force sensor based on a quartz tuning fork*, Appl. Phys. Lett. **76**, 1470 (2000).

[83] K. Schaeffer, *Aufbau eines Tieftemperatur-Rastertunnelmikroskops*, Master's thesis, Freie Universität Berlin (1997).

[84] K. Besocke, *An easily operable scanning tunneling microscope*, Surf. Sci. **181**, 145 (1987).

[85] J. Frohn, J. F. Wolf, K. Besocke, and M. Teske, *Coarse tip distance adjustment and positioner for a scanning tunneling microscope*, Rev. Sci. Instrum. **60**, 1200 (1989).

[86] J. Rychen, T. Ihn, P. Studerus, A. Herrmann, and K. Ensslin, *A low-temperature dynamic mode scanning force microscope operated in high magnetic fields*, Rev. Sci. Instrum. **70**, 2765 (1999).

[87] M. Heyde, M. Sterrer, H.-P. Rust, and H.-J. Freund, *Atomic-resolution on MgO(001) by atomic force microscopy using a double quartz tuning fork sensor at low-temperature and ultrahigh vacuum*, Appl. Phys. Lett. **87**, 083104 (2005).

[88] R. Bennewitz, V. Barwich, M. Bammerlin, C. Loppacher, M. Guggisberg, A. Baratoff, E. Meyer, and H.-J. Güntherodt, *Ultrathin films of NaCl on Cu(111): A LEED and dynamic force microscopy study*, Surf. Sci. **438**, 289 (1999).

[89] J. Repp, G. Meyer, and K.-H. Rieder, *Snell's law for surface electrons: Refraction of an electron gas imaged in real space*, Phys. Rev. Lett. **92**, 036803 (2004).

[90] S.-I. Ishi, Y. Ohno, and B. Viswanathan, *An overview on the electronic and vibrational properties of adsorbed CO*, Surf. Sci. **161**, 349 (1985).

[91] L. Bartels, G. Meyer, and K.-H. Rieder, *Controlled vertical manipulation of single CO molecules with the scanning tunneling microscope: A route to chemical contrast*, Appl. Phys. Lett. **71**, 213 (1997).

[92] J. Repp, G. Meyer, S. Paavilainen, F. E. Olsson, and M. Persson, *Scanning tunneling spectroscopy of Cl vacancies in NaCl films: Strong electron-phonon coupling in double-barrier tunneling junctions*, Phys. Rev. Lett. **95**, 225503 (2005).

[93] J. Lagoute, K. Kanisawa, and S. Fölsch, *Manipulation and adsorption-site mapping of single pentacene molecules on Cu(111)*, Phys. Rev. B **70**, 245415 (2004).

[94] F. E. Olsson, S. Paavilainen, M. Persson, J. Repp, and G. Meyer, *Multiple charge states of Ag atoms on ultrathin NaCl films*, Phys. Rev. Lett. **98**, 176803 (2007).

[95] J. Repp, *Rastertunnelmikroskopie und -spektroskopie an Adsorbaten auf Metall- und Isolatoroberflächen*, Ph.D. thesis, Freie Universität Berlin (2002).

[96] M. Sterrer, T. Risse, U. M. Pozzoni, L. Giordano, M. Heyde, H.-P. Rust, G. Pacchioni, and H.-J. Freund, *Control of the charge state of metal atoms on thin MgO films*, Phys. Rev. Lett. **98**, 096107 (2007).

[97] C. Schönenberger and S. F. Alvarado, *Observation of single charge carriers by force microscopy*, Phys. Rev. Lett. **65**, 3162 (1990).

[98] L. J. Klein and C. C. Williams, *Single electron tunneling detected by electrostatic force*, Appl. Phys. Lett. **79**, 1828 (2001).

[99] M. T. Woodside and P. L. McEuen, *Scanned probe imaging of single-electron charge states in nanotube quantum dots*, Science **296**, 1098 (2002).

[100] R. Stomp, Y. Miyahara, S. Schaer, Q. Sun, H. Guo, P. Grutter, S. Studenikin, P. Poole, and A. Sachrajda, *Detection of single-electron charging in an individual InAs quantum dot by noncontact atomic-force microscopy*, Phys. Rev. Lett. **94**, 056802 (2005).

[101] E. Bussmann, N. Zheng, and C. C. Williams, *Single-electron manipulation to and from a SiO_2 surface by electrostatic force microscopy*, Appl. Phys. Lett. **86**, 163109 (2005).

[102] Y. Azuma, M. Kanehara, T. Teranishi, and Y. Majima, *Single electron on a nanodot in a double-barrier tunneling structure observed by noncontact atomic-force spectroscopy*, Phys. Rev. Lett. **96**, 016108 (2006).

[103] C. Sommerhalter, T. W. Matthes, T. Glatzel, A. Jäger-Waldau, and M. C. Lux-Steiner, *High-sensitivity quantitative Kelvin probe microscopy by noncontact ultra-high-vacuum atomic force microscopy*, Applied Physics Letters **75**, 286 (1999).

[104] C. Barth and C. R. Henry, *Surface double layer on (001) surfaces of alkali halide crystals: A scanning force microscopy study*, Phys. Rev. Lett. **98**, 136804 (2007).

[105] G. H. Enevoldsen, T. Glatzel, M. C. Christensen, J. V. Lauritsen, and F. Besenbacher, *Atomic scale Kelvin probe force microscopy studies of the surface potential variations on the TiO_2(110) surface*, Phys. Rev. Lett. **100**, 236104 (2008).

[106] F. Bocquet, L. Nony, C. Loppacher, and T. Glatzel, *Analytical approach to the local contact potential difference on (001) ionic surfaces: Implications for Kelvin probe force microscopy*, Phys. Rev. B **78**, 035410 (2008).

[107] M. Ikeda, N. Koide, L. Han, A. Sasahara, and H. Onishi, *Work function on dye-adsorbed TiO_2 surfaces measured by using a Kelvin probe force microscope*, J. Phys. Chem. C **112**, 6961 (2008).

[108] S. Sadewasser, P. Jelinek, C.-K. Fang, O. Custance, Y. Yamada, Y. Sugimoto, M. Abe, and S. Morita, *New insights on atomic-resolution frequency-modulation Kelvin-probe force-microscopy imaging of semiconductors*, Phys. Rev. Lett. **103**, 266103 (2009).

[109] S. Kawai, T. Glatzel, H.-J. Hug, and E. Meyer, *Atomic contact potential variations of Si(111)-7 × 7 analyzed by Kelvin probe force microscopy*, Nanotechnology **21**, 245704 (2010).

[110] L. Gross, F. Mohn, P. Liljeroth, J. Repp, F. J. Giessibl, and G. Meyer, *Measuring the charge state of an adatom with noncontact atomic force microscopy*, Science **324**, 1428 (2009).

[111] L. Nony, A. S. Foster, F. Bocquet, and C. Loppacher, *Understanding the atomic-scale contrast in Kelvin probe force microscopy*, Phys. Rev. Lett. **103**, 036802 (2009).

[112] R. Bennewitz, M. Bammerlin, M. Guggisberg, C. Loppacher, A. Baratoff, E. Meyer, and H.-J. Güntherodt, *Aspects of dynamic force microscopy on NaCl/Cu(111): Resolution, tip–sample interactions and cantilever oscillation characteristics*, Surf. Interface Anal. **27**, 462 (1999).

[113] K. Uchida, in *Nanoelectronics and information technology*, edited by R. Waser (Wiley VCH, 2003).

[114] L. Gross, N. Moll, F. Mohn, A. Curioni, G. Meyer, F. Hanke, and M. Persson, *High-resolution molecular orbital imaging using a p-wave STM tip*, Phys. Rev. Lett. **107**, 086101 (2011).

[115] R. Schmidt, C. Lazo, H. Hölscher, U. H. Pi, V. Caciuc, A. Schwarz, R. Wiesendanger, and S. Heinze, *Probing the magnetic exchange forces of iron on the atomic scale*, Nano Lett. **9**, 200 (2009).

[116] R. Schmidt, C. Lazo, U. Kaiser, A. Schwarz, S. Heinze, and R. Wiesendanger, *Quantitative measurement of the magnetic exchange interaction across a vacuum gap*, Phys. Rev. Lett. **106**, 257202 (2011).

[117] M. Ashino, D. Obergfell, M. Haluška, S. Yang, A. N. Khlobystov, S. Roth, and R. Wiesendanger, *Atomically resolved mechanical response of individual metallofullerene molecules confined inside carbon nanotubes*, Nature Nanotech. **3**, 337 (2008).

[118] A. Yazdani, D. M. Eigler, and N. D. Lang, *Off-resonance conduction through atomic wires*, Science **272**, 1921 (1996).

[119] N. Oyabu, P. Pou, Y. Sugimoto, P. Jelinek, M. Abe, S. Morita, R. Pérez, and O. Custance, *Single atomic contact adhesion and dissipation in dynamic force microscopy*, Phys. Rev. Lett. **96**, 106101 (2006).

[120] M. Ondráček, P. Pou, V. Rozsíval, C. González, P. Jelínek, and R. Pérez, *Forces and currents in carbon nanostructures: Are we imaging atoms?*, Phys. Rev. Lett. **106**, 176101 (2011).

[121] L. Gross, F. Mohn, N. Moll, P. Liljeroth, and G. Meyer, *The chemical structure of a molecule resolved by atomic force microscopy*, Science **325**, 1110 (2009).

[122] J. Lagoute and S. Fölsch, *Interaction of single pentacene molecules with monatomic Cu/Cu(111) quantum wires*, J. Vac. Sci. Technol. B **23**, 1726 (2005).

[123] K. Müller, A. Kara, T. K. Kim, R. Bertschinger, A. Scheybal, J. Osterwalder, and T. A. Jung, *Multimorphism in molecular monolayers: Pentacene on Cu(110)*, Phys. Rev. B **79**, 245421 (2009).

[124] J. A. Smerdon, M. Bode, N. P. Guisinger, and J. R. Guest, *Monolayer and bilayer pentacene on Cu(111)*, Phys. Rev. B **84**, 165436 (2011).

[125] D. W. Boukhalov, X. Feng, and K. Müllen, *First-principles modeling of the polycyclic aromatic hydrocarbons reduction*, J. Phys. Chem. C **115**, 16001 (2011).

[126] P. Atkins and R. Friedman, *Molecular quantum mechanics* (Oxford University Press, 2005).

[127] J. A. Larsson, S. D. Elliott, J. C. Greer, J. Repp, G. Meyer, and R. Allenspach, *Orientation of individual C_{60} molecules adsorbed on Cu(111): Low-temperature scanning tunneling microscopy and density functional calculations*, Phys. Rev. B **77**, 115434 (2008).

[128] S.-H. Chang, S. Kuck, J. Brede, L. Lichtenstein, G. Hoffmann, and R. Wiesendanger, *Symmetry reduction of metal phthalocyanines on metals*, Phys. Rev. B **78**, 233409 (2008).

[129] R. Cuadrado, J. I. Cerdá, Y. Wang, G. Xin, R. Berndt, and H. Tang, *CoPc adsorption on Cu(111): Origin of the C4 to C2 symmetry reduction*, J. Chem. Phys. **133**, 154701 (2010).

[130] A. Sperl, J. Kröger, and R. Berndt, *Controlled metalation of a single adsorbed phthalocyanine*, Angew. Chem. Int. Ed. **50**, 5294 (2011).

[131] M. A. Lantz, H. J. Hug, R. Hoffmann, P. J. A. van Schendel, P. Kappenberger, S. Martin, A. Baratoff, and H.-J. Güntherodt, *Quantitative measurement of short-range chemical bonding forces*, Science **291**, 2580 (2001).

[132] M. A. Lantz, R. Hoffmann, A. S. Foster, A. Baratoff, H. J. Hug, H. R. Hidber, and H.-J. Güntherodt, *Site-specific force-distance characteristics on NaCl(001): Measurements versus atomistic simulations*, Phys. Rev. B **74**, 245426 (2006).

[133] H. Hölscher, S. M. Langkat, A. Schwarz, and R. Wiesendanger, *Measurement of three-dimensional force fields with atomic resolution using dynamic force spectroscopy*, Appl. Phys. Lett. **81**, 4428 (2002).

[134] M. Heyde, G. H. Simon, H.-P. Rust, and H.-J. Freund, *Probing adsorption sites on thin oxide films by dynamic force microscopy*, Appl. Phys. Lett. **89**, 263107 (2006).

[135] M. Abe, Y. Sugimoto, T. Namikawa, K. Morita, N. Oyabu, and S. Morita, *Drift-compensated data acquisition performed at room temperature with frequency modulation atomic force microscopy*, Appl. Phys. Lett. **90**, 203103 (2007).

[136] K. Ruschmeier, A. Schirmeisen, and R. Hoffmann, *Atomic-scale force-vector fields*, Phys. Rev. Lett. **101**, 156102 (2008).

[137] B. J. Albers, T. C. Schwendemann, M. Z. Baykara, N. Pilet, M. Liebmann, E. I. Altman, and U. D. Schwarz, *Three-dimensional imaging of short-range chemical forces with picometre resolution*, Nature Nanotech. **4**, 307 (2009).

[138] S. Kawai, T. Glatzel, S. Koch, A. Baratoff, and E. Meyer, *Interaction-induced atomic displacements revealed by drift-corrected dynamic force spectroscopy*, Phys. Rev. B **83**, 035421 (2011).

[139] L. Gross, F. Mohn, N. Moll, G. Meyer, R. Ebel, W. M. Abdel-Mageed, and M. Jaspars, *Organic structure determination using atomic-resolution scanning probe microscopy*, Nature Chem. **2**, 821 (2010).

[140] F. Mohn, L. Gross, and G. Meyer, *Measuring the short-range force field above a single molecule with atomic resolution*, Appl. Phys. Lett. **99**, 053106 (2011).

[141] Z. Sun, M. P. Boneschanscher, I. Swart, D. Vanmaekelbergh, and P. Liljeroth, *Quantitative atomic force microscopy with carbon monoxide terminated tips*, Phys. Rev. Lett. **106**, 046104 (2011).

[142] L. Gross, F. Mohn, N. Moll, B. Schuler, and G. Meyer (2012), in preparation.

[143] F. Mohn, J. Repp, L. Gross, G. Meyer, M. S. Dyer, and M. Persson, *Reversible bond formation in a gold-atom–organic-molecule complex as a molecular switch*, Phys. Rev. Lett. **105**, 266102 (2010).

[144] N. Moll, L. Gross, F. Mohn, A. Curioni, and G. Meyer, *The mechanisms underlying the enhanced resolution of atomic force microscopy with functionalized tips*, New J. Phys. **12**, 125020 (2010).

[145] CPMD, v.3.15, copyright IBM Corp. 1990-2011, copyright MPI für Festkörperforschung Stuttgart 1997-2001.

[146] J. P. Perdew, K. Burke, and M. Ernzerhof, *Generalized gradient approximation made simple*, Phys. Rev. Lett. **77**, 3865 (1996).

[147] D. R. Hamann, *Generalized norm-conserving pseudopotentials*, Phys. Rev. B **40**, 2980 (1989).

[148] N. Troullier and J. L. Martins, *Efficient pseudopotentials for plane-wave calculations*, Phys. Rev. B **43**, 1993 (1991).

[149] S. Grimme, *Semiempirical GGA-type density functional constructed with a long-range dispersion correction*, J. Comput. Chem. **27**, 1787 (2006).

[150] F. Mohn, L. Gross, N. Moll, and G. Meyer, *Imaging the charge distribution within a single molecule*, Nature Nanotech. **7**, 227 (2012).

[151] C.-S. Guo, M. A. Van Hove, R.-Q. Zhang, and C. Minot, *Prospects for resolving chemical structure by atomic force microscopy: A first-principles study*, Langmuir **26**, 16271 (2010).

[152] M. J. Comstock, J. Cho, A. Kirakosian, and M. F. Crommie, *Manipulation of azobenzene molecules on Au(111) using scanning tunneling microscopy*, Phys. Rev. B **72**, 153414 (2005).

[153] B.-Y. Choi, S.-J. Kahng, S. Kim, H. Kim, H. W. Kim, Y. J. Song, J. Ihm, and Y. Kuk, *Conformational molecular switch of the azobenzene molecule: A scanning tunneling microscopy study*, Phys. Rev. Lett. **96**, 156106 (2006).

[154] J. Henzl, M. Mehlhorn, H. Gawronski, K.-H. Rieder, and K. Morgenstern, *Reversible cis-trans isomerization of a single azobenzene molecule*, Angew. Chem. Int. Ed. **45**, 603 (2006).

[155] M. J. Comstock, N. Levy, A. Kirakosian, J. Cho, F. Lauterwasser, J. H. Harvey, D. A. Strubbe, J. M. J. Fréchet, D. Trauner, S. G. Louie, and M. F. Crommie, *Reversible photomechanical switching of individual engineered molecules at a metallic surface*, Phys. Rev. Lett. **99**, 038301 (2007).

[156] C. Dri, M. V. Peters, J. Schwarz, S. Hecht, and L. Grill, *Spatial periodicity in molecular switching*, Nature Nanotech. **3**, 649 (2008).

[157] Y. Wang, J. Kröger, R. Berndt, and W. A. Hofer, *Pushing and pulling a Sn ion through an adsorbed phthalocyanine molecule*, J. Am. Chem. Soc. **131**, 3639 (2009).

[158] T. Choi, S. Bedwani, A. Rochefort, C.-Y. Chen, A. J. Epstein, and J. A. Gupta, *A single molecule Kondo switch: Multistability of tetracyanoethylene on Cu(111)*, Nano Lett. **10**, 4175 (2010).

[159] R. Ohmann, L. Vitali, and K. Kern, *Actuated transitory metal–ligand bond as tunable electromechanical switch*, Nano Lett. **10**, 2995 (2010).

[160] T. Kumagai, M. Kaizu, S. Hatta, H. Okuyama, T. Aruga, I. Hamada, and Y. Morikawa, *Direct observation of hydrogen-bond exchange within a single water dimer*, Phys. Rev. Lett. **100**, 166101 (2008).

[161] O. H. Pakarinen, J. M. Mativetsky, A. Gulans, M. J. Puska, A. S. Foster, and P. Grutter, *Role of van der Waals forces in the adsorption and diffusion of organic molecules on an insulating surface*, Phys. Rev. B **80**, 085401 (2009).

[162] E. Le Moal, M. Müller, O. Bauer, and M. Sokolowski, *Stable and metastable phases of PTCDA on epitaxial NaCl films on Ag(100)*, Phys. Rev. B **82**, 045301 (2010).

[163] S. W. Wu, G. V. Nazin, X. Chen, X. H. Qiu, and W. Ho, *Control of relative tunneling rates in single molecule bipolar electron transport*, Phys. Rev. Lett. **93**, 236802 (2004).

[164] T. Chassé, C.-I. Wu, I. G. Hill, and A. Kahn, *Band alignment at organic-inorganic semiconductor interfaces: α-NPD and CuPc on InP(110)*, J. Appl. Phys. **85**, 6589 (1999).

[165] I. Swart, T. Sonnleitner, and J. Repp, *Charge state control of molecules reveals modification of the tunneling barrier with intramolecular contrast*, Nano Lett. **11**, 1580 (2011).

[166] G. Kresse and D. Joubert, *From ultrasoft pseudopotentials to the projector augmented-wave method*, Phys. Rev. B **59**, 1758 (1999).

[167] G. Kresse and J. Furthmüller, *Efficient iterative schemes for ab initio total-energy calculations using a plane-wave basis set*, Phys. Rev. B **54**, 11169 (1996).

[168] J. P. Perdew, J. A. Chevary, S. H. Vosko, K. A. Jackson, M. R. Pederson, D. J. Singh, and C. Fiolhais, *Atoms, molecules, solids, and surfaces: Applications of the generalized gradient approximation for exchange and correlation*, Phys. Rev. B **46**, 6671 (1992).

[169] P. O. Gartland, S. Berge, and B. J. Slagsvold, *Photoelectric work function of a copper single crystal for the (100), (110), (111), and (112) faces*, Phys. Rev. Lett. **28**, 738 (1972).

[170] P. Gartland and B. J. Slagsvold, *Transitions conserving parallel momentum in photoemission from the (111) face of copper*, Phys. Rev. B **12**, 4047 (1975).

[171] A. Hauschild, K. Karki, B. C. C. Cowie, M. Rohlfing, F. S. Tautz, and M. Sokolowski, *Molecular distortions and chemical bonding of a large π-conjugated molecule on a metal surface*, Phys. Rev. Lett. **94**, 036106 (2005).

[172] P. Crews, J. Rodríguez, and M. Jaspars, *Organic structure analysis* (Oxford Univ. Press, 2010).

[173] J. W. Blunt, B. R. Copp, M. H. G. Munro, P. T. Northcote, and M. R. Prinsep, *Marine natural products*, Nat. Prod. Rep. **27**, 165 (2010).

[174] K. C. Nicolaou and S. A. Snyder, *Chasing molecules that were never there: Misassigned natural products and the role of chemical synthesis in modern structure elucidation*, Angew. Chem. Int. Ed. **44**, 1012 (2005).

[175] M. E. Maier, *Structural revisions of natural products by total synthesis*, Nat. Prod. Rep. **26**, 1105 (2009).

[176] W. Pathom-aree, J. E. M. Stach, A. C. Ward, K. Horikoshi, A. T. Bull, and M. Goodfellow, *Diversity of actinomycetes isolated from Challenger Deep sediment (10,898 m) from the Mariana Trench*, Extremophiles **10**, 181 (2006).

[177] P.-L. Wu, Y.-L. Hsu, and C.-W. Jao, *Indole alkaloids from cephalanceropsis gracilis*, J. Nat. Prod. **69**, 1467 (2006).

[178] J. J. Mason, J. Bergman, and T. Janosik, *Synthetic studies of cephalandole alkaloids and the revised structure of cephalandole A*, J. Nat. Prod. **71**, 1447 (2008).

[179] R. Temirov, S. Soubatch, O. Neucheva, A. C. Lassise, and F. S. Tautz, *A novel method achieving ultra-high geometrical resolution in scanning tunneling microscopy*, New J. Phys. **10**, 053012 (2008).

[180] T. König, G. H. Simon, H.-P. Rust, G. Pacchioni, M. Heyde, and H.-J. Freund, *Measuring the charge state of point defects on MgO/Ag(001)*, J. Am. Chem. Soc. **131**, 17544 (2009).

[181] T. Leoni, O. Guillermet, H. Walch, V. Langlais, A. Scheuermann, J. Bonvoisin, and S. Gauthier, *Controlling the charge state of a single redox molecular switch*, Phys. Rev. Lett. **106**, 216103 (2011).

[182] A. Masago, M. Tsukada, and M. Shimizu, *Simulation method of Kelvin probe force microscopy at nanometer range and its application*, Phys. Rev. B **82**, 195433 (2010).

[183] L. Gross, *Recent advances in submolecular resolution with scanning probe microscopy*, Nature Chem. **3**, 273 (2011).

[184] F. Jäckel, U. G. E. Perera, V. Iancu, K.-F. Braun, N. Koch, J. P. Rabe, and S.-W. Hla, *Investigating molecular charge transfer complexes with a low temperature scanning tunneling microscope*, Phys. Rev. Lett. **100**, 126102 (2008).

[185] C. Tao, J. Sun, X. Zhang, R. Yamachika, D. Wegner, Y. Bahri, G. Samsonidze, M. L. Cohen, S. G. Louie, T. D. Tilley, R. A. Segalman, and M. F. Crommie, *Spatial resolution of a type II heterojunction in a single bipolar molecule*, Nano Lett. **9**, 3963 (2009).

[186] L. Grill, M. Dyer, L. Lafferentz, M. Persson, M. V. Peters, and S. Hecht, *Nano-architectures by covalent assembly of molecular building blocks*, Nature Nanotech. **2**, 687 (2007).

[187] W. Wang, X. Shi, C. Lin, R. Q. Zhang, C. Minot, M. A. Van Hove, Y. Hong, B. Z. Tang, and N. Lin, *Manipulating localized molecular orbitals by single-atom contacts*, Phys. Rev. Lett. **105**, 126801 (2010).

[188] A. Shiotari, Y. Kitaguchi, H. Okuyama, S. Hatta, and T. Aruga, *Imaging covalent bonding between two NO molecules on Cu(111)*, Phys. Rev. Lett. **106**, 156104 (2011).

Acknowledgements

The experiments presented in this thesis were carried out in the *Physics of Nanoscale Systems* group at IBM Research – Zurich. I would especially like to thank the following people who have contributed to this thesis:

- Dr. Leo Gross and Dr. Gerhard Meyer for offering me the chance of working on this thesis project together with them. Thank you for being such supportive, relaxed, inspiring and motivating colleagues.
- Dr. Rolf Allenspach for giving me the opportunity to work in his group. Thank you for your great managerial and personal support.
- Prof. Dr. Jascha Repp for supervising and guiding this thesis and Prof. Dr. Christian Back for his willingness to co-referee this thesis.
- Dr. Nikolaj Moll, who carried out the DFT calculations presented in Chapter 5 and 7.
- Prof. Dr. Franz Giessibl for providing the qPlus tuning forks and helpful support with their setup.
- Prof. Dr. Mats Persson and Dr. Matthew Dyer, who carried out the DFT calculations of the Au-PTCDA complex presented in Chapter 6.
- Prof. Dr. Marcel Jaspars, Dr. Rainer Ebel, and Dr. Wael Abdel-Mageed, who provided the metabolite investigated in Chapter 7 and performed the initial structure analysis with mass spectrometry and NMR.
- Bruno Schuler, who performed the measurement shown in Fig. 5.2c.

- Dr. Andreas Heinrich and Dr. Dan Rugar for offering me the possibility of spending some very interesting weeks at IBM Research – Almaden.
- The European Union for financial support within the Marie Curie initial training network Herodot.